Single- and Multicomponent Hydrate Phase Transitions and $CO_2 - CH_4$ Exchange in a Synthetic Porous Media

Master Thesis in Reservoir Physics

By

Ørjan Strand

Department of Physics and Technology

University of Bergen

June 2020

Abstract

Natural gas hydrates exist in vast amounts in subsurface permafrost and oceanic sediments. The growing demand for energy combined with the need for reduced CO_2 emissions makes natural gas hydrates a potential target for CCUS (Carbon Capture Utilization and Storage). Injecting CO_2 into methane hydrate reservoirs is a win-win process where methane gas is produced and CO_2 is sequestrated. Pore-scale observations can provide insights into multicomponent behaviour of hydrate phase transitions. Previous experimental pore-scale studies done by the Reservoir Physics group at the University of Bergen was based on hydrates formed by a single component, either pure carbon dioxide (CO_2) or pure methane (CH_4). In this work, hydrates were formed from mixtures of CO_2 and CH_4 in micromodels replicating a real sandstone. The main objective of this thesis was to investigate the pore scale physics of mixed hydrates and processes of CH_4 - CO_2 exchange.

A total of twenty experiments were conducted in this work. Twelve multicomponent systems were characterised before and after hydrate formation. In addition, eight experiments where CO_2 was injected into a pore network saturated with methane hydrate were analysed. The formation experiments were carried out with pressure ranging from 48 to 70 bar and temperature from 1 to 5 ^{o}C. CO_2 was injected at pressures close to the hydration pressure of methane hydrate.

Hydrate formation was dependent on the concentration and distribution of components and initiated at the water-CO_2 or water-CH_4 interface. The amount of dissolved CO_2 in water controlled the hydrate growth in water. Hydrate growth resulted in two different configurations: 1) crystalline hydrate with total consumption of gas components, and 2) hydrate films enclosing gas components.

There were performed eight liquid CO_2 injections into pore space with methane hydrate. To get physical observation of liquid CO_2 in the system, liquid CO_2 had to displace a water bank. Methane was enclosed by hydrate film that allowed water to displace in situ methane gas and reduced hydrate saturation. The supply of water and liquid CO_2 promoted crystalline growth of hydrate film enclosing methane.

Nineteen hydrate dissociation experiment was conducted by stepwise pressure reduction. The hydrate dissociation was studied with respect to dissociation pressure points. The dissociation of a mixed hydrate released gas in portions/bubbles at given pressure steps. Dissociation points were plotted against theoretical gas composition values calculated by CSMGem. A system with high amounts of CO_2 before formation was observed to dissociate at pressure closer to pure CO_2 hydrate equilibrium. Furthermore, a system with high amounts of CH_4 gas before formation was observed to dissociate at pressures closer to pure CH_4 hydrate equilibrium.

Acknowledgements

Many persons have directly and indirectly contributed to this work. I would like to express my gratitude to the following persons:

To my supervisor, Associate Professor Geir Ersland, for introducing me to the world of gas hydrates and for providing me with an exciting topic as gas hydrates. His positive spirits made the threshold very low to get in contact for scientific discussion, and his valuable inputs saved me many hours of frustration.

To Dr Stian Almenningen, for his guidance in the laboratory and for patiently answering all my “silly questions”. Your knowledge about micromodel work and guidance has been invaluable and enlightening.

To my lab partner and PhD candidate, Jyoti Shanker Pandey, for teaching me important theory and your dedication in the laboratory has been invaluable.

To the rest of the staff in Reservoir Physics group, for creating a friendly environment and professional scientific group.

To my fellow students and friends, for making a social and productive environment. I will always be proud of my time as a student and as a part of PTEK, thank you.

To my parents Rolf and Reidun, and my brother Lars-Petter for their support and motivations during my time at the University of Bergen.

Bergen, June 2020

Table of contents

Introduction

The renewable energy wave is sweeping across the globe, and the world is facing the energy transition into the new "renewable world". Electricity use grows at more than double the pace of overall energy demand (International Energy Agency, 2019). As global consumption is expected to increase towards 2050, shows that the world needs a supply of more energy. Natural gas is the fastest-growing fossil fuel and is preferred over other fossil fuels due to its lower emission of greenhouse gases upon combustion. Natural gas hydrates are an unconventional resource with vast global estimates in the order of twice of the global coal, oil and gas reserves (Kvenvolden, 1988). The exploitation of gas hydrates can lead to reduced CO_2 emission by eliminating coal in the energy mix and sustain the demand for energy. As a potential new energy resource, natural gas hydrates have gained interest worldwide. Many countries, e.g. China, India, Japan, USA and Canada, seek to be self-sustained with energy partly by recovering natural gas from hydrates in sediments offshore and beneath the permafrost.

Gas hydrates form a cage-like framework interconnected by hydrogen-bonded water molecules. The crystalline framework is stabilized by non-polar guest molecules referred to as hydrate formers. The guest molecules are typically methane, ethane and carbon dioxide, where methane is the most abundant hydrate former in nature. Pressure and temperature conditions are essential to the formation of hydrate together with water availability, and the thermodynamical parameters heat and mass transport.

Producing natural gas from hydrates usually involves depressurization, thermal stimulation or inhibitor injection. Depressurization is considered as the most promising technique, and together with thermal stimulation, hydrates are destabilized by pressure reduction and temperature increase. Injection of chemical inhibitors such as salts or alcohol destabilizes hydrates by creating a shift in the equilibrium curve to higher pressure and lower temperatures. Injection of inhibitors is also utilized to prevent hydrate formation in up-, mid- and downstream industry.

CO_2 injection into a methane hydrate reservoir is a more recent production scheme coupled to CCUS (Carbon Capture Utilization and Storage). The technique is based on the spontaneous conversion from methane hydrate to CO_2 hydrate when pre-existing methane hydrate is exposed to gaseous/liquid CO_2. It has been extensively studied in the last decade and poses a viable "win-win" process where methane gas is produced and CO_2 is sequestered. A successful field pilot on the North Slope of Alaska demonstrated the viability of CO_2 - CH_4 exchange in 2012 (Schoderbek *et al.*, 2013). Potential limitations include formation of pure CO_2 hydrates with excess water. Hydrate reformation leads to a reduction in permeability and can potentially clog the injection well.

1 - Theoretical part

1.1 Fundamentals

Gas hydrates are crystalline structures built by water molecules that interconnect through hydrogen-bonding. The crystalline hydrate structure is a crystalline lattice with cavities/cages giving them the ability to encapsulate a guest molecule. Hydrates are unable to form without the presence of guest molecules. The cavities can inhabit different non-polar or slightly polar guest molecules, such as hydrocarbons. The cavities are stabilized by the guest molecules size and shape, together with Van der Waals forces at the water-guest interface which prevents the cavity from collapsing.

Molecular building blocks

A hydrate structure is built by different unit cells such as the pentagonal dodecahedron, tetradecanhedra and hexakaidecahedra. The pentagonal dodecahedron is composed of 12 pentagonal faces, denoted 5^{12}. It represents a small cavity and is a building block in the three most common hydrate structures. The average radius of a small cavity is 3.95 Å which is suitable for a small guest molecule like methane. Tetrakaidekahedron is composed of twelve pentagonal and two hexagonal faces and is denoted $5^{12}6^2$ and represents a large cavity. The average radius of a large cavity is 4.33 Å which is suitable for larger molecules such as carbon dioxide (CO_2) and ethane. Joining two small cavities together will form a hexakaidecahedra with twelve pentagonal- and four hexagonal faces denoted $5^{12}6^4$.

Hydrate structures

Hydrates can form different structures, with both small and large cavities depending on the arrangement of water molecules in the lattice. Figure 1-1 describes the three different hydrate structures, structure I (sI), structure II (sII) and structure H (sH). These three are the most common hydrate structures in nature even though different structures have been formed experimentally with other guest molecules and not hydrocarbons.

Structure I (sI) hydrate is formed of two small cavities (5^{12}) and six large cavities ($5^{12}6^2$). Structure I is the most common in nature and has 46 water molecules per unit cell. Both cavities can occupy a small guest molecule such as methane, but the large cavity can fit larger molecules such as CO_2. Two components, such as CO_2 and CH_4, or a mixed composition in the cavities will form a mixed hydrate.

Structure II (sII) hydrate is formed of 16 small cavities (5^{12}) and eight large cavities ($5^{12}6^4$). Structure II often materialize experimentally and consists of 136 water molecules per unit cell. Small

molecules like methane can occupy the small cavities, and large cavities can occupy larger molecules such as propane (C_3H_8) and isobutane (C_4H_{10}).

Structure H (sH) has a complex constructed hydrate structure. It is made up of three small (5^{12}), two medium $(4^3 5^6 6^3)$ and one large cavity $(5^{12}6^8)$ and has 34 water molecules per unit cell. sH stabilizes when molecules of different sizes occupy small/medium and large cavities. Accordingly, a mix of methane and neohexane will occupy small and large cavities respectively and stabilize the hydrate structure.

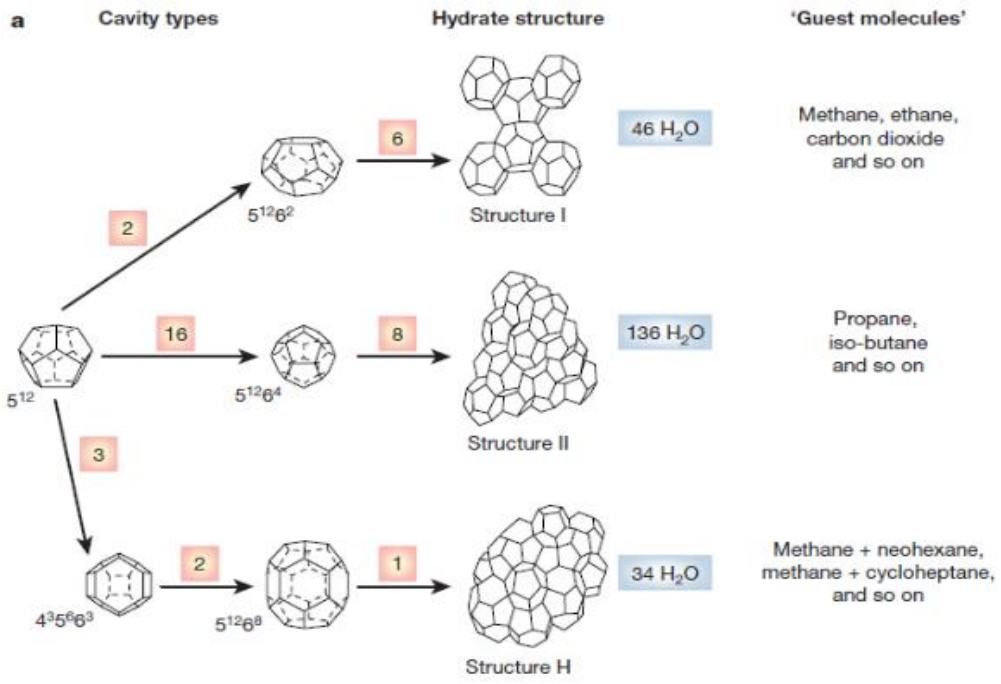

Figure 1-1 - Illustration of the different hydrate structures (Sloan, 2003)

The hydrate structure is dependent on the size of the guest molecules diameter with the unit Ångstrøm, which is $0{,}1\ nm - 10^{-10}m$. The hydrate lattice becomes stable when the guest molecules occupy the minimum number of cavities, thereby preventing the breakage and strain of the hydrogen bonds (Sloan, 2003).

Table 1-1 – Specifications of hydrate structures. Modified from Sloan (Sloan, 2003).

Hydrate crystal structure	**I**		**II**		**H**		
Cavity	Small	Large	Small	Large	Small	Medium	Large
Description	5^{12}	$5^{12}6^2$	5^{12}	$5^{12}6^4$	5^{12}	$4^35^66^3$	$5^{12}6^8$
Cavities per unit cell	2	6	16	8	3	2	1
Avg cavity radius (Å)	3.95	4.33	3.91	4.73	3.91	4.06	5.71
Coordination number	20	24	20	28	20	20	36
Waters per unit cell	46		136		34		

Hydrate guest molecules

A multicomponent system of CO_2 and CH_4 can create different mixtures dependent on the amount of each component in the system. CO_2 can exist in both liquid and gaseous state, whereas CH_4 exist predominantly in the gaseous state and will condense to a liquid state at 112 K. If both components exist in a gaseous state, they will mix into one gas phase. When gaseous CO_2 condense to a liquid phase, CH_4 can dissolve into the liquid phase and create a mixed liquid composition. The two components will form a binary composition, and the highest amount of dissolved gas in the liquid mix is determined by the vapor-liquid equilibrium (VLE).

Binary mixture

Nasir (Nasir *et al.,* 2015) calculated the vapor-liquid equilibrium for a binary mixture of CH_4 and liquid CO_2 at isothermal condition. They calculated vapor-liquid equilibrium at a range of temperatures, but the most relevant temperatures for this thesis are 274.15, 275.95 and 278.05 K. Figure 1-2 illustrates a phase envelope based on the results obtained by Nasir. The figure shows 3 bubblepoint lines and 3 dewpoint lines. Above the bubblepoint equilibrium, the system will consist of a liquid phase where the CH_4 gas has dissolved into the liquid CO_2 phase. Between the bubblepoint and dewpoint equilibrium lines, the amount of CH_4 exceeds the solubility limit in liquid CO_2. At this point, CH_4 and a liquid mix (CO_2 and CH_4) will coexist and form a two-phase system. Depending on the pressure and temperature, Figure 1-2, shows the liquid phase at 70 bar and 278.05 K can contain a CH_4 mole fraction of 0.1292.

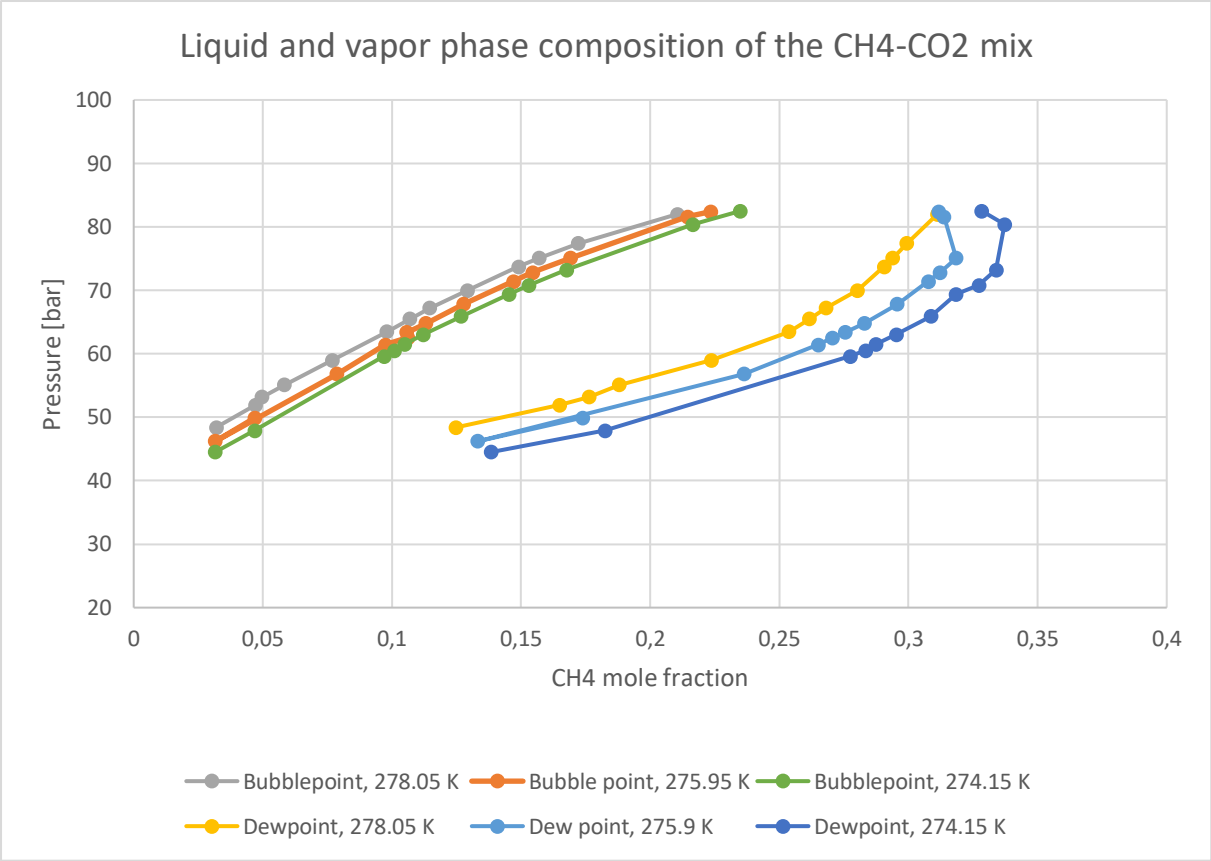

Figure 1-2 – Phase envelopes for a binary mixture of CH_4 and liquid CO_2.

Hydrate stability conditions

Gas hydrates will form when water and guest molecules are exposed to thermodynamic driving forces. Thermodynamic driving forces means high pressures (> 20 bar) and low temperatures (<10 ^{o}C). The stability region for a hydrate is given by the guest molecule or the composition of the guest molecules. Figure 1-3 illustrates four different hydrate stability regions as a function of pressure and temperature of the two components used in this thesis. Zone II shows CO_2 is a stable hydrate former in the gaseous state below 10 ^{o}C and liquid state in temperature regime ranging from 5 ^{o}C – 10 ^{o}C. Zone III illustrates the stability region for pure methane hydrate. Zone IV represents pressure and temperature regime where pure CH_4- and CO_2 hydrates can form. The presence of both components will generate a multicomponent system and mixed hydrates will form. All zones represent the Gas Hydrate Stability Zone (GHSZ). Methane hydrate exposed to CO_2 will initiate a spontaneous exchange between where CO_2 will replace methane molecules and form a mixed hydrate (Graue *et al.*, 2006; Kvamme *et al.*, 2007).

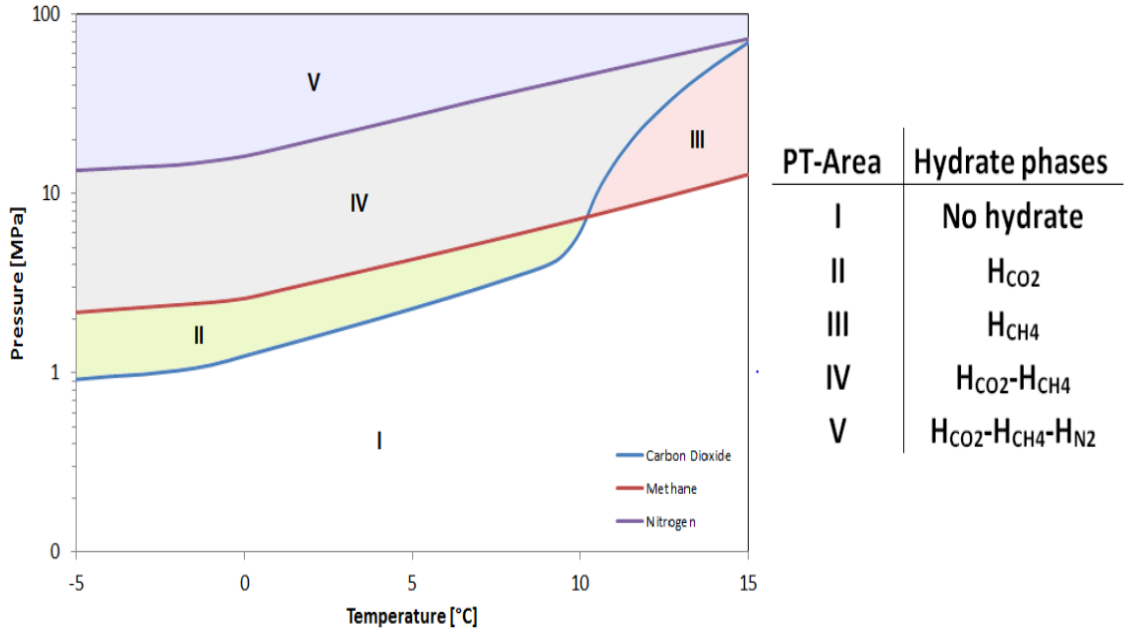

Figure 1-3 – Hydrate stability regions for pure hydrates and multicomponent hydrates containing CH_4, CO_2 and N_2. Modified from Husebø (Husebø, 2008)

1.2 Hydrate formation

Hydrates form when pressure and temperature is within the GHSZ combined with availability of hydrate-formers and water molecules. Formation of hydrate can be separated into nucleation and growth.

Hydrate nucleation

Hydrate nucleation is an unstable process where water and hydrate formers grow and disseminate seeking to reach a critical size, empowering them to further growth (Sloan & Koh, 2008). This happens on a microscale and cannot be detected macroscopically. To overcome the critical cluster size, Gibbs free energy must be minimized. This is a competition between surface excess free energy and volume excess free energy (Sloan, 1998). When the free energy overcomes the surface energy of the new interface, further growth can occur. Minimization of free energy can be expressed as (Kvamme, 2016):

$$\Delta G = \Delta G^{surface} + \Delta G^{phase\ transition} = 4\pi r^2\gamma + \frac{4}{3}\pi r^3 \rho_N^H \Delta g^{phase\ transition} \leq 0 \qquad 1$$

where ΔG is the total excess free energy, $\Delta g^{phase\ transition}$ is the intensive change in Gibbs free energy related to the phase transition $[\frac{J}{mole}]$, r is the crystal radius [m], γ is the interfacial tension $[\frac{J}{m^2}]$ and ρ_N^H is the molecular density $[\frac{mole}{m^3}]$.

The surface excess free energy and free energy from phase transitions (volume excess free energy) have opposite signs. Where surface excess free energy is a positive quantity, while volume excess free energy is a negative quantity. If the volume excess free energy overcomes the penalty from the creation of new surface area, critical size may be attained, and massive growth can proceed. Being a microscopic phenomenon with tens to thousands of molecules makes the nucleation stage hard to observe experimentally. Molecular simulation studies show that critical size is in the order of nanometers and can be reached within microseconds (Walsh, 2011).

Nucleation can be divided into homogenous and heterogeneous nucleation. Homogeneous nucleation is rapid hydrate crystallization in a system without any impurities. Homogeneous nucleation is very rare and nearly impossible to achieve experimentally. Heterogeneous nucleation considers impurities and occurs in the presence of foreign particles or surfaces which reduces the critical size for a nuclei (Sloan, 1998). Aqueous solutions and gas prepared for lab experiments usually have more than 99 % purity, 1 % fluid impurity will contribute to heterogeneous nucleation. In nature, reservoirs have many heterogeneities and a synthetic porous media used in this thesis is indeed heterogeneous.

Induction time

Induction time is often used in the same context as nucleation, but these mechanisms take place on different scales. Nucleation is a microscale process not visual to the eye and is a part of the total induction time. Induction time is a macroscopic event and can be defined as the time needed to reach visible hydrate. Hydrates will not automatically form when entering the hydrate stability zone because of metastability. This causes massive growth to vary from minutes to hours and even days. This makes induction time in experiments dependent on human visual inspection. Englesoz (Englezos *et al.*, 1987) and Sloan (Sloan, 2008) reports that induction time reduces, and the system becomes more predictable at higher driving forces respectively. Induction time is the period from hydrate stable conditions are reached until hydrate has reached a critical size and massive visual growth can commence.

Growth

At the end of nucleation and induction time, crystals/nuclei have reached a critical size and hydrates will start to grow. The growth rate is dependent on the available water and guest molecule coupled with mass transport and heat transfer. Hydrate growth on a molecular level is influenced by three parameters (Sloan, 2008);

- Kinetics of crystal growth at the hydrate forming area
- Mass transfer of molecules to the hydrate forming area
- Heat transfer of the exothermic heat released during hydrate formation away from the hydrate forming area.

Hydrate formation has an exothermic nature and released heat can give increased local temperature and counteract formation. During growth, gas is volumetrically compacted by a factor of 164 and the growth period is identified by a sudden pressure drop (Moridis *et al.*, 2009). Initial growth is fast, but the growth rate will decline when the amount of water and hydrate components is minimized and eventually terminate.

Agitation

Driving forces induce hydrate formation mechanisms, but high driving forces do not always promote nucleation and massive hydrate growth. Agitation is a pressure pulse induced to accelerate nucleation and reduce induction time in experiments conducted in a synthetic porous media and bulk systems. In micro models, the pressure pulse induces a flow through the pores whereas in bulk systems a magnetic stirrer induces fluid flow to provoke hydrate formation.

Due to difficulties of hydrate formation under static conditions on the pore scale at the Reservoir Physics group, earlier students have used the agitation technique. Lysyy, Iden and Flatlandsmo (Flatlandsmo, 2015; Iden, 2017; Lysyy, 2018) have all reported the importance of agitation.

1.3 Natural gas hydrates in nature

Gas hydrates are found beneath permafrost or in marine continental margin sediments worldwide. The gas in gas hydrates originates deep inside earth sediments outside GSHZ from biogenic or thermogenic sources. Biogenic hydrate forms from anaerobic bacterial decomposition of organic matter at low temperatures. While thermogenic hydrate form by high temperature catagenesis above 100 ^{o}C. Once the gas is released from the source rock, density difference and buoyancy effect cause it to migrate upwards as free gas or dissolved in water. This gives the gas by a biogenic source a shorter migration pathway to enter the GHSZ, making it the most abundant source for hydrate formation.

Hydrate reservoirs

Once the gas has accumulated in the GHSZ, a hydrate reservoir will form. Hester and Brewer (Hester and Brewer, 2009) report that more than 90 sites have been directly or indirectly identified to contain gas hydrates. To date, this number is probably significantly higher due to seismic technology development. It is estimated that 97 % of hydrate deposits are found in oceanic sediments where pressure and temperature conditions are within the GSHZ. This is illustrated in Figure 1-4.

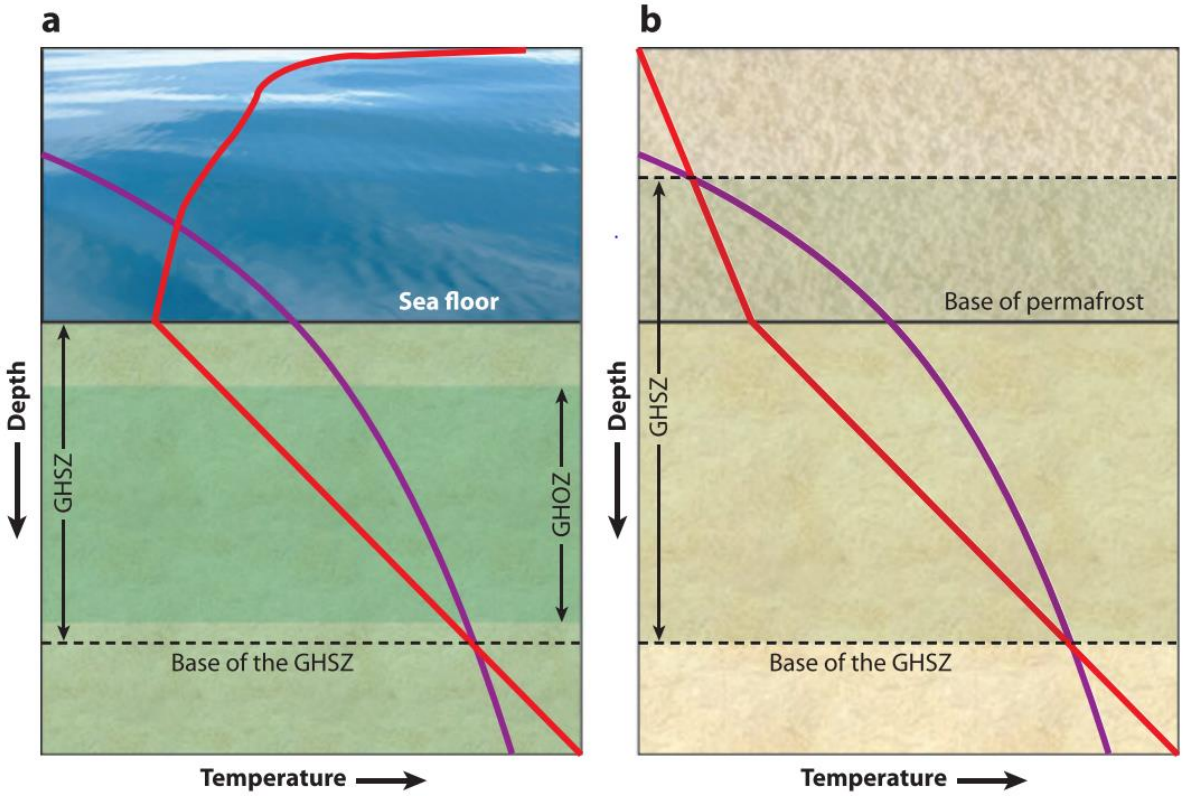

Figure 1-4 – Gas hydrate stability zone for (a) marine sediments found at continental margins and (b) permafrost. Purple- and red line illustrates the hydrate stability curve and ambient temperature profile respectively. The GHSZ is defined by the area between the upper- and lower intersection point (Hester and Brewer, 2009)

For oceanic sediments, the location of the GHSZ is beneath seafloor/seabed given a 300-600 m overlying hydrostatic column with a temperature regime from 2 to 20 ^{o}C. Below seafloor, hydrate formation is limited to gas hydrate occurrence zone (GHOZ), because a marine environment reduces methane availability due to sulphate reduction and anaerobic oxidation. In permafrost regions, the location of the GHSZ is located at 200-600 m depths and extends hundreds of meters dependent on the base of permafrost and the geothermal gradient. The temperature regime ranges from -10 to 20 ^{o}C in the permafrost regions. This temperature regime can create a two-phase gas + ice system until

high enough pressures provoke hydrate formation. The GHSZ exceeds below the base of permafrost until temperature conditions are outside the GHSZ, causing a gas + liquid two-phase region.

Hydrate reservoir classification

Depending on the geologic and reservoir conditions, the natural gas deposits are divided into three main classes (Moridis *et al.*, 2003).

Class 1 reservoirs are composed of two zones: the hydrate interval and a two-phase fluid zone with free water and gas.

Class 2 reservoirs are composed of a hydrate interval on top free water.

Class 3 is characterized by a single hydrate layer interval in the absence of underlying fluids.

The reservoir classes are illustrated in the next figure

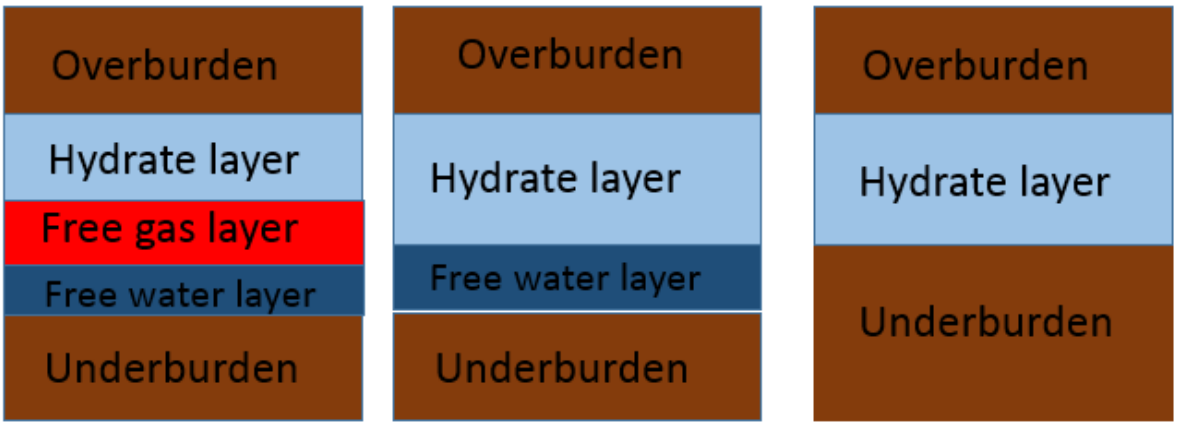

Figure 1-5 – Description of hydrate reservoir classes from class 1 to 3 respectively. Class 1 is defined as excess gas and class 2 is defined as excess water. Based on concepts from (Moridis et al., 2003)

Class 1 reservoir is the most desirable system production wise due to the required amount of energy to produce it.

Accessibility of these resources depends on the geological setting they were formed and hydrate saturation. The global price for natural gas forces reservoirs to be in proximity to existing infrastructure to make it commercially viable. The geological environment and vicinity of existing infrastructure make the Gulf of Mexico a favourable region to extract gas hydrates. The potential energy stored in gas hydrates globally is estimated to be twice of recovered and undiscovered coal, oil and gas reserves worldwide (Kvenvolden, 1988).

1.3.1 Challenges related to gas extraction from gas hydrates

Challenges related to gas hydrates range from exploration, production, reservoir management geologic, and it promotes a risk towards global warming. Makogon (Makogon, 2010) states that more than 230 gas hydrate deposits exist globally. The 90 direct discoveries reported by Hester and Brewer illustrates the challenges related to exploration and seismic data interpretation.

Environmental aspect

Gas hydrates in permafrost regions pose a risk to global warming and a potential accelerated greenhouse effect. The greenhouse effect of methane is estimated to be 20 times bigger, although its time in the atmosphere is shorter compared to CO_2. The increase in global temperature causes the permafrost to melt and bring hydrate layers outside the GHSZ and creates a potential seep of methane gas to the atmosphere. It will be more beneficial to produce methane from hydrate sediments than let it dissociate and rise into the atmosphere. The most abundant greenhouse gas is CO_2 and there is a global consensus on the need to reduce CO_2 emissions. Methane is regarded as the cleanest fossil fuel due to its low CO_2 emission upon combustion. Methane hydrate can be a potential source of energy until renewable energy can sustain the increased global demand for energy. CO_2 injection into methane hydrate offers a win-win strategy by methane production and sequestration of CO_2.

Production

One cubic metre of gas hydrate contains 164 cubic metres of gas. Drilling or producing a hydrate reservoir reduces the volume of the solid hydrate phase and converts it into a mixed fluid phase that is several times larger in volume (Waite et al., 2009). The immense volume expansion will cause pressure increase that can cause borehole to collapse or in the worst-case scenario a severe blowout. Gas hydrate wells are operated at low pressure and temperature, and the risk of hydrate reformation is evident through the whole production line. Maintaining gas flow at high water production rates will require some form of artificial lift together with powerful processing modules to cope with the high water cut (Moridis et al., 2011).

Geomechanical stability

Hydrate sediments suitable for extraction are often poorly consolidated due to limited shear strength. Production of gas from hydrates changes the bulk volume, which in turn reduces the pore pressure and poses a risk to geomechanical stability. Changes in sediment properties such as borehole integrity loss can lead to possible slope collapse with the following marine geohazard such as tsunamis. The Ormen Lange gas field is located on the northwest coast in the Norwegian Sea and is the second-biggest gas field in Norway. The development started as late as in 2004 and the major

challenge was to establish pipelines across the Storegga ridge. The Storegga ridge was the initiation point of the Storegga Slide which is one of the most massive submarine slides and tsunami ever discovered. The geomechanical stability in the Storegga area was affected by several geological factors. Local destabilization caused by gas hydrates could be one of them (Bryn et al., 2005). CO_2 sequestration in hydrate-bearing sediments is proposed as a viable option to exploit hydrate reservoirs safely to avoid loss of pore pressure and to keep the integrity of the geomechanical stability.

1.4 Hydrate dissociation

The encapsulated gas in hydrates is produced by bringing the pressure and temperature conditions outside the GSHZ. At a given temperature, the pressure inside a hydrate cavity is called the equilibrium pressure. Pressure reduction below the equilibrium pressure will cause the hydrate to melt/dissociate. The released gas will cause a volume expansion and increased pore pressure. Mixed hydrates can have a range of equilibrium pressures dependent on the cavity filling.

1.4.1 Production techniques

Gas hydrates can potentially be an energy resource supplying the global demand for energy for the next hundred years. Gas hydrates are produced by hydrate dissociation by depressurization, thermal stimulation or inhibitor injection. These are the most viable methods although more unconventional methods are proposed but generally not accepted. A more recent production scheme is based on exposing hydrates to another hydrate former (e.g. CO_2), this results in a thermodynamical reaction and will be discussed in section 1.5. Long- term production strategies often utilize a combined effect of two or more methods.

Depressurization

Pressure reduction below the equilibrium value at a given temperature will cause hydrates to dissociate. The pressure drop will propagate through the reservoir and cause hydrate to become unstable and start to melt/dissociate. The rapid expansion of gas and endothermic nature of hydrate dissociation can cause a temperature drop and terminate further dissociation, and thermal stimulation or inhibitor injection is needed. Depressurization is considered as the most promising production technique as it is the cheapest and most energy-efficient production method (Sloan & Koh, 2008). In this thesis, hydrates are dissociated by stepwise pressure reduction.

Thermal Stimulation

The thermal stimulation technique is based on increasing the temperature above the equilibrium value at a given pressure. Hot water/steam injection or direct heating of the formation is the most common technique. In industry the best way to avoid hydrate plugs in flowlines is to keep the

temperature high enough, so the hydrate conditions are outside the GHSZ. Thermal stimulation is slow, and it demands high amounts of energy. It is often used to avoid drawbacks in combination with depressurization. Thermal stimulation was applied in the Mallik field pilot in 2002. Gas was produced from the hydrate reservoir when the bottom hole temperature was increased to greater than 50 ^{o}C while maintaining constant pressure (Hancock *et al.*, 2005).

Hydrate inhibition

Injection of chemicals promotes a fast dissociation. Thermodynamic inhibitors such as methanol, glycol and salts will make a shift in the hydrate equilibrium curve to higher pressures and lower temperature causing hydrate to dissociate. The production technique is highly dependent on diffusion and effective permeability in the reservoir. It is not considered as the primary technique for long-term production schemes due to high expenses and the necessity for separation of the produced gas. Shifting the equilibrium line to higher pressures and lower temperatures is also a measure to prevent hydrate formation. Hydrate plugs can damage gas transport system equipment and hydrate inhibition is mostly used in the industry to prevent hydrate formation. The petroleum industry spends about one billion US dollars a year to prevent hydrate formation in wells, equipment and flowlines (Makogon, 2010).

Memory effect

Hydrates release high amounts of water during melting, and it is suggested that the free water keep a memory of the hydrate structure. The memory effect will cause hydrate to nucleate faster in a dissociated system compared to a system with replenished water with no previous hydrate history. Enough heating will dismantle the memory effect from the free water. Sloan (Sloan, 2008) proposed two hypotheses to explain the memory effect:

1. Hydrate structure remains in a system as a residual structure of partial hydrate cages or persistent hydrate crystallites in the solution.
2. Dissolved gas remains in the solution after hydrate dissociation.

It is believed the memory effect participates in the reformation of mixed hydrate during dissociation and exchange processes between methane hydrate and CO_2.
In order to avoid the memory effect during hydrate formation, it is crucial to flush the system between each experiment.

Self-preservation of gas hydrates

Self-preservation occurs when P-T conditions are outside the GHSZ and temperature is sub-zero. This phenomenon shows that hydrates remain stable for extended periods outside the hydrate stable region. The cause of anomalous self-preservation is not fully understood, but the most accepted

theories are that high amounts of water are released during dissociation. The released water will freeze at T < 0 and cover the hydrate with ice forming an extra solid water layer around the hydrate. Natural gas hydrate ability to delay dissociation above T > 0 ^{o}C have been reported by (Makogon and Ghassemi, 2010). Sub-zero temperature conditions and the formation of ice applies forces and can cause the micromodel to break and is not to recommend. On the other hand, in the coming years, the main field of interest might include the study of self-preservation due to its effect on the long-term storage of CO_2.

1.5 Exchange

Carbon capture and storage is essential to achieve net-zero emission by 2050. U.S has injected CO_2 for EOR (enhanced oil recovery) since the '70s. In the North Sea, the produced gas from the Sleipner field in Norway contains a too high concentration of CO2. To meet the required export specifications, the CO_2 gas has been separated and injected into the formation since 1996 (Hermanrud *et al.*, 2009). Exposing methane hydrate to CO_2 is thermodynamically viable and offers safe storage of CO_2 and in situ release of methane gas (Kvamme *et al.*, 2007).

The mechanisms that work on field scale are different from a micromodel. In a micromodel, the effect of gravity is neglected. It is harder to predict the flow of CO_2 on the core and field scale due to the gravity effect. The force of gravity causes viscous fingering and will reduce the sweep efficiency through the pore network. This thesis emphasizes multicomponent hydrate formation and dissociation on pore-level, this section provides a detailed description of microscopic events of mixed gas hydrates.

1.5.1 Exchange mechanisms

The exchange process on the molecular scale is quite complicated and includes several mechanisms related to adsorption and diffusion. The replacement scheme is based on the thermodynamics of the equilibrium to CH_4- and CO_2 hydrate (Aresta *et al.*, 2015). Even though the conversion is thermodynamically favourable in terms of free energy difference, hydrate phase transitions are coupled to processes of mass- and heat transport (Graue *et al.*, 2006). This is a win-win process; where methane gas is produced, and CO_2 is safely sequestered with the released water in the hydrate reservoir.

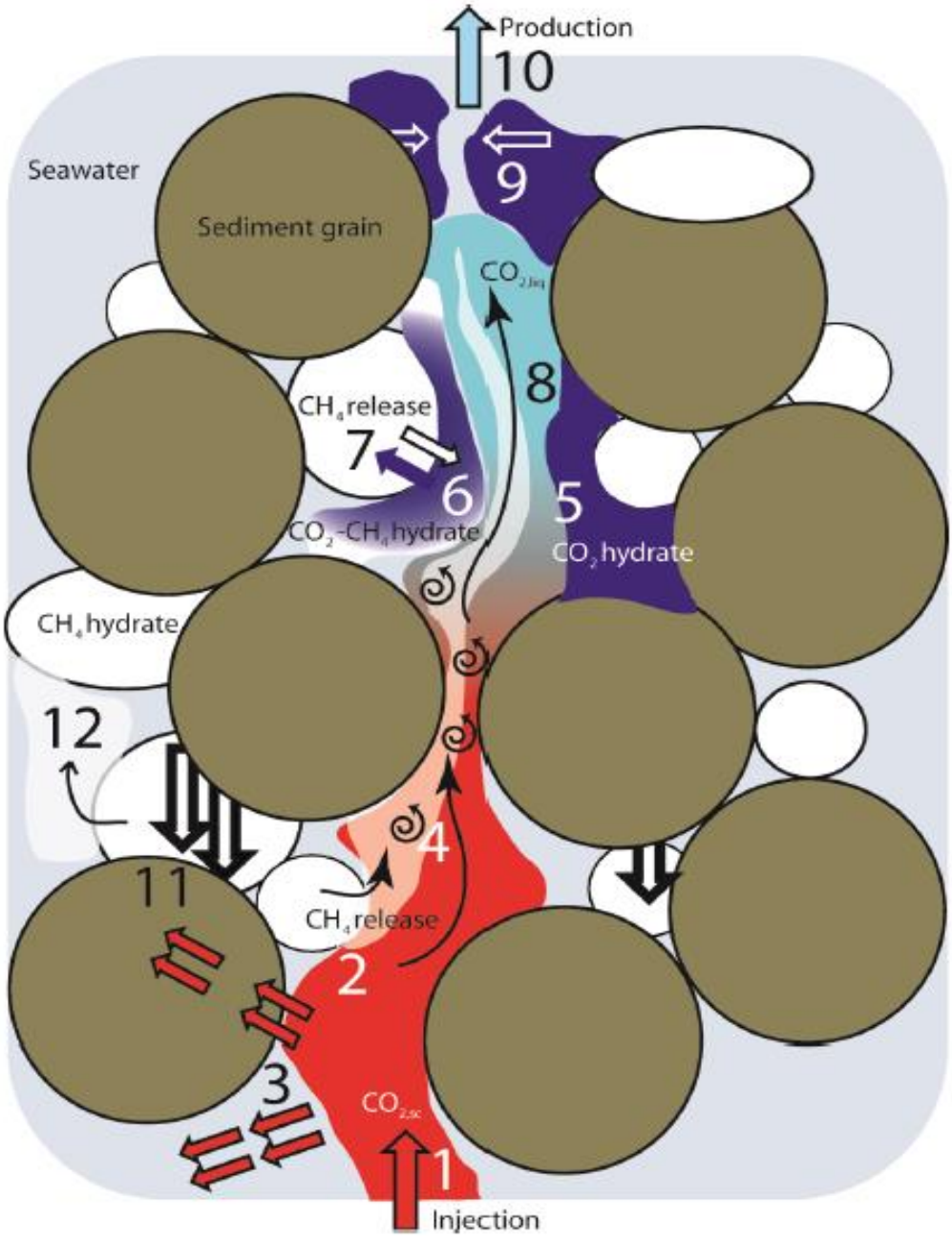

Figure 1-6 – Illustration of exchange mechanisms during an injection of supercritical CO_2 into a methane hydrate reservoir (Deusner et al., 2012). Supercritical CO_2 holds a temperature above 30 °C. 1) Injection of hot, mobile CO_2. 2) Fast dissociation of methane hydrate due to thermal stimulation from hot CO_2. 3) Conductive heat transport via sediment particles or capillary bound pore water followed thermal stimulation and dissociation of distant methane hydrate particles. 4) CO_2 and CH_4 mixes and creates a gas flow. 5) Pure CO_2 hydrate formation with pore water. 6) Formation of mixed $CO_2 - CH_4$ hydrates from $CO_2 - CH_4$ gas mixtures. 7) $CO_2 - CH_4$ exchange limited by diffusive transport of CH_4 and CO_2. 8) Supercritical CO_2 cools and transforms to a liquid phase due to the surrounding conditions. The mix of CO_2 and CH_4 is now a two-phase flow. 9) CO_2 hydrate formation with excess pore water can lead to pore space clogging leading to a reduction in permeability. 10) Production of fluid containing water, CO_2 and CH_4 in different states. 11) Dissociation of load-bearing hydrate can reduce sediment integrity and geomechanical stability. 12) CH_4 might diffuse into isolated pores as non-producible gas.

Solid-state diffusion exchange

Exposing methane hydrate to pure liquid or gaseous CO_2 will lead to an exchange where CO_2 replaces methane in the hydrate lattice. CO_2 has a high chemical potential in gas phase and zero in gas hydrate, while methane has the direct opposite. The difference in chemical potential indicates that replacement is thermodynamically favourable and the high gradient creates a driving force that induces a spontaneous conversion (Seo and Lee, 2001). This will engage the hydrate phase to replace the CH_4 molecule with a more thermodynamic stable CO_2 molecule. The phase transition is rather slow as it is based on diffusion where mass transport is the limiting factor (Graue *et al.*, 2006), and the diffusion coefficient is constrained to $D \sim 10^{-16} m^2/s$ (Liang *et al.*, 2016). A high concentration of CO_2 will enhance the diffusion process. However, the mechanism is dependent on getting in contact with the surface area of methane hydrate either by pure CO_2 in contact with hydrate, or CO_2 dissolved in water.

Liquid state conversion

The second mechanism implies that injected CO_2 can form a new hydrate together with the free water. Anderson (Anderson, 2003) reports that CO_2 hydrate has a dissociation enthalpy in the range of $[57.6, 63.6] \frac{kJ}{mol}$ at $[271.8, 283.1]\ K$, while CH_4 hydrate has a dissociation enthalpy in the range of $[52.5, 55.5] \frac{kJ}{mol}$ at $[274 - 318]K$. The formation of CO_2 hydrate is an exothermic reaction, which means heat is liberated during hydrate formation. CO_2 hydrate may form with excess-, capillary bound-, or water at the hydrate surface. The liberated heat from CO2 hydrate formation is higher than the energy required to dissociate the CH_4 hydrate structure and will assist in the dissociation of CH4 hydrate. However, Raman analysis shows the CH_4 hydrate structure does not entirely dissociate but experiences replacement in the large cavities. This suggests that large cavities dissociate, and small cavities remain stable. Cavity stability is dependent on the interactive Van der Waals force between the molecule and lattice. The interactive force between a CH_4 molecule and cavity is greatest in a small cavity. This shows that thermodynamic forces in the exchange might not overcome the stability forces inside the small cavities. Another explanation could be the reformation of the small cages after CH_4 molecules are released because CO_2 molecules are unlikely to be able to occupy the small cages. It is expected that the conversion rate increases with higher amounts of the surrounding water. It will generate a larger contact area and is mostly limited by mass transport to the surface area. Heat transport through liquid water and hydrate is 2-3 orders of magnitude faster than solid-state diffusion. CO_2 hydrate formation facilitates heat transfer from its region towards in situ methane hydrate and will be the dominant factor during CO_2 - CH_4 exchange.

Two-step exchange

Zhao (Zhao *et al.*, 2015) and Falenty (Falenty *et al.*, 2016) describes the exchange procedure as a combination of solid-state and liquid-state exchange. The first stage is a short surface-replacement where CO_2 hydrate forms at the CH_4 hydrate interface. Heat release partially dissociates the CH_4 hydrate, allowing the release of CH_4 molecules and encapsulation of CO_2 molecules to form a mixed hydrate. The highest ratio of released methane and formed CO_2 occurs during this stage. The second step describes an inner-layer exchange where the driving force is a slow diffusion reaction between the two pure hydrates. In the first stage, the initial CH_4 hydrate will decompose partially caused by increased temperature and the difference in chemical potentials will lead to an exchange. Also, CO_2 will form CO_2 hydrate with the released water in a continuous formation-dissociation process.

Factors influencing the replacement reaction/controlling mechanisms

Multiple coexisting processes take place during $CH_4 - CO_2$ replacement, including heat release, dissolution of the participating components into different phases, volume change and mass transport (Jung *et al.*, 2010). Experimental data reported in literature indicates that replacement increases near pure CH_4 hydrate equilibrium and with higher injection pressure. Replacement is also highly dependent on hydrate- and water saturation respectively. A higher surface contact area allows for more CO_2 to react with water in proximity to hydrate. The advantage is it will release more heat when CO_2 forms with water and can extend as far as $\sim$ 10 K inside the GHSZ. A pore network consists of several heterogeneities and these can limit the continuous heat release to $\sim$ 3 K. On reservoir scale, high water saturation poses a potential risk for early clogging and will be discussed in the next section.

The solubility to a component in a liquid phase is pressure and temperature dependent. The solubility of CO_2 and CH_4 in water affects mass transport, hydrate formation and hydrate dissolution when water is not saturated with gas. CO_2 is 10 times more soluble in water compared to CH_4 and CH_4 is highly soluble in liquid CO_2. This chemical property will make liquid CO_2 attract/absorb water and CH_4 molecules from the CH_4 hydrate until the solubility limit of CH_4 in liquid CO_2 is reached.

1.5.2 Igṅik Sikumi – Fiery Ice - field trial

The Igṅik Sikumi field pilot was conducted to assess the viability of CO_2 - CH_4 exchange in naturally occurring hydrate reservoirs. Conoco Phillips was the operator and it was based on a series of CO_2 – CH_4 exchange experiments conducted in collaboration with the Reservoir Physics Group (Graue *et al.*, 2006; Stevens *et al.*, 2008; Ersland *et al.*, 2010). Prudhoe Bay on the North Slope of Alaska is known for hydrate accumulations beneath the permafrost. Well logs indicated four hydrate-bearing sediments in the target formation with conditions similar to the lab experiments. NMR logging

indicated a pore volume with 75 % hydrate saturation and 25 % water. High water saturation posed a risk of early CO_2 hydrate formation and clogging in the near well-bore area. In addition, the weight of liquid CO_2 would exceed the formation fracture pressure posing the risk of pore collapse. The operational concerns around liquid CO_2 led to the decision to dilute the liquid CO_2 with nitrogen. Simulation studies concluded that a gas mixture of 77 mol% N2 + 23mol% CO_2 was predicted to give the optimum injection- and exchange strategy (Schoderbek *et al.*, 2012).

The field trial was carried out as a four-phase production plan: 1) unassisted flow back, 2) jet pumping above methane hydrate stability pressure, 3) jet pumping near methane hydrate stability pressure, 4) jet pumping below methane hydrate stability pressure. A thirteen days injection of approximately 210 Mscf, resulted in a total of 998 Mscf produced gas where CH_4 accounted for 82 % of the recovered total volume. Approximately 70 % of the N2 was recovered and more than 50 % of the injected CO_2 was sequestered in the formation. Nitrogen proved to be an effective component to increase sweep and to avoid early clogging. The field trial was regarded as a success and demonstrated the potential of CO_2 storage in hydrate sediments in permafrost regions and the commercial viability of $CO_2 - CH_4$ exchange.

2 - Literature review

This chapter deals with previous research on the formation and dissociation of hydrates in micro models. The review on CO_2 exchange with methane hydrate is mostly in bulk volume and on core scale due to limited research in micro models. This literature review summarizes research on gas hydrates with components relevant to this thesis.

2.1 Hydrate formation in micromodel

Tohidi (Tohidi *et al.*, 2001) was the first to observe hydrate formation and dissociation in a synthetic porous network. They used a synthetic 2D micromodel with similar properties to the model used in this thesis. Single component hydrates were formed from free gas methane (CH_4) and gaseous carbon dioxide (CO_2) dissolved in water. In a methane-water system, there was a rapid formation and growth where gas was encapsulated at the water-gas interface. Hydrate formed at the water-gas interface and trapped gas bubbles in the form of a hydrate crust. The same hydrate crust enclosing methane gas collapsed as the trapped gas converted to hydrate. Besides, they discovered that hydrate could form with gaseous CO_2 dissolved in water. Hydrate growth formed a tendril and cross-hatched morphology which describes supersaturated conditions. For each system, they observed hydrate accumulation in the center of the pores and a thin water film coating the grains. This water-wet phenomenon limits the potential of sediment cementation. They observed sediment cementation only in regions where gas hydrates occupied most of the pore volume, or in areas where grains were small.

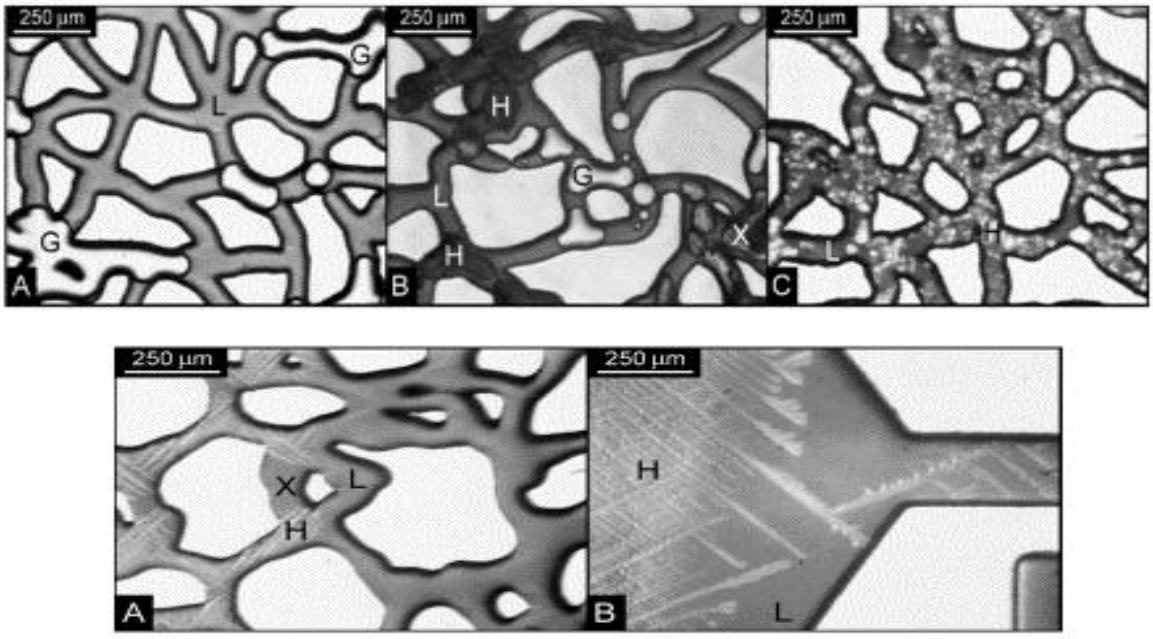

Figure 2-1 - Upper sequence shows methane hydrate formation and lower sequence shows hydrate growth in water with dissolved CO_2 ($Tohidi\ et\ al.$, 2001). Upper sequence: A) Water represented with L, methane gas represented with G prior/before hydrate formation. B) Hydrates represented with H, methane gas represented with G and X represents a thin hydrate film. C) Crystalline hydrate structure. Lower sequence: A) Hydrate growth in water represented by H and L respectively. X shows a bypassed pore are where no hydrates formed. B) Parallel ridges intersecting at 105°-110°

Katsuki (Katsuki *et al.*, 2007) used a similar synthetic model as Tohidi, but they used a micromodel with straight channels arranged in a grid pattern. The model was filled with gaseous methane and saturated water kept at constant pressure, 101 bar. They investigated 4 systems with different degree of subcooling, $\Delta T_{sub} = 3.4\ K, 6.7\ K, 12.3\ K, 14.1\ K$. At subcooling equal 6.7 K or lower, they observed the growth of faceted crystals that bridged the pores. The formation of hydrate occurred at the water-gas interface. Resolution limitation of fewer than 1 μm, made it likely that liquid water layers between the physical bonding and the glass walls of the porous medium were undetectable by the visual observation equipment.

At subcooling, equal 12.3 K or higher they observed that hydrate formation appeared dendritic before they transformed into hydrate crystals. They did not see any channel bridging because methane supply was the limiting factor.

Almenningen (Almenningen *et al.*, 2018b) studied hydrate formation by CO_2 sequestration in a micromodel with analogue pore network to sandstone. The micromodel was saturated with distilled water at 70 bar and 1.3 °C. CO_2 was injected at a constant volumetric flowrate of 0.5 ml/h. They observed nucleation of solid hydrates initiated at the liquid CO_2 – water interface. This growth was slow and propagated through the water phase, contrary to methane hydrate. Hydrates crystallized in

water-filled pores and growth in the CO_2 phase continued slowly until growth ceased due to lack of water. In the end, liquid CO_2 was left immobilized by surrounding hydrates. The result shows that crystalline hydrate formation in water can create an effective barrier to buoyancy. A further supply of CO_2 will, in time spread laterally and the extent of the barrier will increase. Hydrates as a physical barrier enable cold aquifers as prospects for CO_2 sequestration.

2.2 Hydrate dissociation in micromodel

Tohidi (Tohidi *et al.*, 2001) dissociated the two introduced systems in section 2.1. The hydrate systems dissolved gaseous CO_2-water and methane gas-water, completely dissociated by thermal stimulation. In the methane-water system, parts of the CH_4 hydrate broke free and became mobile within the liquid phase. After complete dissociation, small crystalline structures remained in the system, even though the system was outside the GHSZ. The cause of residual hydrate probably has to do with the self-preservation effect. In the case of CO_2 hydrate system, all hydrate crystals returned to single-phase liquid and complete dissociation of the CO_2 hydrates. Gas bubbles evolved when the pressure was reduced below 0.69 MPa at room temperature.

Katsuki (Katsuki *et al.*, 2008) presented visual observation of hydrate dissociation in a glass micromodel with straight channels. They dissociated the system by thermal stimulation and depressurization. They observed methane bubbles forming on the hydrate crystal surface during thermal stimulation. These bubbles diffused through liquid water to bigger bubbles which further increased to slugs of gaseous methane filling pore channels $1.0\ x\ 10^2\ \mu m$ in diameter. In the case of depressurization, small bubbles of methane (in the range of $[10 - 20]\mu m$) formed in the liquid phase and developed into larger slugs when the hydrate continuously dissociated and released more methane bubbles.

Almenningen (Almenningen *et al.*, 2018a) studied the dissociation of CH_4 hydrate formed in water with increasing salinity in a silicon micromodel. Depressurization and thermal stimulation of crystalline hydrates and hydrate films showed different dissociation patterns. Different dissociation patterns were explained by how the pressure gradient propagated through the media. The pressure gradient transferred through wetting films inducing dissociation in pore corners for crystalline systems formed by distilled water. Whereas the pressure gradient induced hydrate film dissociation in the center of the pores. Also, results showed that hydrate stability increased by increased salinity.

2.3 Exchange

The utilization of CO_2 is regarded as a promising production technique of gas hydrates. It has attracted attention from researches all over the world. Low replacement efficiency and slow replacement rate combined with the economic aspect makes the injection strategy uncommercial on field scale.

Research on the exchange mechanisms is mainly conducted on core scale and in bulk conditions. The term bulk condition means when the exchange process is done in a medium without any impact from foreign/unknown particles. The study of this reaction started in the 1990s and is currently drawing interest all over the world. Englezos (Englezos, 2019), a highly recognized researcher in the field of NGH reports that there is high variability in reported exchange results. This section will cover research on methane hydrate exchange with CO_2 in liquid- and gaseous state.

2.3.1 Exchange with gaseous CO_2

Ohgaki (Ohgaki *et al.*, 1994) was the first to study exchange between gaseous CO_2 and methane hydrate, and later on with liquid CO_2 (Ohgaki, 1996). They showed the concentration of CO_2 increased in the hydrate phase compared with its gas phase for a CH_4 and CO_2 hydrate in a bulk system.

Uchida (Uchida *et al.*, 2001) used Raman spectroscopy to study the exchange and proved that the exchange reaction occurs on the contact surface between CH_4 hydrate and CO_2 gas. They suggested that the replacement rate is prolonged and induction time can take up to several days. Later they measured the composition ratio between CH_4 and CO_2 in the gaseous phase (XCH_4/XCO_2) at various times during the formation of mixed gas hydrates. They found that CH_4 molecules always occupied the small cavities and large cages were occupied by CO_2 molecules.

Ota (Ota *et al.*, 2005a) used a high pressured cell, gaseous CO_2 and Raman spectroscopy. They performed experiments at [31, 32.6, 33.4] bar at [271.2, 273.2, 275.2] K. They showed that the amount of decomposed methane hydrate was almost proportional to the consumed CO_2. This means most of the replacement happened in the hydrate phase. Moreover, they found that the driving force of replacement was the difference in fugacity (difference in chemical potential). Based on activation energies during replacement, they concluded the dissociation of CH_4 hydrate was dominated by rearrangement of water molecules in the hydrate structure. While for CO_2 hydrate formation, the dominant process was diffusion into the hydrate phase.

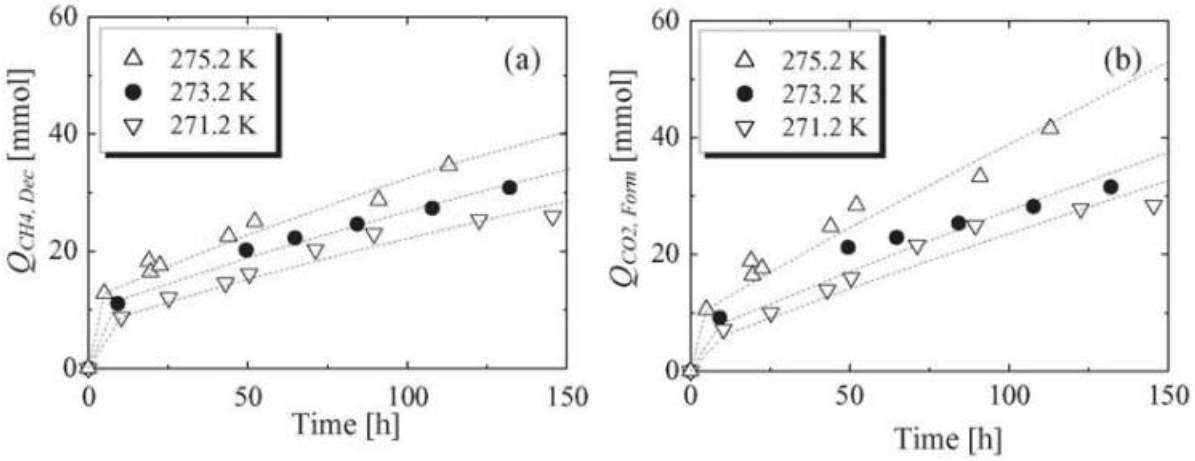

Figure 2-2 – Amount of decomposed CH_4 hydrate to the left and amount of formed CO_2 hydrate to the right (Ota, Abe, et al., 2005).

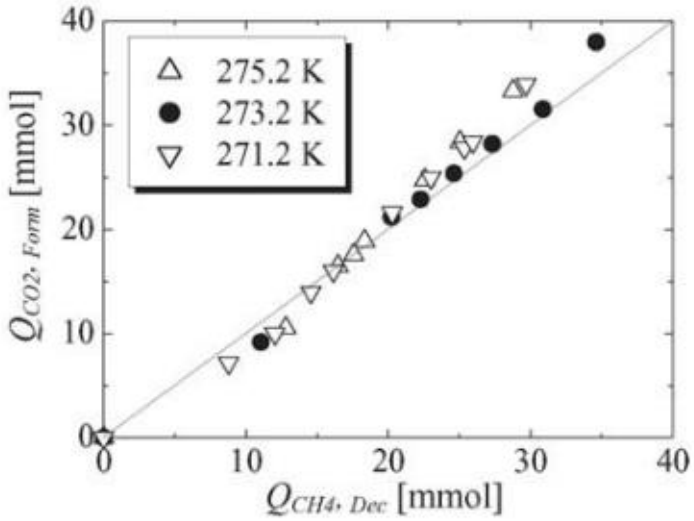

Figure 2-3 – Plot of decomposed CH_4 hydrate vs consumed CO_2 at 32,6 bar(Ota et al., 2005a).

Yuan (Yuan *et al.*, 2012) used a high-pressure reactor with an inner diameter of 300 mm and a height of 100 mm. They created a hydrate reservoir with underlying free gas, by using a porous stainless-steel sheet to separate the reactor with an upper layer sediment and underlying layer free gas. This model was submerged in a cooling bath containing aqueous glycol solution to withstand generation of ice at temperatures below freezing point. They formed a sand reservoir in the upper layer of the reactor, by mixing frozen quartz sand and a known amount of sodium sulphate (Na_2SO_4). They prepared three different hydrate samples at 274.7 K at 30 bar simulating three classes of hydrate reservoirs to investigate favourable methane recovery conditions. In the first run, the reactor was not separated. They prepared the hydrate sample with water saturation, gas saturation and hydrate saturation at 23.7 %, 51.5 % and 24.8 % respectively. In the next two experiments, they separated

the reactor to simulate reservoir conditions with underlying free gas. For run 2, the hydrate sample had water saturation, gas saturation and hydrate saturation at 27.6 %, 61.7 % and 10.7 % respectively. For run 3, the hydrate sample had water saturation, gas saturation and hydrate saturation at 1.1 %, 91.0 % and 8.9 % respectively.

High water saturation in run 1 and 2 showed unfavourable conditions for CO_2 - CH_4 exchange. Gaseous CO_2 was consumed by water and formed pure CO_2 hydrate, so only a small fraction of the gaseous CO_2 could react with the CH_4 hydrate. A system with low water saturation and a large amount of CO_2 in the gas phase showed favourable exchange conditions. With these conditions, most of the CH_4 hydrate got converted into a mixed CO_2-CH_4 hydrate. Figure 2-7 in section 2.3.2 compares the experiments Yuan (Yuan *et al.*, 2012, 2013) did with liquid and gaseous CO_2. Figure 2-4 shows the following plots in ascending order; gaseous CO_2 experiment done by Ota, two different experiments with liquid CO_2 done by Zhou and Ota, run 3 with gaseous CO_2 done by Yuan and three emulsion experiments done by Zhou. Comparing Figure 2-4 and Figure 2-7 shows that Yuan obtained a higher replacement percent in run 3 (gaseous CO_2) than Ota (Ota *et al.*, 2005a; Ota *et al.*, 2005b) and Zhou (Zhou *et al.*, 2008) did in their experiments with gaseous and liquid CO_2. The result in run 3 contradicts literature since CO_2 in the liquid state gives a higher replacement percent. The reason they obtained such high replacement values was a pressure reduction to 30 bar before injection of gaseous CO_2. This made an unobstructed pore network, which had a lower resistance for CO_2 to diffuse in the sediment.

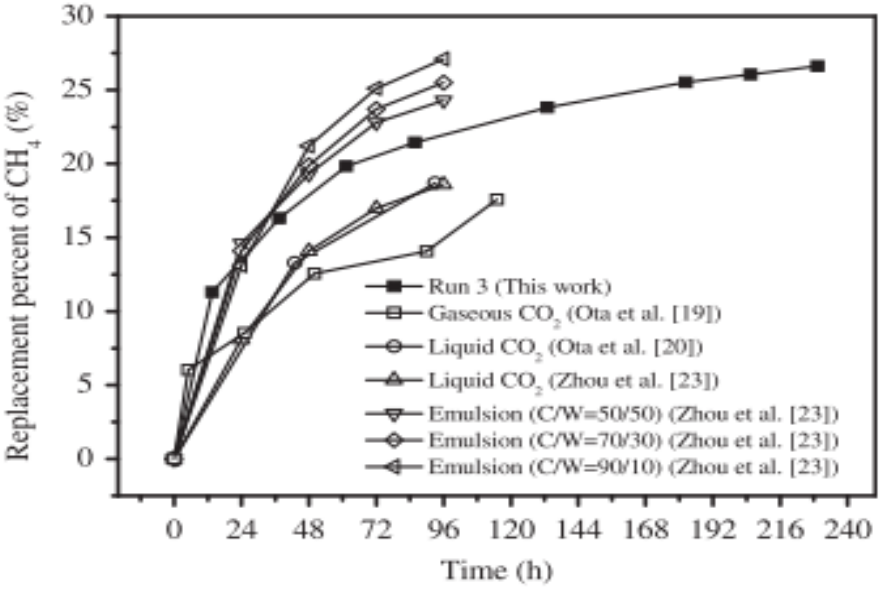

Figure 2-4 - Comparisons of replacement experiments (Yuan *et al.*, 2012)

2.3.2 Exchange with liquid CO2

Ota (Ota, *et al.*, 2005b) used Raman spectroscopy to analyse the exchange with liquid CO_2 in a high pressure optical cell at 273,2 K. After 307 hours they recovered 35 % of the CH_4. The results showed the amount of decomposed CH_4 hydrate was close to the same amount of formed CO_2 hydrate. In addition, with the use of Raman spectroscopy, they made a kinetic model for calculation of the remaining CH_4 in the different cage structures. The model showed there was remaining CH_4 in the small cages compared to large cages. Secondly, it showed that CH_4 occupying small cages decomposed at a much slower rate than large cages occupied by CH_4. This indicated that the driving force for the exchange reaction is the difference in chemical potential between the component in the fluid phase and the component in hydrate phase.

Yuan (Yuan *et al.*, 2013) used liquid CO_2 and the same setup described in chapter 2.3.1 to investigate the exchange mechanisms. Hydrate gradually form in the sediment when CH_4 was injected at 275.2 K and 95 bar. After the preparation phase, they lowered the pressure to the equilibrium pressure to pure CH_4 hydrate before liquid CO_2 was injected. The experimental conditions for all five experiments are in the table below.

Table 2-1 - Experimental conditions (Yuan et al., 2013)

Runs	Temperature (K)	Pressure of CO_2 (MPa)	Void volume (L)	Water consumed (g)	CH_4 consumed (mol)	Initial CO_2 (mol)	Water saturation (%)	Hydrate saturation (%)
1	275.2	4.21	3.26	372	3.44	52.46	5.42	19.7
2	275.2	4.20	3.26	576	5.33	50.88	0.17	30.5
3	275.2	4.21	3.26	367	3.40	47.62	16.44	19.4
4	280.2	4.20	3.26	366	3.38	52.45	5.68	19.4
5	275.2	4.19	2.71	321	2.97	42.43	11.82	17.0

The highest amount of recovered CH_4 and replacement rate were obtained in experiment 2 because the high hydrate saturation made the largest surface area for liquid CO_2 to contact CH_4 hydrate. Moreover, they found that the rate and amount of replaced CH_4 increase with a higher hydrate saturation, even though replacement percent in CH_4 hydrate increases with a lower hydrate- and higher water saturation. This suggests that heat release from pure CO_2 hydrate formation will liberate most methane from a long-term perspective. Also, the fugacity difference of liquid CO_2 in contact with methane hydrate creates a faster initial replacement.

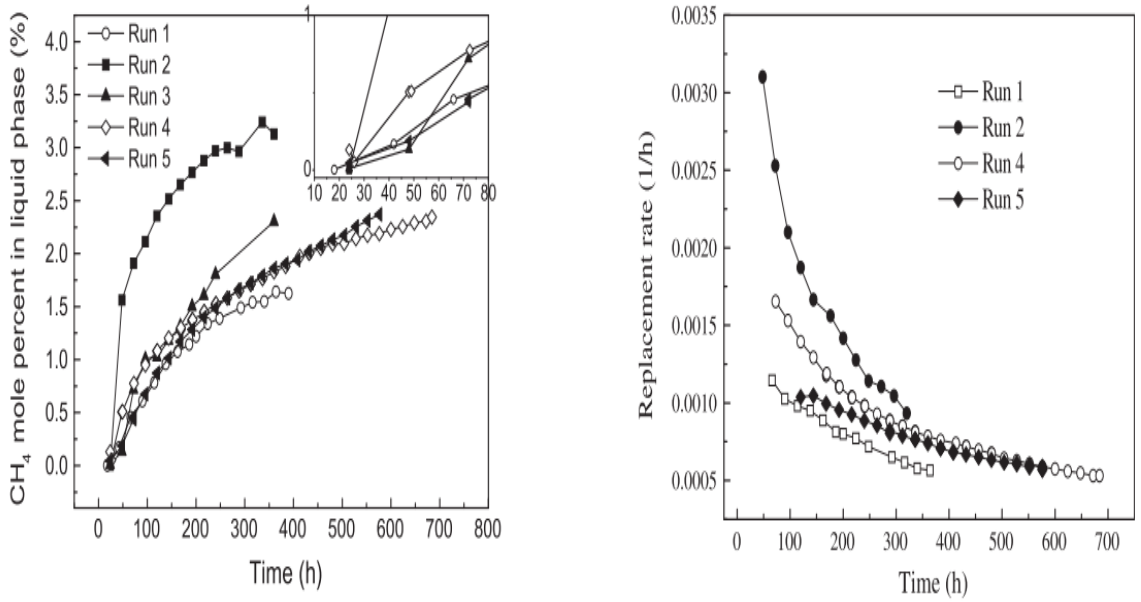

Figure 2-5 - Plot to the left shows the increase of released CH_4 over time. Plot to the right shows the rate of replacement over time (Yuan et al., 2013)

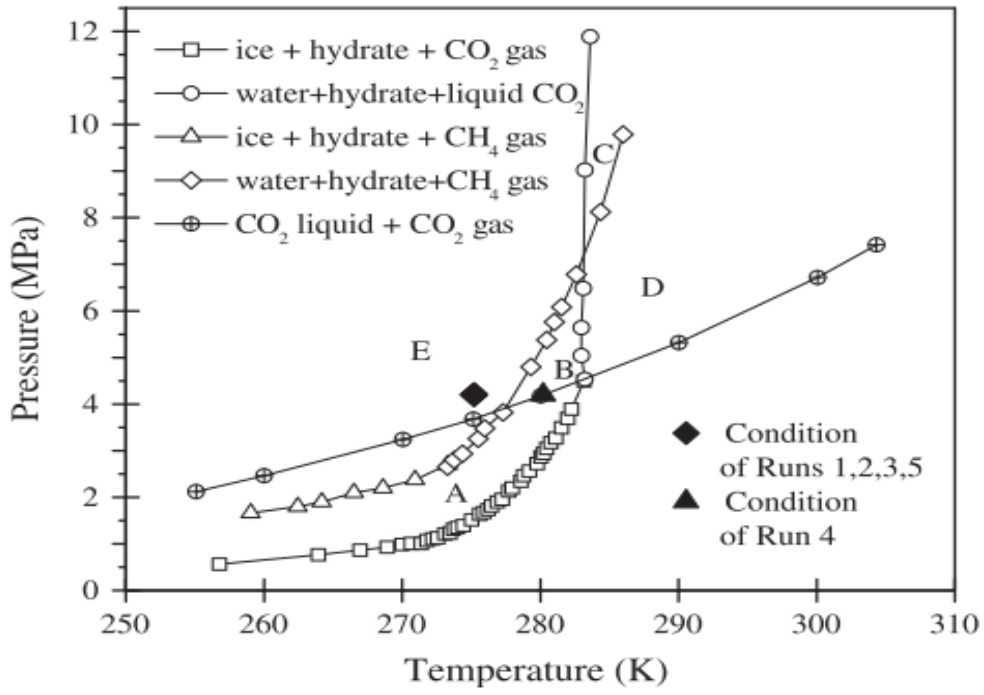

Figure 2-6 - Stability zones for different conditions of hydrates, showing that optimum exchange conditions are in zone B with liquid CO_2 (Ohgaki, 1996).

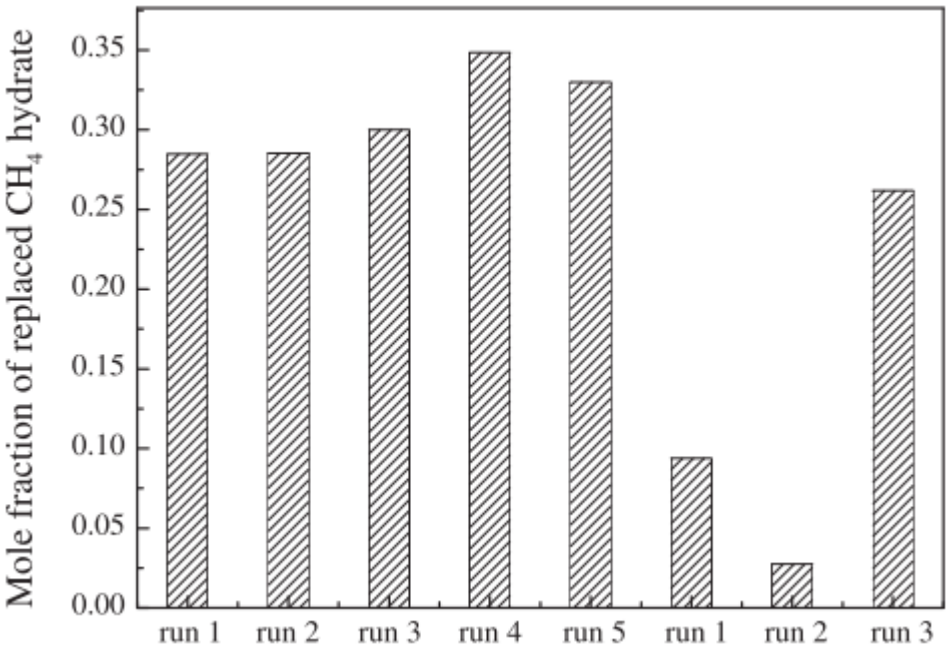

Figure 2-7 – Mole fraction of replaced methane in the hydrate phase comparison with injected liquid CO_2 in run 1-5 and gaseous CO_2 in run 1-3 (Yuan et al., 2013)

Ersland (Ersland *et al.*, 2010) exposed CH_4 hydrate to liquid CO_2 and utilized magnetic resonance imaging (MRI) to visualize the exchange mechanisms. MRI detects hydrogen molecules and distinguishes liquid water and solid hydrate. The MRI will not detect hydrogen in the hydrate phase, but the hydrogen in pure water and CH_4 make a strong MRI signal. The MRI allowed them to study CH_4 hydrate formation and injection of CO_2 in a sandstone core. The sandstone core consisted of two half-cylindrical cores separated by a spacer. Use of a spacer made rectangular holes allowing easy transport of water and gas through the core. The spacer caused an increased surface area for CO_2 to imbibe for an exchange. Additionally, the spacer avoided signal contribution from the water and made the right conditions for measuring MRI intensities of the mixed CO_2-CH_4 composition. They obtained results where diffusion processes appeared to be the dominant driving mechanism in supplying CO_2 to the CH_4 hydrate, together with the apparent absence of large-scale hydrate melting during the exchange.

3 – Materials and methods

The lab work, data acquisition and analysis have been conducted at the Department of Physics and Technology at the University of Bergen. The next section emphasizes the experimental setup for hydrate formation, liquid CO_2 injection and hydrate dissociation as well as the characteristics of the silicon micromodel. Section 3.2 describes the experimental procedure, section 3.3 provides details on the optic features and explanation of the image output. Section 3.4 explains the quantitative analysis in this work.

3.1 Experimental setup

The experimental setup was adapted from previous MSc (Iden, 2017; Lysyy, 2018) and PhD (Hauge *et al.*, 2016; Almenningen *et al.*, 2017) students. Necessary adjustments were made to create a multicomponent system. Overview of the experimental apparatus and fluids are illustrated in Figure 3-1 and the next page.

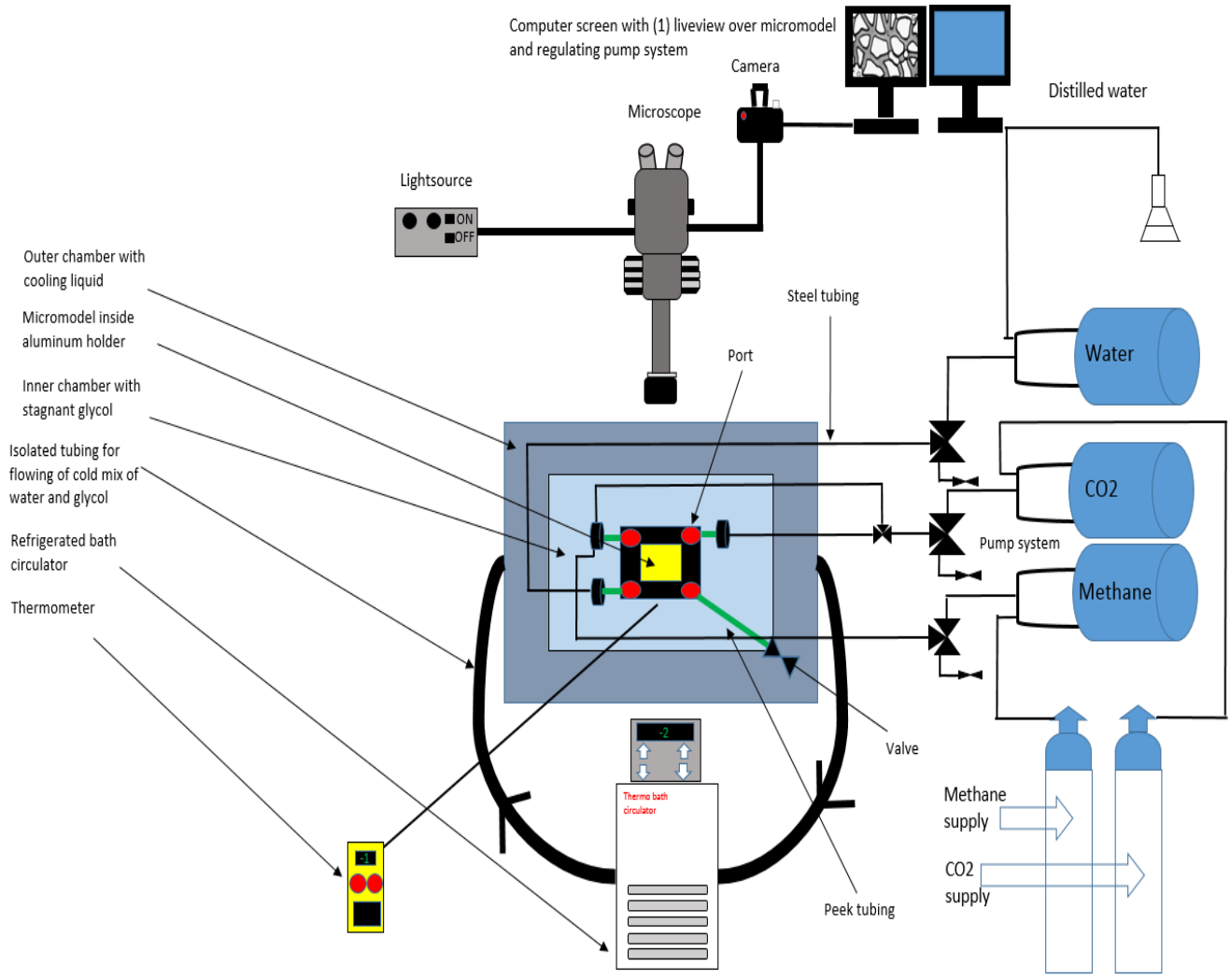

Figure 3-1 – Experimental setup showing all parts in the setup.

Apparatus:

- High-pressure micromodel
- Quizix Q5200 pump system
- Aluminum holder
- 1/16'' PEEK (polyetheretherketone) and 1/8'' steel tubing
- Dual cooling chamber
- Thermo Scientific Neslab RTE 17 refrigerated bath circulator
- Propylene glycol-based antifreeze by Camco
- HH506RA Omega Multilogger thermocouple
- Nikon SMZ11500 microscope
- Photonic LED F1 Cold light 5500K light source
- NikonD7100 camera

Experimental fluids:

- Distilled water
- Methane gas from YaraPraxair with $\geq$ 99.5 purity
- CO_2 from YaraPraxair with 99.9 % purity

Micromodel properties

The micromodel used in the experiments was capable of withstanding pressures up to 150 bar and is produced by Pharmafluidics. The micromodel replicates the pore network in Berea sandstone with an average pore diameter of 100 μm and dimensions 2.8 cm x 2.2 cm x 0.0025 cm(Lysyy, 2018). The micromodel consists of two main parts. The bottom part is made of a silicon wafer anodically connected to a top part made of borosilicate glass. The porous network is etched in the silicon wafer by a DRIE (Deep Reactive Ionic Etching) technique. This makes a realistic representation of geometrical and topological rock properties such as sharp corners, rough pore walls and high aspect ratio (i.e. the ratio of pore body to pore throat). As a result of the manufacturing procedure, the micromodel is water-wet. The micromodel has four ports on the backside, allowing for the opportunity to inject and produce fluids. Hornbrook (Hornbrook *et al*., 1991) and Buchgraber (Buchgraber *et al.*, 2012) provide a more thorough description of the manufacturing procedure.

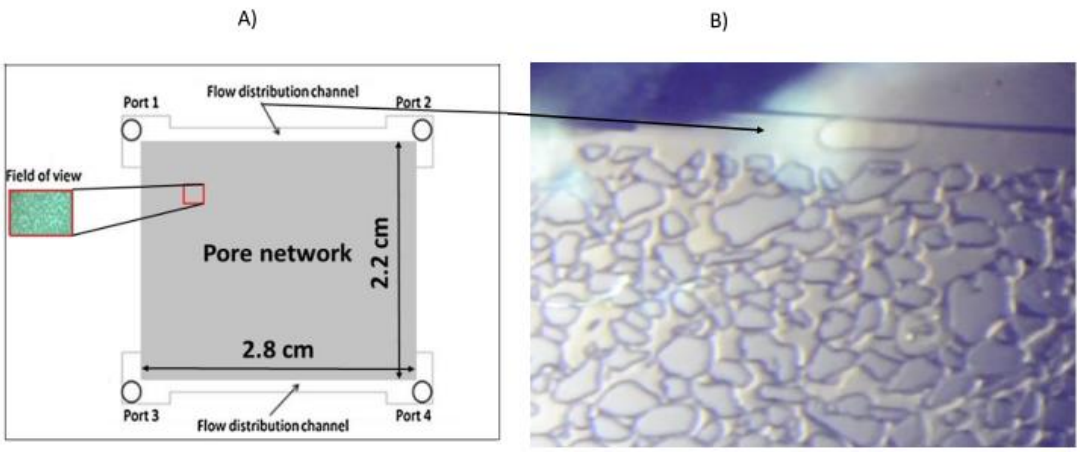

Figure 3-2 – Bird-eye view of the micromodel showing the structure of the grains, pores and location of high permeable channels. The ports are in the four corners and pore network pattern is repeated 36 times. Field of view refers to the area visual through the microscope and represents around 1 % of the entire pore network. Modified from (Lysyy, 2018). *B) Cropped and magnified microscopic view with a low zoom ratio (the used zoom ratio was 5 X) showing a gas bubble flowing in the upper high permeable channel.*

Experimental design

The micromodel was placed inside an aluminium holder and submersed in a dual cooling chamber. The cooling chamber consisted of an outer- and inner cooling chamber. The inner part was filled with stagnant glycol or distilled water, whereas a cooling liquid circulated in the outer chamber. A refrigerated bath circulator provided the cooling liquid in the outer chamber to maintain a cold and constant temperature. An aluminium barrier separating the inner and outer chamber made sure of efficient heat transfer between the chambers.

The Quizix Q5200 pump system consisted of three separate pump cylinders operating independently of each other. Each cylinder was filled with; distilled water, methane gas and CO_2. These components were used to saturate the porous media and to acquire target pressure. To operate the pump reasonably, two operating modes were utilized: constant pressure mode (to maintain constant pressure) and constant volumetric flow rate mode (to inject and extract fluids). For the micromodel to communicate with the pump system, PEEK tubes were connected to the steel tubing. Three cylinders were connected in three different ports of the micromodel. Water supply was connected in the bottom left of the model and methane supply was connected in the top left. The supply of CO_2 was connected to the top right port and the top left port. It allowed injection of CO_2 from the same port as methane but entering the valve from the opposite side. This made it possible to inject CO2 from multiple ports to see how this could affect an injection into the porous media. This setup ensured the distribution of multiple components in the model.

The temperature was monitored by a thermocouple placed in the still water directly beneath the micromodel. The thermocouple was placed underneath the model to minimize the effect of room temperature. Flatlandsmo (Flatlandsmo, 2015) utilized a similar experimental setup and briefly evaluated the heat transfer through the model with a general conclusion that the temperature in the still water and micromodel could be assumed equal.

A camera was mounted on top of the microscope which provided direct visual observation of the hydrate behaviour through images or videos. Interval shooting was not preferred to gather observational data due to vibrations caused by the circulating water. Vibrations caused an unintentionally focus adjustments that made images blurry if the laboratory was unattended for a period. This made capturing hydrate behaviour overnight disadvantageous. A computer screen connected to the camera provided improved live-view monitoring of the micromodel. A cold light source illuminated the area in focus, this ensured conditions for obtaining high quality data. The area in focus called the Field of View (FOV) is from here and now called the FOV.

3.2 Experimental procedure

This section provides a description of the procedures for mixed hydrate formation, CO_2 injection into a micromodel with CH_4 hydrate and mixed hydrate dissociation.

Best practice

Acquire both components in FOV proved to be difficult and even more challenging to form hydrate at static conditions. A couple of procedures were carried out seeking the most efficient procedure to form hydrate with both components in the FOV. The following steps describe the most efficient mixed hydrate formation procedure.

1. Cylinder A, B, C were filled with distilled water, methane gas and pressurized liquid CO_2 respectively.
2. Micromodel was flushed with distilled water to remove residual components, CH_4 and CO_2.
3. The system was carefully pressurized by water. Pressurizing the system too fast can cause cracks in the micromodel.
4. Valve connecting water pump to model was closed.
5. Camera recording was started every 30 minutes to monitor fluid behaviour.
6. The system was injected and further pressurized by either CH_4 or CO_2, this ensured the pores were saturated with one component.
7. The pressure was increased by constant volumetric flowrate mode until target fluid saturation in the porous media was reached.

8. Valve connecting the first injected component to the model was closed and the pump was set to constant pressure mode.
9. The second component was pressurized 5 or 10 bar higher system pressure. Opening the valve allowed the second component to invade the pore network and redistribution of the components.
10. The valve to the second injected component was closed. Methane pump was set to the same pressure as the invasion pressure of the second component and the valve opened to maintain constant pressure in the system. If methane was injected as the second component, no action was needed.
11. Refrigerated bath circulator was turned on to cool down the system to target temperature.
12. Observation of hydrate formation.
13. In case of no visible hydrate formation under static conditions within 24 hours, both pumps were set to equal pressure in constant pressure mode and both valves were opened. The system was agitated by cautiously opening the valve connecting the system to atmospheric pressure (port 4) to generate a small pressure pulse through the model.
14. Agitation resulted in a redistribution of components, which in turn caused mixed hydrate formation within a few minutes.

CO_2 injection procedure

The procedure was as follows;

1. Cylinder A, B, C were filled with distilled water, methane gas and pressurized liquid CO_2 respectively.
2. Micromodel was flushed with distilled water to remove residual components (capillary effects).
3. Refrigerated bath circulator was turned on to cool down the system to a target temperature.
4. The system was pressurized by water reaching target pressure.
5. The valve connecting the water pump to model was closed.
6. The camera was set to record.
7. The methane pump pressure was set equal to the system pressure.
8. Valve connecting methane cylinder to the system was opened and pump set to constant pressure.
9. The system was agitated by cautiously opening the valve connecting the system to atmospheric pressure (port 4) to generate a small pressure pulse through the model. This allowed methane to flow from the pump through the model and form methane hydrate fast. The system was left for many hours to let the system stabilize and prepare for CO_2 injection.

10. CO_2 pump pressure was set equal to system pressure.
11. Valve connecting CO_2 to the model was opened.
12. CO_2 was injected at a constant volumetric flow rate.
13. Valve connecting CO_2 to the model was closed when methane pump stopped retracting volume. This was observed by close surveillance of the Quizix Pump program.

Hydrate dissociation procedure

After mixed hydrate formation, the system was left for 24 hours to ensure the formation of a stable hydrate system. The system was depressurized by using a "lab-on-chip" method in order to study hydrate phase equilibria (Almenningen *et al.*, 2017). The pressure was always reduced through methane pump at a constant temperature.

1. The methane pump was retracted at constant volumetric flow rate, 10 ml/hr, until reaching one bar above pure CH_4 hydrate equilibrium. If the liquid/gas boundary to CO_2 was above pure CH_4 hydrate equilibrium, the pressure was reduced one bar above this pressure. Pore network was monitored through video recordings every 30 minutes.
2. Methane pump was set to a constant pressure, and the system was left at each pressure step to observe hydrate behaviour and dissociation.
3. Methane pump retracted at constant volumetric flow rate, 0.1 ml/hr until next pressure step was reached, one bar below the previous pressure step.
4. Step 2-3 were repeated until reaching pressure one bar below the equilibrium pressure to pure CO_2 hydrate.
5. Hydrate dissociation was recorded until no hydrate were visually detected in the pores.

In between each experiment, methane cylinder was depressurized to atmospheric conditions and vacuumed to remove residual components in the pump.

3.3 Optics

The experimental data was obtained through the investigation of videos acquired from the camera installed in the microscope. This section describes the optical properties, limitations and the description of the qualitative data analysis.

Microscopic view

In the micromodel, there are multiple phases and components present. This forms complex pore networks because the different components and phases make different hydrate configurations. For data interpretation, it is essential to understand physical chemistry and light propagation through the media to distinguish components, configurations and compositions. The phases present in the FOV

will be are and is illustrated Figure 3-3; grains, distilled water, methane, hydrate film, crystalline hydrate, liquid CO_2 and gaseous CO_2. The major drawback with this setup is that it is impossible to analyse the dissolution of each component in other phases. This makes compositional analysis before formation and during dissociation impossible.

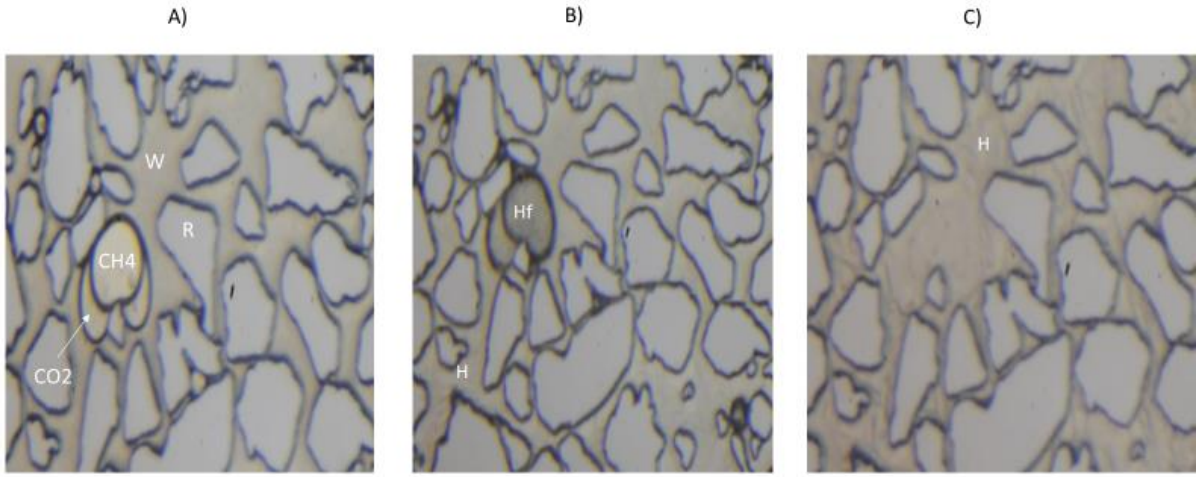

Figure 3-3 - View of the pore network through the microscope where six media are present: water, grains, methane, liquid CO_2, hydrate film and hydrate crystals. They are denoted as W, R, CH_4, CO_2, Hf and H respectively. A) methane gas bubble on top of liquid CO_2 droplet prior to formation. B) hydrate film has encapsulated methane and CO_2 and hydrate crystals have started to grow in water in the bottom left. C) Bubble and droplet have been consumed to grow into crystalline hydrate. Hydrate crystals appear as transparent crystal structures, whereas hydrate film configuration appears black.

Table 3-1 shows the refractive index for the different components present in the images obtained in this thesis. The refractive index describes light propagation through a medium. If two non-absorbing materials cannot be distinguished visually, they will have the same refractive index. In contrast, if materials can be distinguished visually they will have different refractive indexes (Bylov and Rasmussen, 1997). The water-wet nature of the micromodel makes methane gas form a convex curvature toward grains and water. CO_2 can exist in different states and its refractive index will thereby change when pressure is increased or decreased below its liquid/gas boundary.

Table 3-1 – Refractive indexes for media represented in this work

Media	Refractive index n	Reference
Methane gas	1.000	(TheEngineeringToolbox, n.d)
Water	1.333	(TheEngineeringToolbox, n.d)
Crystalline Methane hydrate	1.346	(Bylov and Rasmussen, 1997)
CO_2 gas	1.001	(Morgan, 1953)
CO_2 liquid*	1.20 – 1.25	(Guo *et al.*, 2006)

*The density of liquid CO_2 changes with pressure and temperature. Refractive index of CO_2 is a function of CO_2 density ranging from (0.85 – 1.05) [g/ml] at 25 ^oC.

The difference in refractive index between crystalline methane hydrate and water is [0.013]. The amount of reflected light causes the difference in refractive index at the interface of fluids and the bottom wafer in the micromodel. Sequentially, the light will propagate through both phases and bottom wafer in micromodel and reflects light to the microscope. This small value makes water and crystalline methane hydrate almost identical and is differentiated by crystal structures in water, as illustrated in Figure 3-3 (C). In contrast, the difference between CH_4 gas and hydrate film enclosing CH_4 gas is striking. CH_4 gas below hydrate films causes the light to be bent and reflected at fluid interface, causing dispersion of light. This leads to small amounts of reflected light back to the microscope and the appearance of dark hydrate films.

Image quality

The images presented in this work are of different colour and brightness. These two properties are affected by multiple factors such as the fluid in the inner chamber, microscope magnification, camera settings, system pressure, and internal and external light sources.

Glycol and distilled water have different densities and were both utilized in the inner chamber during the experimental work. High pressure in the model can cause the top wafer to slightly elevate/bulge affecting the angle of the incoming light.

Data was acquired through video recordings, and the images presented are snapshots from these videos. Camera settings utilized for video recordings: F13 aperture, 1/30 shutter speed, 6700 ISO. These settings made it possible to achieve high-quality data suitable for hydrate analysis.

The microscope magnification ability has a zoom ratio ranging from 0.75X to 11.25X. Ideally, all light from the light source should converge through the microscope and enlighten one specific area. Limitations in the microscope cause the light to diverge, making an uneven illumination of the micromodel. The uneven illumination generates a sharper focus in the center of images and shadows in each corner. The effect is diminished by increased magnification. Zoom ratio 5X was used to obtain high-quality data and a representative area of the pore network.

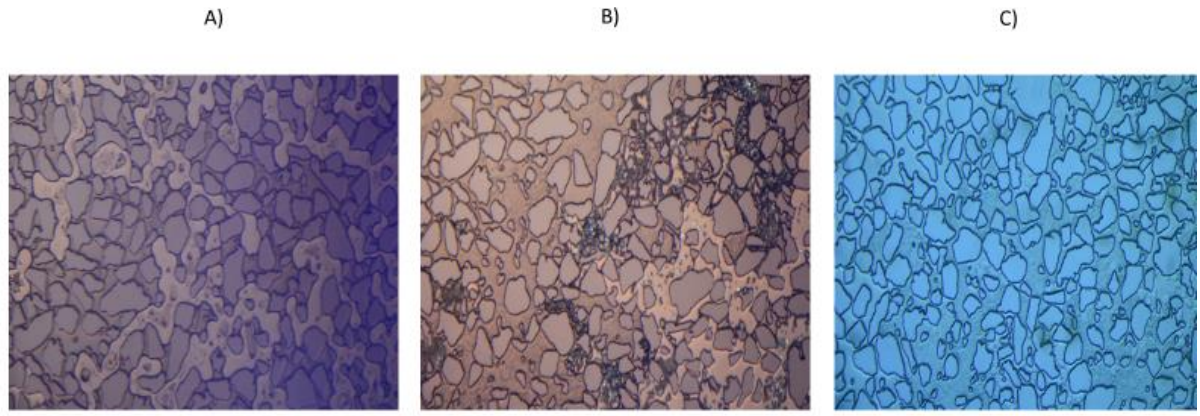

Figure 3-4 - Illustration of different brightness and colours. A) An external light source created a shadow across the right side of the image. B) Snapshot from video recording in the area close to methane port where micromodel is submerged in glycol. C) Snapshot from a video recording in the area close to CO_2 port where micromodel is submersed in distilled water.

3.4 Quantitative analysis

The quantitative analysis studies how the composition in the hydrate changes throughout a stepwise dissociation. The composition in the hydrate was calculated utilizing the hydrate equilibrium software Colorado School of Mines Gibbs Energy Minimization (CSMGem). Also, a two-dimensional saturation estimation was done prior to mixed hydrate formation. The estimated pore volume of the micromodel is 0.01 mL, which is several orders smaller than the volume in tubing (Flatlandsmo, 2015; Iden, 2017; Lysyy, 2018). Consequently, any material balance calculations would be sensitive to small leakages and hydrate clogging in tubing upon CO_2 injection and hydrate formation (Lysyy, 2018). Due to this reason, saturation mapping before and after hydrate formation was estimated through the quantitative characterization of the images utilizing visualization software: Paint.net.

Saturation mapping

Saturation mapping was conducted to evaluate the fluid distribution prior to hydrate formation formation to evaluate if a system could be regarded as, e.g. high water- or high gas saturation system. Images were captured momentarily before hydrate formation initiated and ahead of each dissociation. Hydrate saturations were mapped on the basis that hydrate can appear as black (hydrate film) and transparent (crystalline hydrate) morphology. The two configurations combined were regarded as one single hydrate saturation. A pore is assumed to be saturated by hydrate when hydrate film encloses gas or and liquid phase, despite hydrate films may form above or below the components.

Saturation estimation of a multicomponent system has three main limitations. 1) Saturation before formation does not consider the pore depth and gravity effect of two components. If CH_4 gas flows

on top of liquid CO_2 makes the two-dimensional mapping unfavourable. 2) The illuminated area (FOV) enlighten 1 % of the pore network, whereas global saturation could vary in the entire micromodel. 3) The saturation mapping does not quantify the dissolved amount of each component in the different phases. It is essential to know the composition working with a multicomponent hydrate system.

Paint.net was utilized to calculate porosity and saturation values for each component. Water, CH_4, CO_2 and grains were detected and segmented with separate colours. Each image has a total number of pixels where saturation represents a fraction of the total amount to each component. Paint.net can process raw images and during processing, it colours grains and all phases except water with distinct colours. Porosity was calculated with, equation 3.2, to obtain pore space area. Total image porosity and fluid saturations were estimated through the pixel count analysis, utilizing the following computational formulas:

$$\emptyset_{pore} = \frac{A_{pore\ area}}{A_{tot}} = \frac{N_{pore\ area}}{N_{tot}} = \frac{N_{tot} - N_{grains}}{N_{tot}} \tag{3.2}$$

$A_{pore\ area}$ – area of pore space

A_{tot} – total area of image

$N_{bulk\ area}$ - number of pore area pixels

N_{tot} – total number of pixels in image

N_{grains} – number of grain pixels

$$S_i = \frac{A_i}{A_{pore\ space}} = \frac{N_i}{N_{pore\ space}} \tag{3.3}$$

Where,

A_i – area of a component, (water, methane, CO_2 or hydrate) in the image

N_i – number of a phase pixels (water, methane, CO_2, or hydrate)

Depending on the fluid distribution, the most efficient segmentation method would leave a residual unsegmented component. Since the sum of all components saturating the pore space must be equal unity, the unsegmented component was estimated as the difference between unity and the sum of the segmented components.

Uncertainty calculations would have applied for the two-dimensional area. The standard deviation for a sample set of data would have resulted in an estimated mean uncertainty to be ± 0.07. The uncertainty is not representable for the system and would be higher due to the three limitations mentioned above. It is thereby concluded that the experimental uncertainty is greater than the instrumental uncertainty.

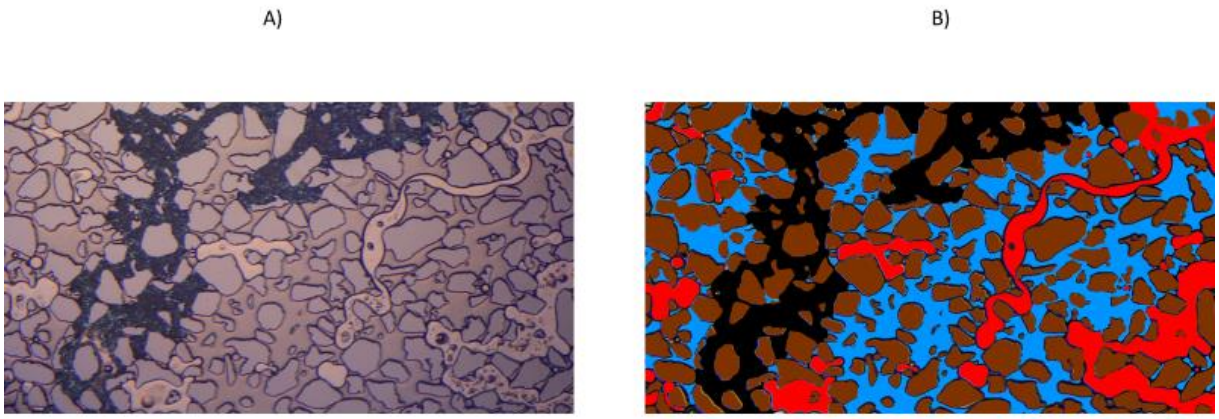

Figure 3-5 – Illustration of saturation estimation utilizing Paint.net. Left: Original image. Right: Processed image with grains, gas, hydrate film and water coloured brown, red, black and blue respectively.

CSMGem

CSMGem predicts the equilibrium pressure at a given temperature for different mixed compositions encapsulated by hydrates. CSMGem was used to study the phase equilibria in the different CO_2 + CH_4 + water systems under hydrate formation conditions. A mixed hydrate will have multiple dissociation points and the released gas can quantify the CO_2/CH_4 composition in the hydrate. The CO_2/CH_4 gas composition was calculated at each dissociation point.

The orange dot in Figure 3-6, represents an observed dissociation point in experiment 8 at 3.5 ^{o}C. However, the orange dot does not represent the correct mole fraction of CO_2 in the gas phase but is plotted to a CO_2 mole fraction value (30 %) for illustration. The blue dots represent the theoretical gas composition in equilibrium with hydrate at different pressures at 3.5 ^{o}C, calculated by CSMGem. To calculate the correct mole fraction of CO_2 in the dissociated hydrate, a second-order polynomial (Poly.(CSMGem) is applied to the theoretical equilibrium values. Utilizing the goal seek function in Microsoft Excel allows fitting experimental data to the theoretical equilibrium pressures, illustrated by the black arrow and grey dots. This will give a representative indication of how the hydrate composition changes during a stepwise pressure reduction.

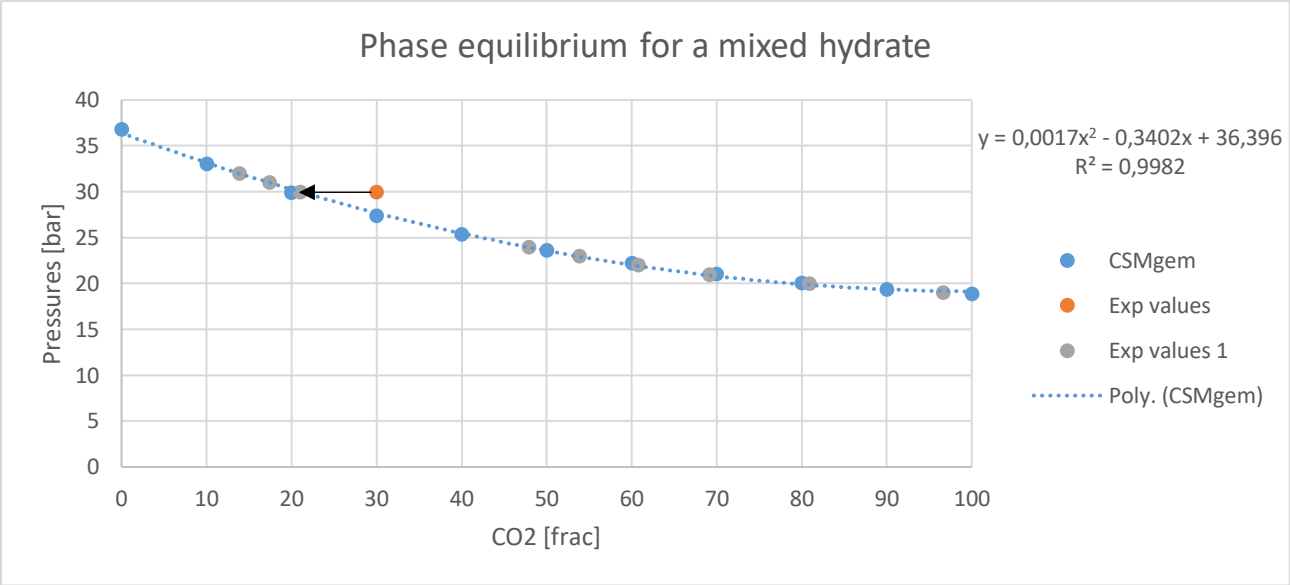

Figure 3-6 - Phase equilibrium for a mixed hydrate composition at 3.5 °C. The X-axis shows mole fraction of CO_2 and Y-axis shows pressure in bar. Blue points represent theoretical equilibrium pressures at different mole fractions of CO_2. The orange dot represents an observed dissociation point, but not the mole fraction in experiment 8. Blue dashed line represents the second-order polynomial to the theoretical equilibrium values with a correlation of 0.9982. Grey dots represent experimental mole fraction of CO_2 at observed dissociation points in experiment 8.

4 – Results and discussion

At the Reservoir Physics Group in Bergen, there have been several studies of pure hydrate systems at the pore scale. This is the first study of mixed hydrate formation and dissociation of CH_4 - CO_2 mixtures in micro models. This chapter consists of obtained experimental results and challenges related to understanding the complexity of these systems. This chapter describes challenges and analyses the experimental results obtained both quantitatively and qualitatively. Challenges are included to help for future work. Presented results are chosen to supplement and expand the perception and understanding of hydrates in porous media. Section 4.1 summarizes single and multicomponent hydrate formation, while section 4.2 presents hydrate behaviour when injecting CO_2 into a porous media containing methane hydrate. Section 4.3 focuses on dissociation mechanisms and how molar composition changes in a mixed hydrate.

4.1 Hydrate formation

Table 4-1 list the twelve mixed hydrate formation experiments conducted in this work. Experiments 1, 2, 4, and 5 were carried out to study formation mechanisms for a gas hydrate system of CO_2 and CH_4, whereas experiment 3 consisted of pure liquid CO_2. Experiments 6-12 were carried out to make repetitive conditions for each formation. Section 4.1.2 explains some of the challenges to recreate repetitive fluid distributions in the micromodel. Eleven out of twelve formations were induced by agitation (flow of fluids), whereas hydrate formation in experiment 1 was achieved by decreasing temperature into the GHSZ at constant pressure. Saturation values are based on fluid distribution before formation initiated. Hydrate saturation values are based on hydrate distribution after formation. In experiment two, hydrate formed during fluid agitation, which made it impossible to calculate saturation values. Further analysis showed a mixed hydrate formed with an overlying free gas layer. Each image except experiment two was segmented in Paint.net, calculation and procedure can be found in section 3.4.

Table 4-1 – List of experiments

		$\boldsymbol{Saturations\ before\ formation}$				
$\boldsymbol{Exp.}$	$\boldsymbol{Formation\ pressure}$ $[\boldsymbol{bar}]$ $\pm\mathbf{1.4}$	$\boldsymbol{S_{CH_4}}$ $[\boldsymbol{fraction}]$	$\boldsymbol{S_{CO_2}(liq)}$ $[\boldsymbol{fraction}]$	$\boldsymbol{S_{water}}$ $[\boldsymbol{fraction}]$	$\boldsymbol{Temperature}$ $[^0\boldsymbol{C}]$ $\pm\mathbf{0.2}$	$\boldsymbol{S_{hydrate}}$ $[\boldsymbol{fraction}]$
1*	65,00	X	X	X	10,60	0,92
2	48,00	X	X	X	3,30	0,94
3	70,00	0	0,38	0,62	3,50	0,44
4	45,00	0,55	0,01	0,44	2,20	0,96
5	44,00	0,88	0,00	0,12	2,20	0,94
6	65,00	0,05	0,30	0,65	1,70	0,96
7	65,00	0,34	0,00	0,66	3,10	0,95
8*	65,00	X	X	X	3,60	X
9	65,00	0,000	0,84	0,16	3,50	0,96
10	64,00	0,61	0,01	0,38	3,50	0,94
11	65,00	0,04	0,01	0,95	3,50	1,00
12	65,00	0,89	0,000	0,11	3,50	0,92

* Data for experiment 1 and 8 were lost during data acquisition.

4.1.1 Single component hydrate formation

Pure hydrate

Previous micromodel research done by the Reservoir Physics group at the University of Bergen reports that hydrate formation shows either a porous hydrate film and or nonporous crystalline hydrate morphology. The research has involved distilled-, saline water and methane gas. Pure CO_2 hydrate forms a similar hydrate film morphology as pure methane hydrate. However, further CO_2

hydrate growth forms a solid crystalline morphology, which is easy to distinguish from water, compared to transparent crystalline methane hydrate. Figure 4-1 shows known methane hydrate configurations acquired in previous work. In general, the symbols W, G, L, R, HF and H will denote water, CH_4 gas, liquid CO_2, rock, hydrate film and crystalline hydrate respectively.

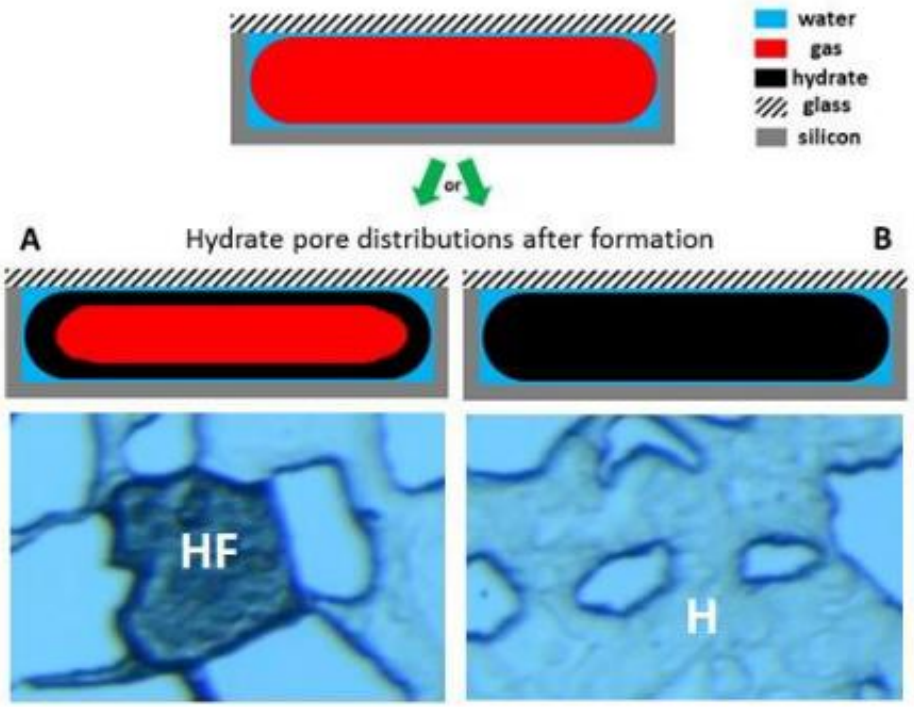

Figure 4-1 – Top: shows a methane hydrate pore occupancy (Almenningen, Iden, *et al.*, 2018)*. Below: real view images of hydrate configurations observed in the work of Lysyy* (Lysyy, 2018)*.*

Figure 4-2 shows the formation sequence of pure CO_2 hydrate at 70 bar and 3.3 °C. Hydrate film encapsulating liquid CO_2 was observed to develop a coarse hydrate film morphology. Different refractive indexes cause the difference in morphology. Methane gas is transparent with a refractive index, n = 1, while liquid CO_2 is a rich grey coloured component with a refractive index as a function of its density at 25 °C in the range of 1.20 - 1.25 (Guo *et al.*, 2006).

Image A shows fluid distribution right before formation initiated. Pore space was initially filled with liquid CO_2 and water. In image B, after 10 sec, the hydrate film encapsulates the liquid CO_2. Growth initiated at the liquid-water interface in the continuous liquid CO_2 phase along the pore walls and propagated towards pore center. In Image C and D, hydrate film growth proceeded through the water denoted by the yellow circles. Image E illustrates the hydrate films growing into a coarse morphology. In image F, yellow circles denote the same areas as in image C and D. At this point hydrate growth in the water has formed discontinuous isolated CO_2 hydrate.

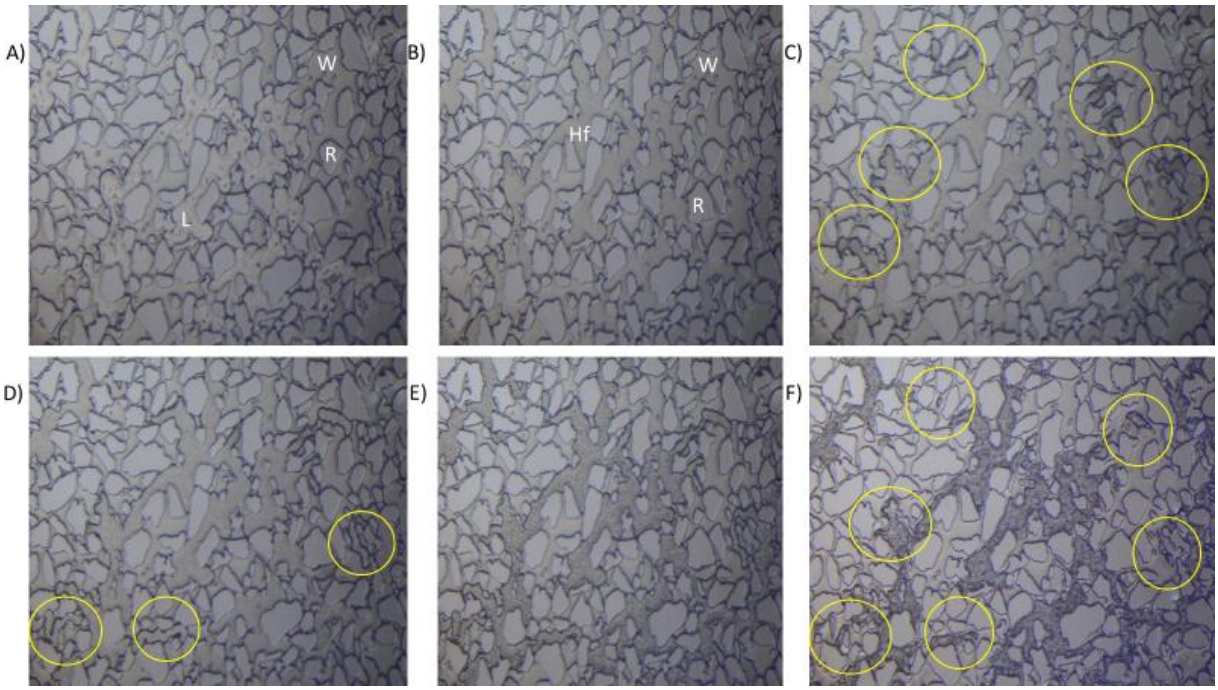

Figure 4-2 - Image sequence of liquid CO_2 hydrate formation at 70 bar and 3.3 ^oC. A) Initial saturation, t – 0 seconds. B) Hydrate film encapsulating liquid CO_2, t – 10 seconds C) Hydrate growing through water phase, t- 30 seconds. D) Further growth through water phase, t – 2 minutes. E) Hydrate film developing a coarse morphology, t – 25 minutes. F) Stable system after 18 hours.

An important observation is that after initial liquid CO_2 hydrate formation, the further formation could propagate through the water and increase hydrate saturation. This is caused by the high solubility of CO_2 in water. CO_2 hydrate formation will cause a pressure reduction in the pores, and the dissolved liquid CO_2 in water will partition from the water and induce further hydrate growth through the water. This is an advantageous mechanism in the view of CO_2 storage in a cold aquifer. CO_2 storage in a cold aquifer can potentially make the solid hydrate act as a caprock in the reservoir. This geological trapping mechanism is beneficial to avoid the buoyancy effect of CO_2 in the gaseous state. The isolated CO_2 hydrates show that the integrity of the formed hydrate as a seal needs further research. Many parameters such as the equilibrium pressure to pure CO_2 hydrate, salinity and solubility prediction must be analysed to understand and use hydrates as caprock for CO_2 storage.

4.1.2 Multicomponent hydrate growth mechanisms

In a silicon micromodel, it is not possible to clarify if a mixed hydrate has formed. This section will describe and interpret the formation sequence for the different multicomponent systems with liquid CO_2 and CH_4 gas, obtained in this work.

Phase equilibrium of CO_2 is temperature and pressure dependent. The temperature in the CO_2 pump is assumed to hold room temperature (23 ^oC), meaning the liquid/gas boundary to CO_2 lies between 61 - 62 bar at 23 ^oC (CO2 calculator - A web computational tool, 2015). When CO_2 is supplied at pressures below 60 bar, it enters the model as a gas phase if the model holds a temperature of 23 ^oC. If CO_2 enters a colder temperature regime, it will condense to a liquid phase. There was no observation of condensation of gaseous CO_2 to a liquid state in the micromodel. The basis for further analysis is that CO_2 injected below 60 bar condensate to a liquid state before entering the pore network.

Mixed phase composition of liquid CO_2 and methane gas

The intention and hypothesis described in the previous paragraph were to investigate if pure CO_2 hydrate formed two configurations like methane hydrate. The sequence in Figure 4-2 showed no observation of two different configurations, although the system was given 18 hours from the formation to the start of stepwise pressure reduction. Liquid CO_2 and water saturation values in image A in Figure 4-2 were 0.387 and 0.632 respectively. Figure 4-3 illustrates a sequence where the pore space seems to consist of liquid CO_2 and water with the following saturation at 0.843 and 0.157 in image A respectively. Image B shows the composition encapsulated by hydrate film, where it darkens and thickens in image C. In image D, the transformation to a second configuration has started. The hydrate film starts to change colour at its interface and continues towards the pore center. Image E shows a second configuration where the hydrate film morphology has changed to a grey and crystalline configuration. There was no observation of CH_4 gas in the FOV during hydrate formation. The CH_4 gas is assumed to dissolve into the liquid CO_2 forming a one-phase system, with a low mole fraction of CH_4. This is quantified as a multicomponent hydrate since measuring the phase composition is limited by the apparatus.

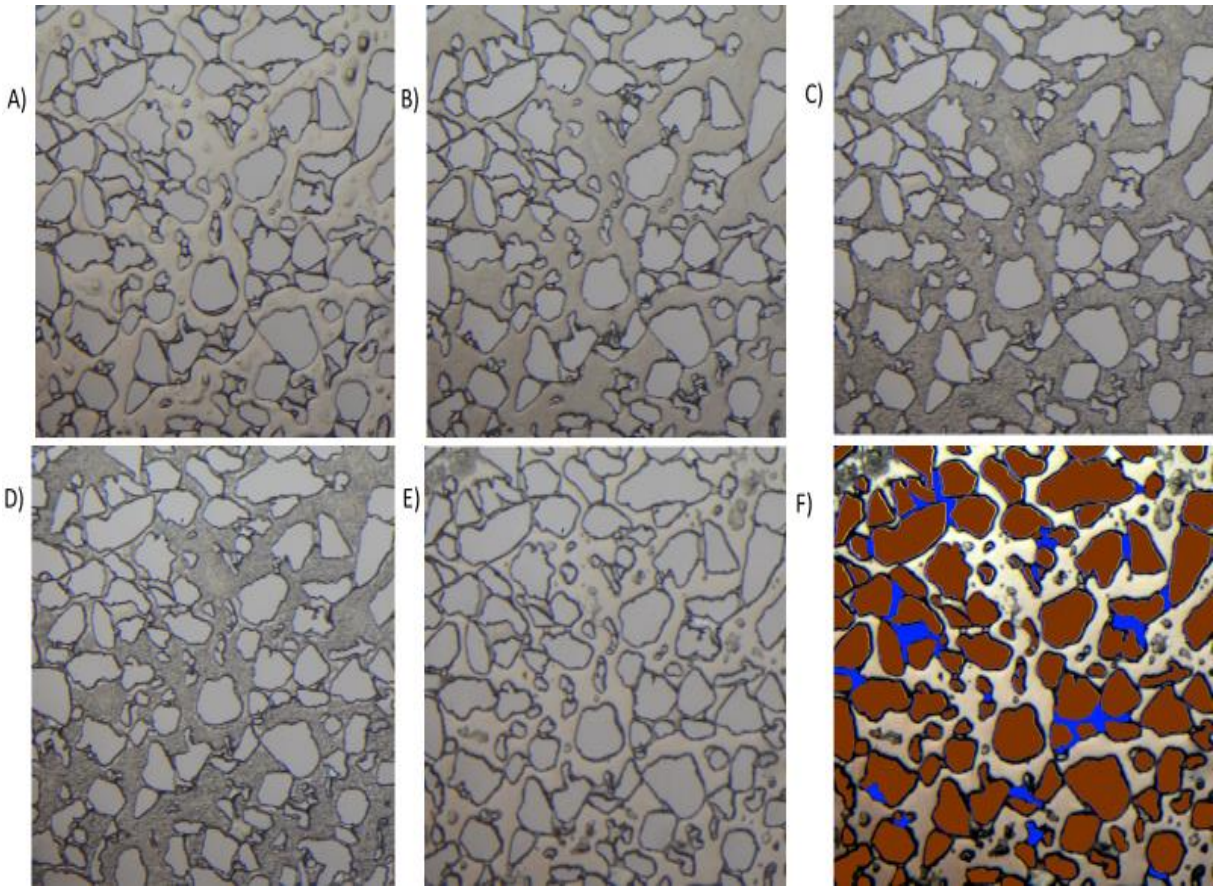

Figure 4-3 – Hydrate formation sequence of a mixed composition in experiment number 9 at 65 bar and 3.5 °C. A) Initial saturation before formation at 65 bar. B) Mixed phase encapsulated by hydrate film after 10 min. C) Hydrate film thickens after 35 min. D) Transformation about to start. Crystallization starting at the interface of hydrate after 90 min. E) Crystalline mixed hydrate after 12 hours. F) Segmented image of image E where grains are brown, water is blue, and hydrate remained unsegmented.

The described crystalline hydrate was a common observation when liquid CO_2 was present in this work. As described in the previous paragraph and shown in Figure 4-2, liquid CO_2 has almost the same colour as water [$n_{co_2} = 1.20 - 1.25, n_w = 1.33, n_{CH_4} = 1$]. This means liquid CO_2 and water is hard to distinguish, but they are easy to separate from CH_4 gas. One of the suggested mechanisms of CH_4 hydrate film conversion to crystalline CH_4 hydrate is water availability. Figure 4-2 describes a case where hydrate films enclosing liquid CO_2 did not grow into a crystalline morphology, even though free water was not a limiting parameter. In Figure 4-3, water was a limiting parameter, but hydrate transformed into a crystalline morphology. The FOV in image E) resembles a layer of liquid CO_2, but similar hydrate morphology was observed in other experiments. The controlling mechanism of mixed crystalline hydrate growth is not known, but the presence of CH_4 gas in the liquid phase might be the cause of the transformation to a mixed crystalline hydrate. With this setup, it is not possible to quantify the amount of dissolved methane in liquid CO_2. Based on the results of Nasir,

the maximum mole fraction of CH_4 in the liquid phase will be approximately 0.11 (Nasir *et al.,* 2015). To quantify if mixed hydrates formed, a stepwise dissociation was conducted.

Hydrate growth at the liquid CO_2 – water interface in a multicomponent system

Figure 4-4 illustrates a system with liquid CO_2, CH_4 gas and water saturation equal to 0.307, 0.038 and 0.655 respectively. The first sign of hydrate formation initiated at the liquid CO_2 – water interface but did not fully enclose liquid CO_2. Formation continued rapidly from the interface of liquid CO_2 through the water forming an irregular hydrate film pattern, as shown in Figure 4-4(C). Shindo (Shindo *et al.*, 1993) and Almenningen (Almenningen *et al.*, 2018b) observed a similar mechanism with seawater and distilled water respectively. Shindo suggests that the hydrate film at the liquid CO_2 – water interface will control the diffusion of CO_2 into the water. But, hydrate formation in water could be governed by a high amount of CO_2 initially dissolved in water. Or as proposed by Shindo, diffusion of liquid CO_2 into the hydrate-forming water from liquid CO_2 or a combination of both. Figure 4-4(A) shows the first sign of hydrate film thickening at the liquid CO_2-water interface. The time interval between film thickening at the interface of liquid CO_2 to hydrate film had formed through all water was less than 2 minutes. Large methane gas bubbles reduced in size, suggesting it was either consumed by water or dissolved into the CO_2 to participate in the hydrate growth of a mixed hydrate. Both continuous and isolated liquid CO_2 droplets transformed into a grey crystalline phase (marked with yellow circles in image D) making a definite change in morphology compared to the surrounding hydrate film. This configuration/morphology might be pure CO_2 hydrate or mixed hydrate.

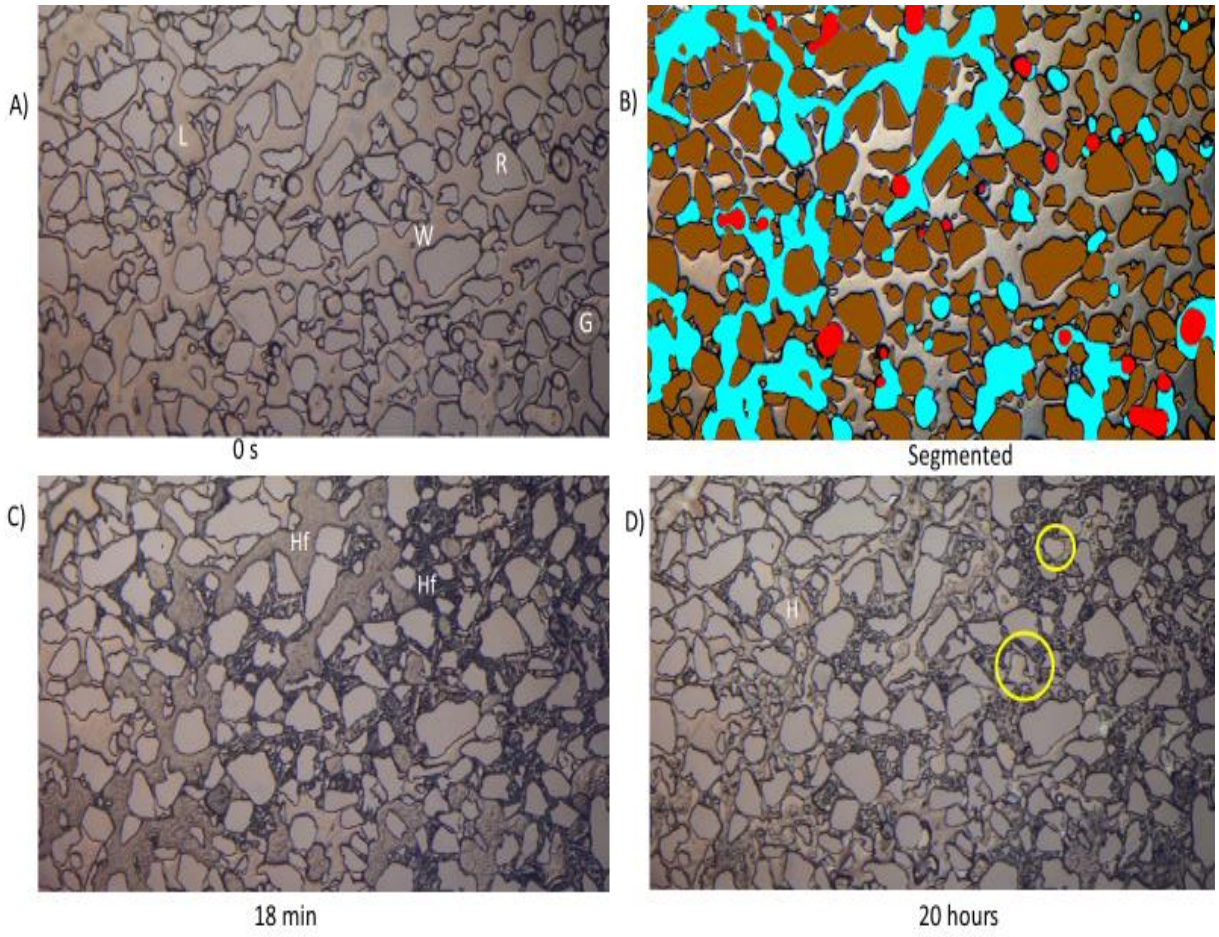

Figure 4-4 - Mixed hydrate formation sequence in experiment 6. A) Shows fluid distribution before formation initiated. FOV is saturated with liquid CO_2 (L), water (W) and isolated methane gas bubbles (G) on top of liquid CO_2. b) Segmented illustration to image A with liquid CO_2 (light blue), methane gas (red), grains (brown) and water not segmented). C) Two different hydrate film morphologies have developed. A dark film formed in water and lighter (grey) film morphology encapsulates liquid CO_2. D) Growth of liquid CO_2 hydrate from hydrate film to a crystalline hydrate. Yellow circles denote isolated CO_2 droplets which have transformed from hydrate film to a crystalline morphology.

As seen in Figure 4-4, isolated gas bubbles are segmented red in image (B) and flow on top of liquid CO_2. The microscopic view is a bird-eye view utilized to look vertically down into the model. A bird-eye view makes the setup disadvantageous to interpret formation mechanisms at the horizontal/parallel interface of liquid CO_2 and CH_4. This makes it impossible to obtain visual evidence if the components are encapsulated in two separate or one single film configuration. Modifying the setup horizontally could make favourable conditions for investigating formation mechanisms at the interface of liquid CO_2 and CH_4.

Hydrate growth in water pockets

Figure 4-5 illustrates a system with high gas saturation and presumably liquid CO_2 beneath. The growth pattern is similar to a single component system with CH_4. Hydrate film growth starts at the interface of the continuous gas phase and any water-wetting surface. Growth proceeds rapidly

through the continuous gas phase, in advance of slower growth towards pore center from the gas interface. Hydrate formation in a multicomponent system with an overlying gas phase can be described as a two-stage formation process. Once the overlying gas phase is encapsulated by hydrate film, growth proceeds and forms hydrate tortuous through isolated water pockets. Previous studies of single component hydrate growth in water reports that hydrate crystals grow close to already formed hydrate. Furthermore, the isolated gas bubbles act as a source for guest molecules for the growing crystals. The next figure illustrates the second stage growth after initial hydrate formation at 45 bar.

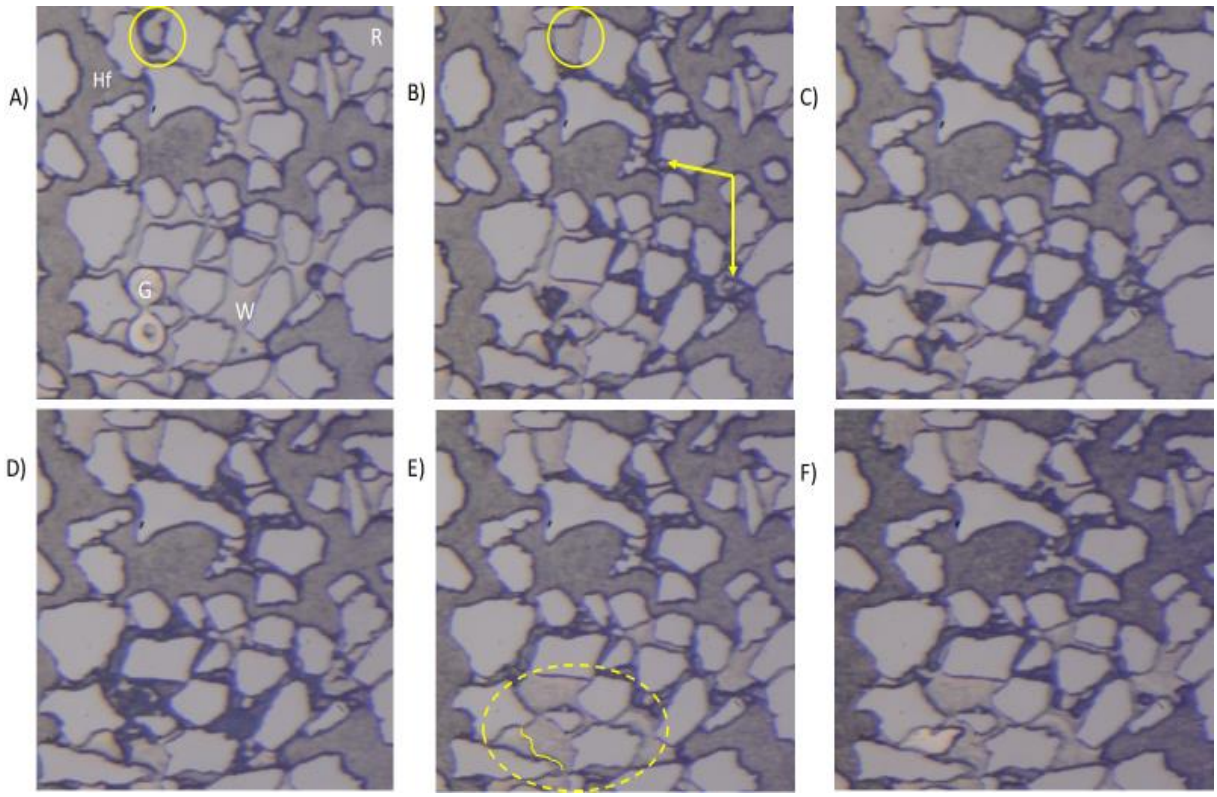

Figure 4-5 – Image sequence of further growth after initial formation in experiment 4. A multicomponent system with an overlying gas phase. A) Initial saturation with hydrate film encapsulated gas phase (HF), excess gas bubble (G), water (W) and grains (R). The yellow circle indicates a residual gas bubble about to crystallize, t – 0. B) Shows hydrate growth through water phase. Yellow arrows indicate the starting point of growth. Yellow circles indicate the same area as in Image 1 where hydrate has completely crystallized. The excess gas bubble in image A has been enclosed by hydrate film without contact with the hydrate front movement in the water and transforming to crystalline hydrate, t- 3 min. C) Shows further propagation, t – 4 min. D) Hydrate growth has consumed almost all free water available after initial hydrate formation. E) The dashed yellow circle shows that excess gas and "second stage hydrate growth" has crystallized. The yellow line inside dashed yellow circle marks the boundary between crystalline hydrate and water, t- 13 min. F) Shows saturation after 13 hours where gas either diffused from hydrate film, crystalline hydrate or partitioning out of water phase.

The second-stage formation was observed mainly in water pockets after encapsulation of a continuous gas phase. Growth in water is caused by a dissolved amount of CO_2 and CH_4 in water. A low amount of dissolved hydrate former in water can be a limiting parameter of further hydrate growth in water. However, a high amount will induce growth in water since hydrate formation causes a reduction in pore pressure and inverts the solubility in water. The solubility of CO_2 in water is about 10 times greater than CH_4 (Jung *et al.,* 2010). According to Henry's law, this will lead to a higher amount of CO_2 dissolved in water. Hydrate formation will lead to the partitioning of liquid CO_2 and gaseous CH_4 molecules as illustrated in Figure 4-6. The partitioned CO_2 will have a higher concentration and can use the available free water to grow and form new hydrate. Heat release during second-stage formation could create an exchange by liberating gas from surrounding hydrate as seen by the liberated gas in image F.

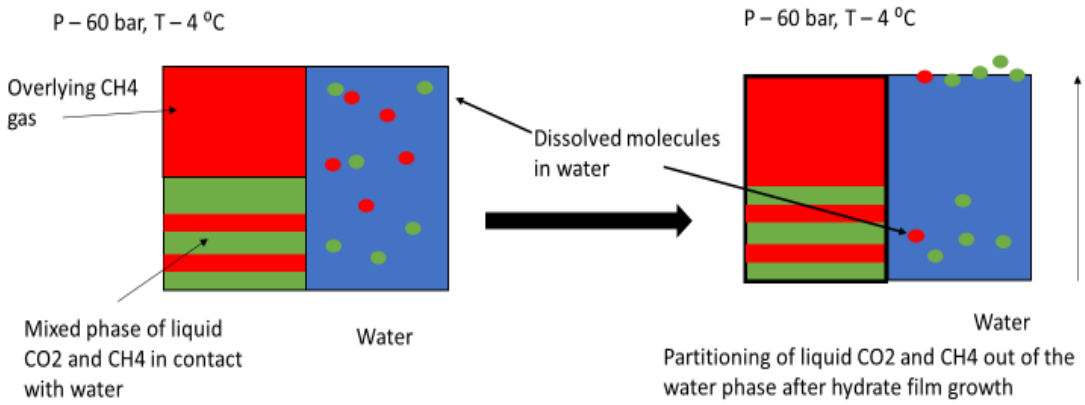

Figure 4-6 - Illustration of dissolution of methane, liquid CO_2 in water before formation to the left, and after formation to the right where the black arrow indicates partitioning direction.

Crystalline hydrate growth in water

Previous research has reported hydrate growth in water as rare. In this work, it was a common observation, and the previous paragraphs described the formation of hydrate film through the water. The figures presented in this chapter illustrate two types of hydrate growth in water. The components can be supplied to the hydrate-forming region either 1) through the water as dissolved liquid CO_2 or methane gas, 2) diffuse through hydrate films when hydrate films enclose liquid CO_2 and gaseous CH_4.

Growth in water was observed in contact with liquid CO_2 or hydrate film. Figure 4-7 demonstrates crystalline hydrate formation in water that transforms into a crystalline hydrate. Hydrate formation initiated in isolated droplets (liquid CO_2) and bubbles (CH_4 gas), and hydrate crystals formed in water across the pores. Similar hydrate crystal growth in water was reported and explained by Tohidi

(Tohidi *et al.*, 2001). Image (A), shows initial saturation before formation. Pores are filled with water, liquid CO_2 droplets and methane bubbles. Image B is a segmented image of image A. In image C, the formation of hydrate crystals propagates rapidly in water between the isolated phases (droplets and bubbles) before hydrate films starts to enclose the isolated phases. In image D, a partitioning phenomenon takes place one minute after initial formation. Liquid CO_2 appears to partition in water and hydrate film encloses the partitioned phases instantaneously. Image D and E are magnified to illustrate this phenomenon which happened across the entire FOV in a few seconds. During the partitioning process, it seems liquid CO_2 is liberated from the water and enclosed by hydrate film, indicated by the yellow circles in image (D). Darker hydrate film could be an indication of dissolved CH_4 gas in liquid CO_2. Miscibility of liquid CO_2 and CH_4 gas could lead to liquid CO_2 as a dissolving promotor for CH_4 gas in water. The high availability of water led to complete crystallization of hydrates across the pores.

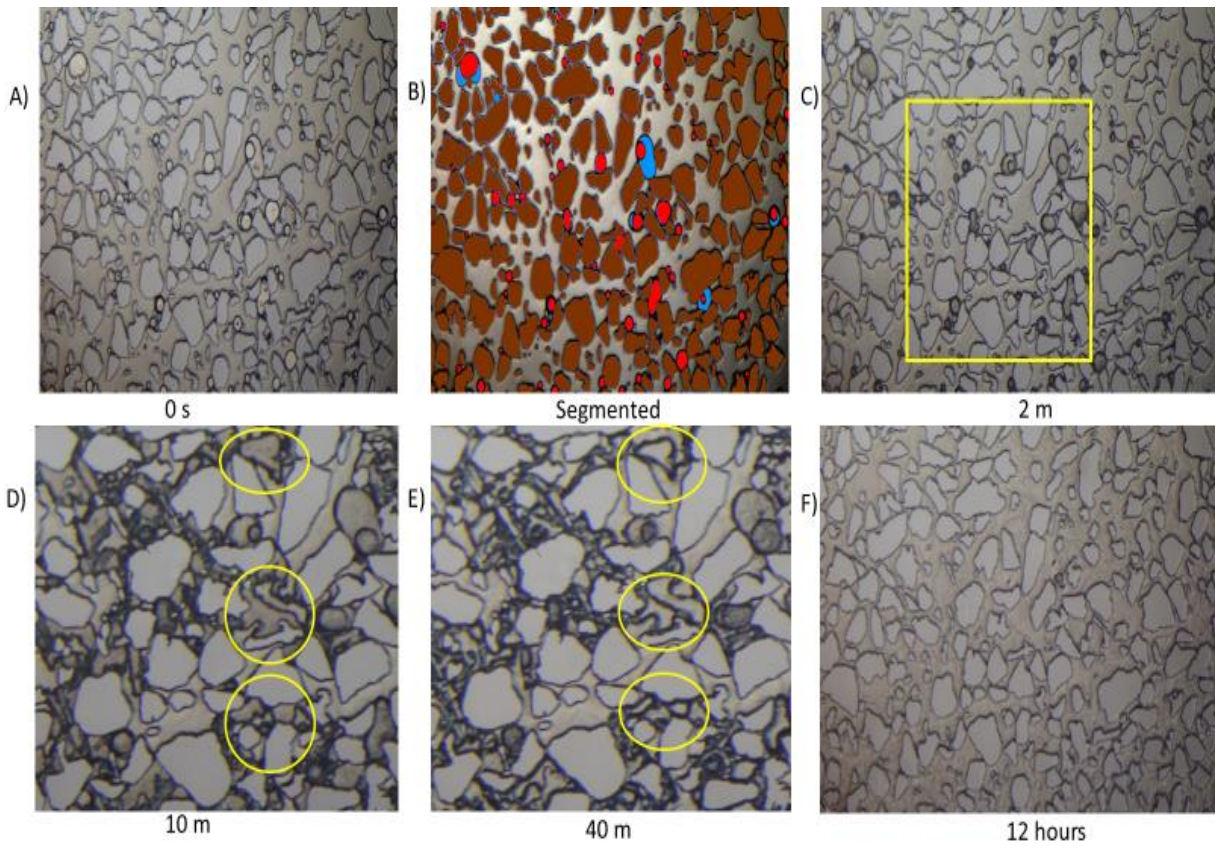

Figure 4-7 - Formation sequence in experiment 11. Image A) shows fluid distribution before formation. Image B) Segmented image of image A where showing grains (brown), methane gas (red), liquid CO_2 (light blue), water remained unsegmented. Image C) shows initial formation where droplets and bubbles are being encapsulated by hydrate film. Hydrate crystals have grown in water (difficult to see in the image). The yellow square indicates FOV in image D and E. Image D) Hydrate film have formed in water and reveals dissolved phases which appears to liquid CO_2. Yellow circles indicate areas of where liquid CO_2 appears from water phase encapsulated by hydrate film. Image E) Shows crystallization of hydrate film around liquid CO_2 starting from center of the phase. E) The whole FOV has completely crystallized after 12 hours.

The partitioning process might be connected to the inverted solubility of CO_2 and CH_4 in water due to hydrate formation. If the concentration of CO_2 exceeds the solubility limit in water, the aqueous solution will be supersaturated. Excessive CO_2 will partition from the aqueous solution and form new hydrate cells at the hydrate surface (hydrate crystals formed in water (image C)). Supersaturated water can cause the dissolved liquid CO_2 and CH_4 to instantaneous partition out of the water. The tendril and cross-hatched skeletal growth in water are typical for crystallization processes under supersaturated conditions. That is, the system is kinetically driven, and the growth forms are not optimally configured for low surface energy (Tohidi *et al.*, 2001).

Additional observations - exchange

Between hydrate formation and dissociation procedures, the system was left until the next day to ensure the system was in equilibrium. The saturation in the FOV could change between formation and dissociation. A change in saturation is an indication that the system was not in equilibrium. Figure 4-8 shows a formation sequence with three different hydrate film structures in experiment 7. Image A shows hydrate film have encapsulated a continuous methane gas phase (Hf1) at 65 bar and 3.1 ^{o}C. Image B shows a fluid redistribution when water displaces the gas phase enclosed by hydrate film (Hf1). The yellow circle shows there is a boundary between the water pocket and the invading water. Additional water should mix with the residual water in the water pocket. A thin hydrate film might block the residual water in the water pocket and the invaded water to mix.

In image C, a hydrate film forms in the invaded water making three different hydrate film structures (Hf1, Hf2, Hf3) present at the same time. Hf1 represents the first hydrate film formed in image A and is segmented with blue in image D. Hf2 represents hydrate film growth in the invaded water and is segmented with green in image D. Hf3 represents the secondary formation of the redistributed gas and is unsegmented in image D.

Hf1 and Hf2 starts to crystallize 25 minutes after the first formation (Hf1). After 75 minutes Hf1(blue) have partially crystallized, and Hf2(green) has completely crystallized. Image F is taken 14 hours after image E in front of the dissociation process. At this point, hydrates might have dissociated, and liberated gas has accumulated in the same pores where Hf1 and Hf2 formed. Hf3 has partially melted from center of pores where hydrate film is assumed to be thinnest. The pressure was kept constant at 65 bar overnight, which suggests the system was in a continuously formation-dissociation process.

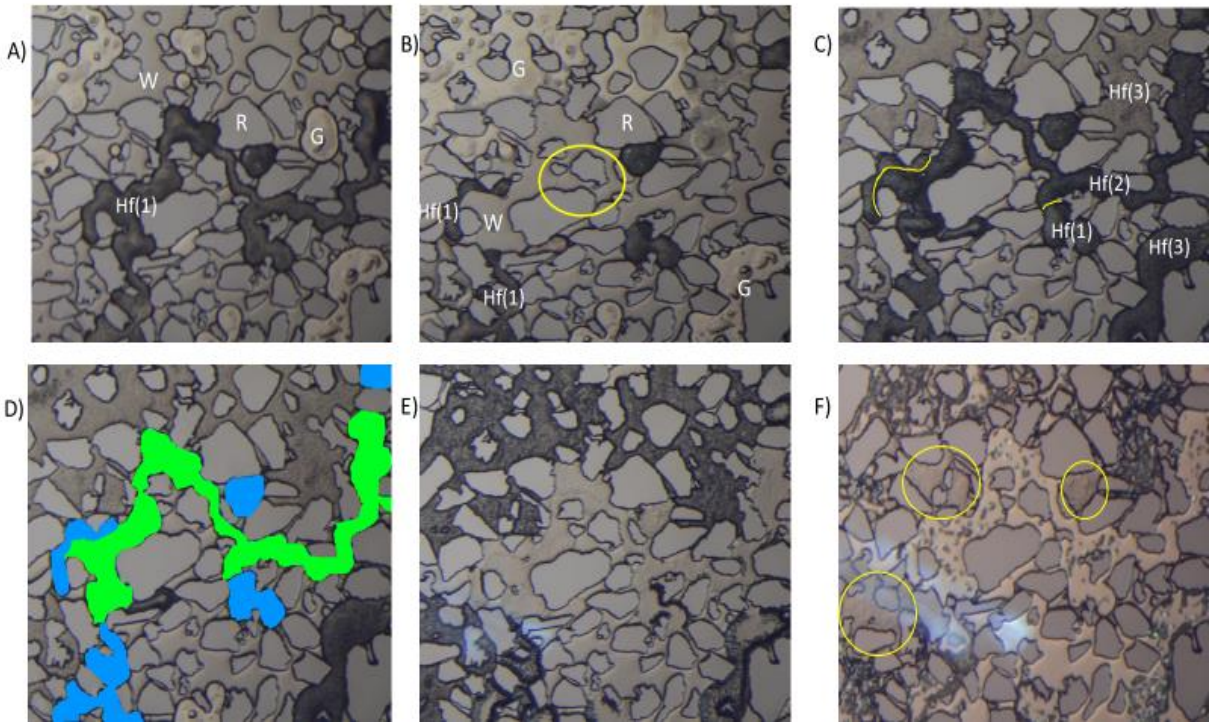

Figure 4-8 - Formation sequence of a mixed hydrate in experiment 7. Three different hydrate film structures, grains, gas and water, are denoted as Hf(1-3), R, G and W respectively. Image A) Formation of a continuous gas phase represented by Hf(1), t – 0 m. Image B) Fluid redistribution, t – 10 sec, after the first hydrate film formation. Water invades hydrate film capillary Hf(1) and reduces gas saturation and creates isolated areas with hydrate film. Image C) Hydrate film structure 2 (Hf2) forms in water indicates the presence of dissolved liquid CO_2 and Hf3 encapsulates another continues gas phase. Yellow lines show boundaries between Hf1 and Hf2. Image D is segmented Image C, where blue represents Hf1, green represent Hf2. Hf3, water, grains, gas remained unsegmented. Image E) Hf1 and Hf2 have almost completely crystallized and Hf3 have acquired a darker film morphology. Image E) Hf1 and Hf2 have dissociated and Hf3 have dissociated partially. In the pores occupied by Hf1 and Hf2 inhibits methane gas which suggests liberation of methane because of exchange.

An increased gas saturation might be the case of CH_4 gas liberation from hydrate, suggesting an exchange took place, and the formation of mixed hydrates. Similarly, the methane pump can cause increased gas saturation when the pump is in constant pressure mode. Hydrate formation will cause the pore pressure to decrease since gas is volumetrically compacted into a solid hydrate phase. The methane pump will respond by injecting more gas into the model to keep constant pressure. However, these mechanisms do not explain what seems to be melting of the surrounding hydrate film (Hf3). Besides, the pressure does not change significantly during hydrate formation, and it is assumed to be constant during formation. A continuously formation-dissociation process might indicate that exchange processes have taken place overnight. Hydrate film formed in water (Hf2) is an indication that dissolved liquid CO_2 participated in the hydrate formation. The formation of Hf2 could be the starting point of CO_2 - CH_4 exchange and partial dissociation of Hf1. The formation of Hf2 and Hf3 could release enough heat to dissociate each other or Hf1. Another exchange initiation

could be when hydrate film started to crystallize or a combination of these two. The crystallization process happened for 50 minutes. This suggests it could be a continuous heat release in the pore network leading to partial dissociation of the crystalline hydrate. CO_2 molecules could diffuse through hydrate films and form new hydrate with the liberated water and CH_4 to form a pure CO_2- or mixed hydrate.

4.2 Liquid CO_2 injection into a micromodel with methane hydrate

This section investigates CO_2 injection and CO_2 - CH_4 exchange in a porous media. There has been a lot of research conducted on replacement, but the research is primarily related to bulk studies and core scale, see section 2.3 for a summary.

An exchange process is compounded of multiple processes related to thermodynamics. This includes mass transport, heat liberation, mutual solubilities and pressure- and temperature-dependent phase conditions, among others. Therefore, a fundamental understanding of the CO_2 - CH_4 replacement is needed to develop this as a commercially viable method.

Table 4-2 summarizes all exchange experiments. They are numbered from 13-20 in continuation from Table 4-1 since they are combined in Table 4-3 in section 4.3. After methane hydrate formation, the system was left at formation pressure, P_{system}, to ensure stable hydrate. The intention was to inject CO_2 at the same pressure, P_{start}, as the system. The pressure in the CO_2 valve fluctuates more than the CH_4 pump pressure making it difficult to inject at equal pressure value measured by the methane pump. The pressure fluctuation could generate a small differential pressure at the start of the injection in some experiments. The final pressure, P_{final}, indicates the pressure at the end of the injection. Time indicates total injection time and temperature were set in the range of 3.7 to 4.5 °C.

Table 4-2 – List of CO_2 injection experiments

Exp	$\boldsymbol{P_{system}}$ $[bar]$ ± 1.4	$\boldsymbol{P_{start}}$ $[bar]$ ± 1.4	$\boldsymbol{P_{final}}$ $[bar]$ ± 1.4	$\boldsymbol{Q_{rate}}$ $[ml/hr]$	***Time*** $[Minutes]$	$\boldsymbol{T_{sys}}$ $[^0C]$ ± 0.2
13	58,0	58,7	X	X	X	4,5
14	58,7	58,7	65,0	0,5	1314	4,0
15	68,5	69,3	100,0	0,5	150	4,0
16	68,0	68,4	72,4	0,5	28	4,0
17	69,0	69,8	71,9	0,2	115	4,5
18	62,0	62,0	66,8	0,2	90	4,0
19	65,5	65,5	66,8	0,5	21	4,0
20	65,0	65,0	68,7	1,0	28	3,7

4.2.1 Liquid CO_2 injection into methane hydrate reservoir

One of the main objectives in this work was to get liquid CO_2 in contact with methane hydrate. This section reports the observations of liquid CO_2 in contact with methane hydrate and water.

Liquid CO_2 in contact with water

Figure 4-9 shows a pore space filled with methane hydrate. Liquid CO_2 injection led to reduced methane hydrate saturation because water displaced the methane gas enclosed by hydrate films. Consequently, liquid CO_2 was not observed to displace methane gas enclosed by hydrate films and had to displace the water to invade the pore network, as illustrated in image (C). CO_2 hydrate formation initiated immediately after flow of liquid CO_2 ceased. A thick dark film developed at the interface between CO_2 and wetting surfaces and propagated towards pore center. The hydrate film morphology was thicker in the pore corners because the water film is thicker in the pore corners, as illustrated in Figure 4-10 (Hauge *et al.*, 2016).

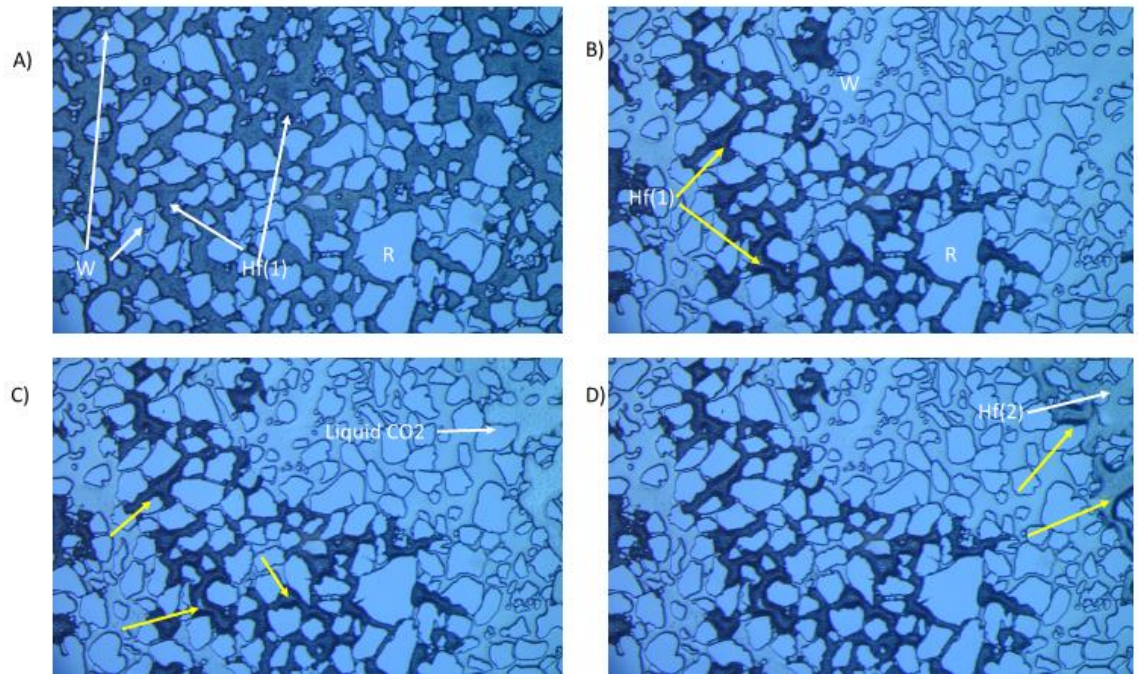

Figure 4-9 - Liquid CO_2 flows into the FOV in experiment 18. A) Initial methane hydrate saturation where methane hydrate, water and rock are denoted Hf(1), W and R respectively. B) Water displaces gas enclosed by hydrate film and reduces hydrate saturation after 12 min. Yellow arrows indicate places where hydrate film forms a darker morphology at the hydrate film – grains interface because of water supply through wetting films. C) Liquid CO_2 enters pore space in the top right corner after 16 minutes indicated by the white arrow. D) Hydrate film encapsulates liquid CO_2, Hf(2), where film morphology develops a thicker film at the film – grain interface after 16 min indicated by yellow arrows. Same reasoning as film thickness development for hydrate film in image (B and C), which is because of water accumulation in the pore corners.

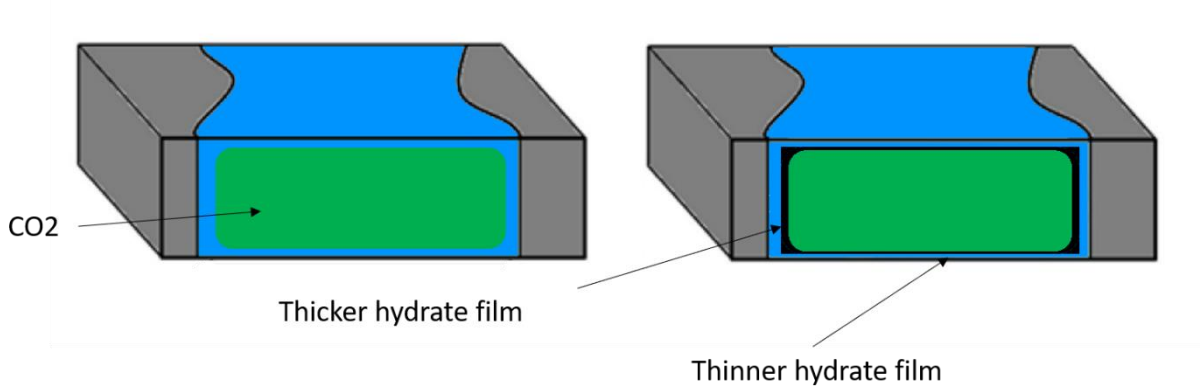

Figure 4-10 – Illustration of hydrate film enclosing liquid CO_2. Left image illustrates liquid CO_2 drop in contact with water. The right image illustrates a droplet of liquid CO_2 enclosed by hydrate film. The hydrate film is thin on the horizontal axis and thicker on the vertical axis because of water availability in the pore corners. The illustration is modified from Hauge *(Hauge* et al*., 2016).*

Water invasion

The cause of water invasion is most likely related to flushing of the micromodel ahead of each experiment. Flushing will cause water to enter all tubing and make a water bank between the CO_2 valve and the model. Starting an injection with a small differential pressure cause a force on the water in the tubing leading to a waterfront invading the pores in front of the liquid CO_2. Methane gas enclosed by hydrate films forms cylindrical capillaries through the model. A waterfront will displace methane gas enclosed by hydrate films, reducing hydrate saturation and form an excess water system (class 2 reservoir). This system is both favourable by increased surface contact area to methane hydrate, and at the same time unfavourable since the solubility of liquid CO_2 in water can initiate massive growth of CO_2 hydrate and reduce the permeability in the reservoir. Varied injection rates can cause the liquid CO_2 to occlude regions and prevent direct contact with CH_4 hydrate, and hinder replacement (Jung *et al.,* 2010). Ersland (Ersland *et al.*, 2010) observed that diffusion was the apparent dominant transport mechanism for CO_2 to contact methane hydrate. In a system where CO_2 is not in contact with methane hydrate, CO_2 must dissolve in the water and diffuse to the methane hydrate. An exchange can take place by forming a CO_2 hydrate with water at the surface of methane hydrate film. The heat will dissociate large cavities allowing CH_4 to escape and diffuse through wetting films. An open cage structure will draw CO_2 molecules into the large cavities in the structure.

Liquid CO_2 hydrate film collapse

A hydrate film formed at the continuous liquid CO_2 - water interface. Figure 4-11 shows magnified images of hydrate film thickening in the liquid CO_2. Image (A and B) are same as image (C and D) in Figure 4-9, only magnified. Image B and C shows one and two breakpoints in the hydrate film enclosing liquid CO_2. Breakpoints are denoted by the white circles in image (B) and (C). Furthermore, the hydrate film forms a more scattered morphology. This morphology is dominant in the centre of the pores forming a thicker hydrate film towards the pore walls and in the pore throats. Hydrate film thickening in the pore throats are illustrated by the yellow circles in image D. In image (E), crystalline hydrate might have grown in water in the area with scattered hydrate film. The red circles indicate similar hydrate growth in water as described in Figure 4-5. Image (F) shows crystalline hydrate development in the pore space after 11 hours. Ultimately, the hydrate has grown and merged together to one crystalline morphology where the dark spots might indicate a higher concentration of liquid CO_2.

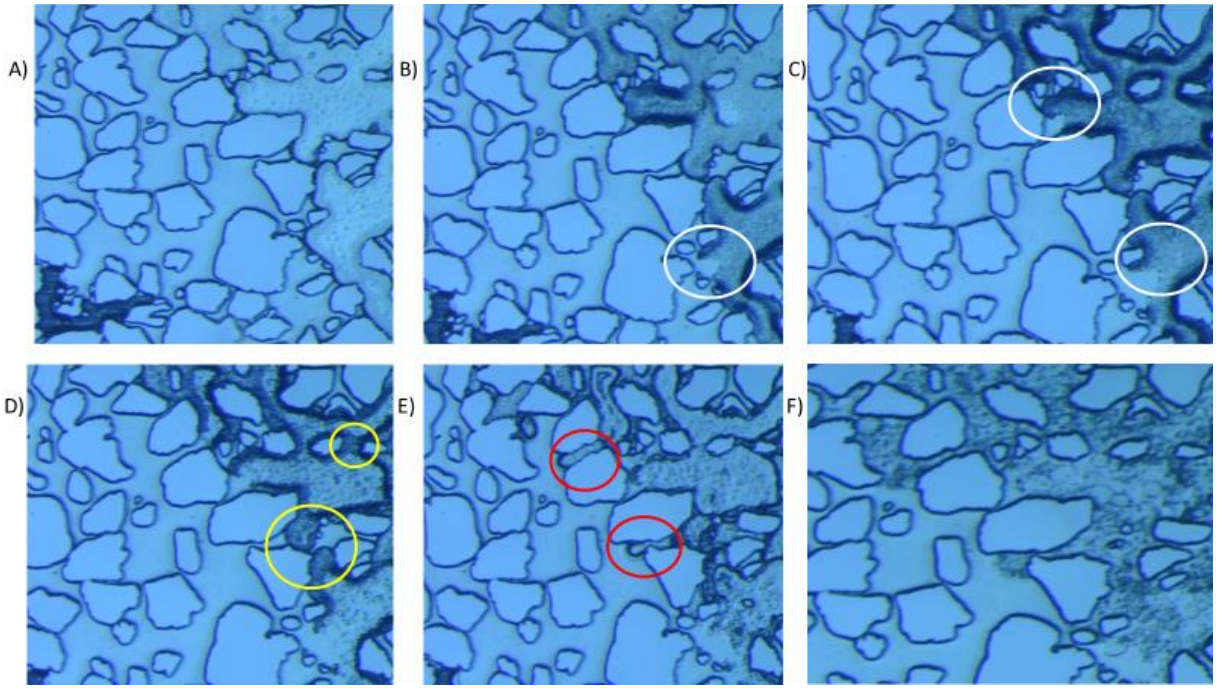

Figure 4-11 - Image sequence showing a collapsing liquid CO_2 hydrate film interface. White circles denote breakpoints. A) Liquid CO_2 displaces water and flows into the FOV, t – 0 m. B) First breakpoint where the interface of hydrate film enclosing liquid CO_2 collapses, t – 8 sec. C) Second breakpoint, t- 12 sec. D)Hydrate film thickening where the yellow circles might indicate higher concentration of liquid CO_2 , t – 1 min. E) Hydrate growth, t- 13 min. F) Crystalline hydrate morphology, t – 11 hrs.

The breakpoints in the hydrate films might suggest that the concentration of CO_2 in water is low, resulting in a concentration gradient causing liquid CO_2 to dissolve in water. The dissolution process might leave residual liquid CO_2 trapped by capillary forces, illustrated by hydrate film thickening in

image (E). The dissolving process appears to start in the center of the pores and spread towards pore walls. This could be the same reasoning as to why hydrate films tend to dissociate from the pore center towards pore walls. Hydrate film is thickest at the pore walls and have a dispersed pattern in the pore center. The boundaries seem to show an interface between water and liquid CO_2 enclosed by hydrate film.

Liquid CO_2 in contact with methane hydrate

In this work, liquid CO_2 was only observed in contact with hydrate films encapsulating CH_4 gas. The sequence is presented in two figures where, Figure 4-12 proofs that the micromodel is suitable to investigate $CO_2 - CH_4$ replacement, and Figure 4-14 shows the formation of CO_2 hydrate in proximity to methane hydrate.

Figure 4-12 demonstrates the only observation of liquid CO_2 flowing through a narrow pore channel in contact with methane gas enclosed by hydrate film. Image (A) shows a pore space filled with hydrate film, grains and small water pockets. Image (B) shows reduced hydrate saturation because of water invasion. Image (C) shows liquid CO_2 flowing through the pore channel, where the white arrows indicate flow direction. Image (D) shows hydrate film encapsulating the liquid CO_2.

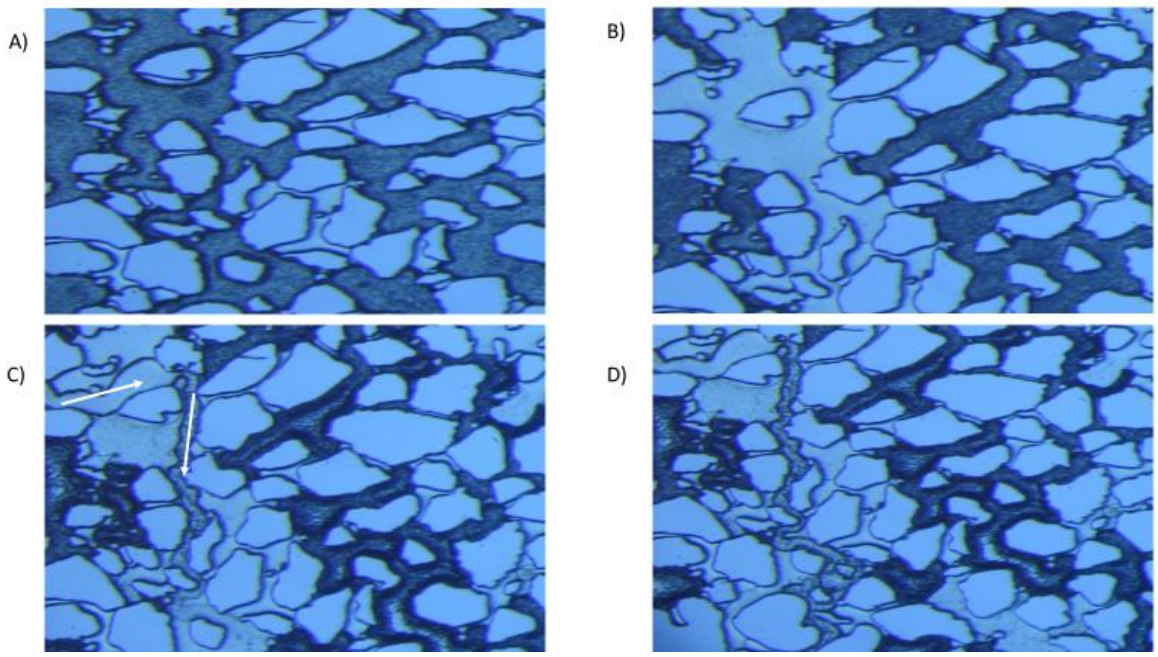

Figure 4-12 – Proof that liquid CO_2 can propagate through the porous medium in experiment 18. A) Initial methane hydrate saturation. Image is captured at the same time as Figure 4-9 (A). B) Water displaces gas and reduces hydrate saturation after 50 sec. C) CO_2 displaces water and propagates through the medium after 26 min. White arrows indicate flow direction D) Hydrate film formation enclosing liquid CO_2 initiates quickly after flow has terminated.

The narrow channel with liquid CO_2 is evidence of a poor microscopic sweep through the pore network. Liquid CO_2 is a volatile and low viscous (mobile) substance that finds pathways with good pore-connectivity. Because of its low viscosity, it tends to follow the same path resulting in viscous fingering and bad microscopic sweep. Lenormand showed numerically that pore scale capillary and viscous forces cause a higher tendency to viscous fingering close to injection ports because of high flow velocities (Lenormand *et al.*, 1988). The edges of the micromodel are high permeable channels with no artificial sediment, illustrated in Figure 4-13. These channels have low fluid flow resistance, which gives CO_2 free flow path to the production port. The high permeable channels reduce the microscopic sweep and increase the risk of clogging with accumulated water in the production port.

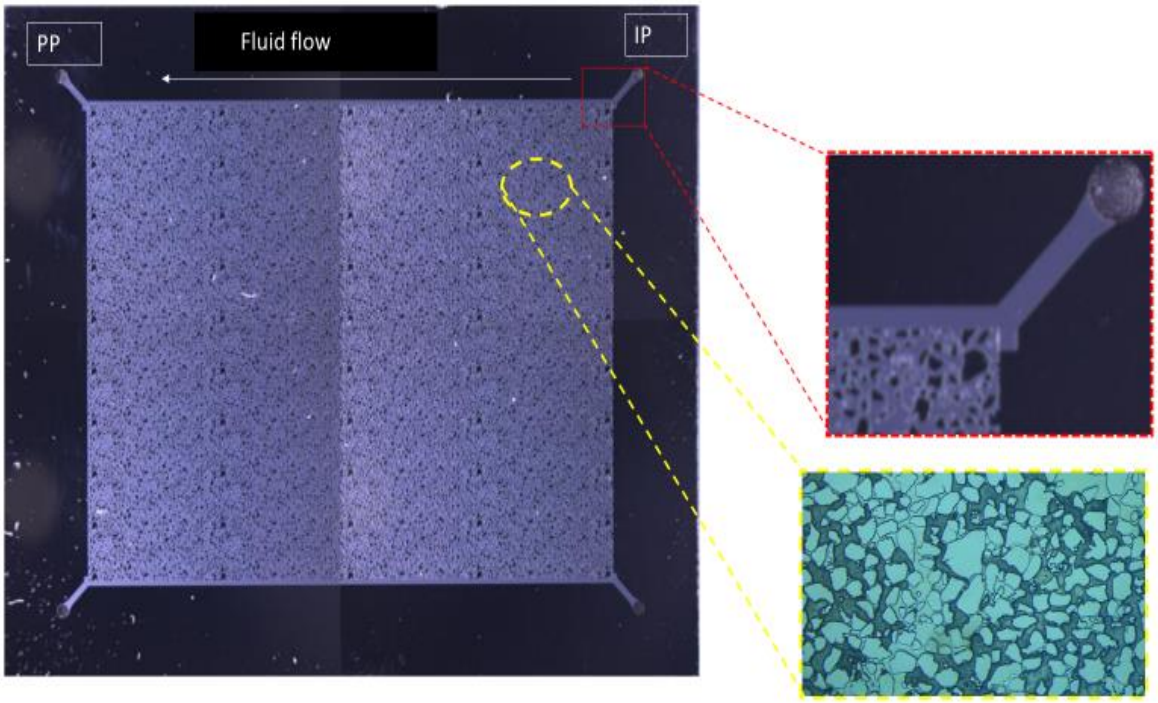

Figure 4-13 - Illustration of the micromodel, illustrating the injection port (IP, red stapled lines), fluid flow direction (white arrow), the field of view (yellow stapled lines). The figure is modified from Benali (Benali, 2019).

Hydrate growth after liquid CO_2 injection

Figure 4-14 describes the continuation after liquid CO_2 flowed through the pore channel and illustrates the hydrate growth phenomenon in the presence of methane hydrate. The hydrate growth starts with hydrate film encapsulating liquid CO_2 in image (A). In image (B) similar hydrate growth occurs in available water pockets with free water, as observed in Figure 4-2 and Figure 4-5. Hydrate growth in the water pockets increases hydrate saturation and allows direct contact between CO_2 hydrate and CH_4 hydrate on left and right hand-side of the pore channel. In image (B and C), hydrate film enclosing methane gas starts to transform into crystalline hydrate from the center of the pores,

indicated by the yellow circles. In image (D), liquid CO_2 hydrate grow and merges together with crystalline methane hydrate, indicated by the yellow circle. In image (E), the hydrate film enclosing methane gas, except the area in the red circle, has completely transformed to crystalline hydrate. Image (F) shows the pore space is filled with crystalline hydrate 12 hours after the injection.

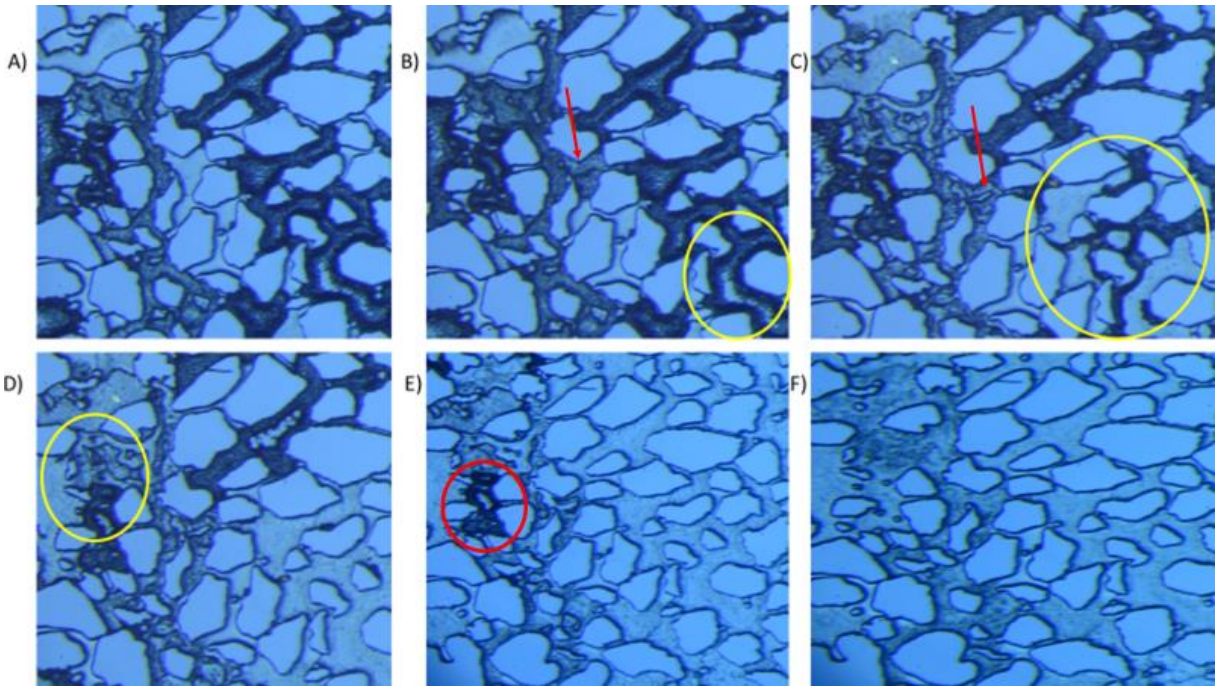

Figure 4-14 - Formation of liquid CO_2 hydrate in the proximity to methane hydrate. A) Shows formation of liquid CO_2 hydrate at t- 0 s. B) Liquid CO_2 hydrate film thickens and surrounding methane hydrate transforms to crystalline hydrate in the center of the pores indicated by the yellow circle, t – 4 min. C) The CO_2 hydrate starts to form a crystalline morphology and surrounding methane hydrate continues to transform to crystalline hydrate indicated by the yellow circle, t – 10 min. D) The yellow circle indicates that two crystalline hydrates merge together into one morphology after 18 min. E) Shows the FOV after 1 hour. F) Shows the pore space have entirely transformed to a crystalline morphology after 12 hours.

The pore channel liquid CO_2 flowed through is filled with crystalline hydrate. The morphology of this crystalline hydrate has similar morphology as in Figure 4-11. In this area, it is reasonable to believe that the concentration of CO_2 is higher compared to the surroundings. Furthermore, the surrounding methane hydrate film has grown into a crystalline morphology that resembles pure crystalline CH_4 hydrate. During this growth, it can be assumed that the exchange mechanisms described in Figure 1-6 and section 1.5.1 have taken place.

4.3 Hydrate dissociation by stepwise pressure reduction

Nineteen stepwise pressure reduction experiments were conducted to analyse how a mixed hydrate composition changes during a stepwise pressure reduction. Twelve dissociation experiments were complete after mixed hydrate formation and seven stepwise dissociation experiments were conducted after a CO_2 injection. Pressure reduction was made by retracting 10 ml/hr from the micro model system with connected lines until reaching one bar above theoretical pure CH_4 hydrate equilibrium pressure. If the equilibrium pressure to pure CH_4 was lower than the liquid/gas boundary to CO_2, the pressure was lowered to one bar above to see if there was any impact of CO_2 phase conversion. The pressure was reduced through CH_4 pump to avoid CO_2 to mix with water in the water pump due to its corrosive effect. Six dissociation experiments are considered as unsuccessful, due to hydrate clogging in the tubing.

In experiment one to five, the pressure was reduced every thirty minutes, and in experiments 6 to 19, it was reduced every hour if there were no changes in saturation in the FOV. A stepwise dissociation could take over 20 hours to complete. In that time span, dissociation could initiate in another part of the model and liberated gas could propagate into the FOV and induce further hydrate dissociation (Almenningen *et al.*, 2017). For future work, it should be considered to increase the time between each pressure step.

Table 4-3 shows an overview of the dissociation experiments. The overview is put together by mixed hydrate experiments (1-12) and CO_2 injection experiments (13-20). Equilibrium pressures are theoretical equilibrium values for pure CH_4- and CO_2 hydrate, calculated by CSMGem(Colorado School Of Mines, 2015). Dissociation points indicate pressure points of observed hydrate dissociation. “Reformation” indicates the pressure value where secondary hydrate formation occurred during dissociation. Reformation of hydrate above pure CH_4 equilibrium was observed in experiment 2 and 10. and will be discussed in detail in section 4.3.2.

Table 4-3 – Overview of hydrate dissociation experiments

Exp	Equilibrium pressure [bar] CH_4 [bar]	CO_2 [bar]	Dissociation points [bar]	Reformation [bar]	Temperature [ºC]
1	30,15	14,82	Plug	X	1,5
2	36,11	18,42	20, 19	37 and 20	3,3
3	x	18,40	18,17	18 and 17	3,3
4	32,34	16,11	31, 30, 28, 27, 25, 23, 22, 21	X	2,2
5	32,34	16,11	26	X	2,2
6	31,01	15,17	28, 27, 25, 22, 20, 15	16	1,7
7	35,39	17,91	34, 32, 31, 30, 29, 26	28	3,1
8	36,85	18,85	33, 32, 31, 30, 23, 22, 21, 20, 19, 18	24 and 22	3,5
9	36,85	18,85	Plug	x	3,7
10	36,85	18,85	36, 35, 34, 27.95, 27, 26, 25, 24, 23, 22, 20	29 and 26	3,5
11	36,11	18,42	20, 19, 18	X	3,3
12	36,11	18,42	Plug	X	3,5
13	36,11	18,42	Plug	34	3,3
14	36,11	18,42	39, 38, 37, 36, 35, 33, 31	X	3,3
15	36,11	18,42	38, 30, 29, 27.7, 27, 26, 25, 23, 21.9	38 and 25	3,3
16	40,77	21,38	30, 28, 26, 24, 23	28	4,5
17	40,77	21,38	29, 26, 25, 21, 18	21	4,5
18	38,77	20,01	Plug	23	4,0
19	37,98	19,59	33, 32, 31, 30, 28, 23, 22, 21, 20	X	3,8
20	38,77	20,01	Plug	X	4,0

4.3.1 Dissociation mechanisms

The pressure inside a hydrate cavity is equal to the equilibrium value to the hydrate gas composition. If the surrounding pressure is lower than the equilibrium value, the pressure gradient will generate a force causing the hydrate structure to dissociate (melt). The composition of a mixed hydrate can have a variety of fractions ranging from [0, 1] of one component and [0, 1] of the second component. Stepwise pressure reduction allows a mixed hydrate to dissociate at several pressure points between the upper and lower equilibrium pressures for pure hydrates depending on the mixed composition. Each dissociation point will reveal the liberated gas composition in the hydrate. Reducing the

pressure after CO_2 injection can lead to more production of methane and increasing the benefits of CO_2 injection.

Hydrate morphology varied due to the availability of water, the FOV was either dominated by hydrate film, crystalline hydrate or both combined. Crystalline hydrate dissociated over several pressure steps releasing more gas for each pressure steps. This suggests structures of a specific composition dissociates, while structures with a higher mole fraction of CO_2 are stable.

Hydrate film melting

Figure 4-15 demonstrates hydrate film melting during stepwise pressure reduction. It was observed that hydrate films encapsulating gas and liquid CO_2 became thinner after each pressure step. Hydrate film, crystalline hydrate, gas, water and grains are present in the micromodel and denoted as Hf, H, G, W and R respectively. Image (A) shows the pore space is filled with hydrate film, crystalline hydrate and grains. The system was inside the GHSZ before the pressure was reduced to 36 bar below pure CH_4 hydrate equilibrium pressure at 36.8 bar. In image (B) the pressure is reduced to 34 bar, and the colour of hydrate film turns lighter and has started to melt. The melting process started from the center of the pores and propagated to the pore walls. In image (C), red circles indicate the melting of hydrate film at 28 bar whereas yellow circles indicate dissociation of a crystalline hydrate. Even though almost all hydrate film has melted, the gas enclosed by hydrate films seems to be immobile because of thicker hydrate film at the pore walls holding it in place. Due note that gas can diffuse through hydrate films, but this was not observed. In image (D), hydrate film in the top right corner has completely melted and mobilized the gas phase. The red circle indicates an area with hydrate film still immobile. In image (E) at 24 bar, all hydrate film has melted, and the pore space is left with residual crystalline hydrate, water and gas. Hydrate film has dissociated and formed a continuous gas phase and liberated gas from crystalline hydrate propagates upwards from the bottom left of the image. In image(F) at 20 bar, all hydrate has completely dissociated, and gas is not restricted by permeability and has free flow. The dissociation in the top right induced further dissociation of the crystalline hydrate between the two areas in focus before connecting as a continuous gas phase.

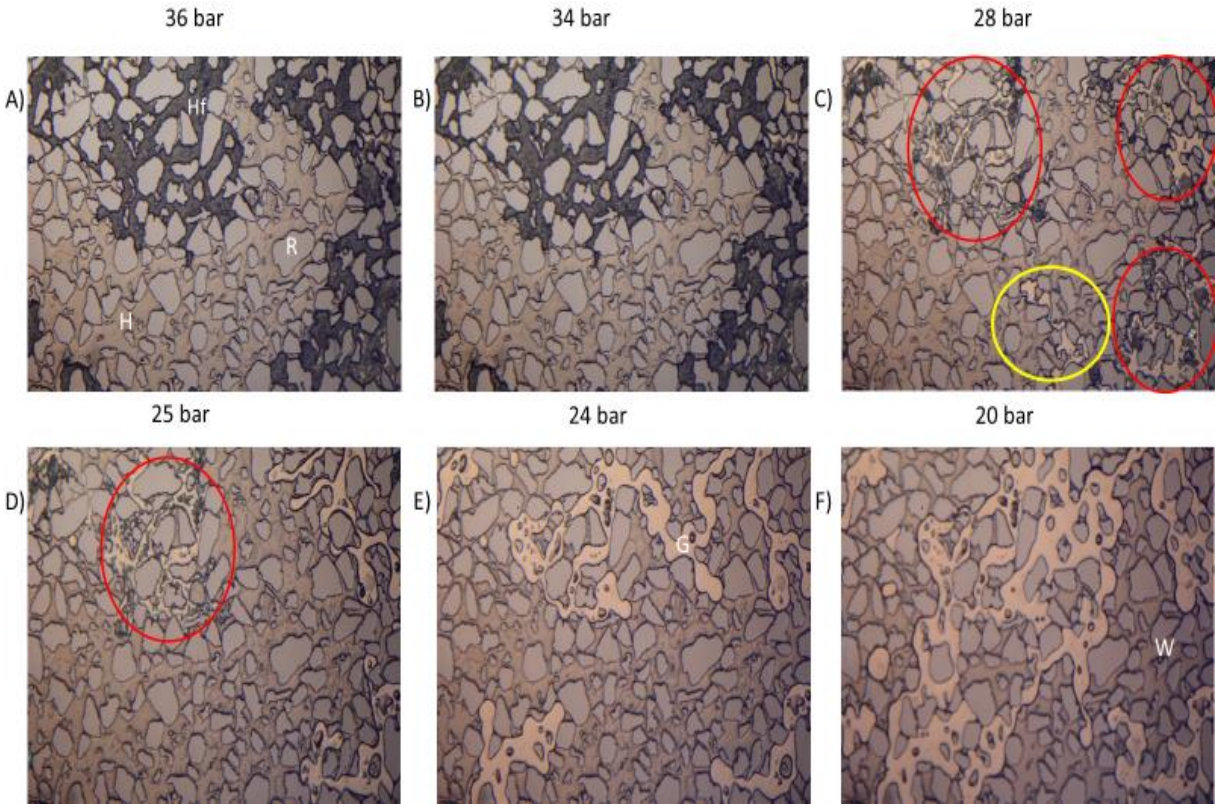

Figure 4-15 – Image sequence showing that hydrate film melts during many pressure steps in experiment 10. A) Initial saturation where pore space is filled with crystalline hydrate (H), hydrate film (Hf) and grains (R). B) Hydrate film is stable at 34 bar. C) The red circles indicate areas where hydrate films start to dissociate. The yellow circle indicate that crystalline hydrate has dissociated at 28 bar. D) Two areas with hydrate film have completely melted, whereas the gas in the red circle is still immobile at 25 bar. E) All hydrate film zones have dissociated and crystalline hydrate remains stable at 24 bar. F) Residual hydrate has dissociated at 20 bar.

Each pressure step was allowed sufficient time to where no phase transitions or flow was observed. Throughout the stepwise dissociation, residual hydrate films remained in the center of the pores, as seen in image (A-D), and melted closer towards pore walls. Residual hydrate film in the center of pores contradicts the water-wet nature of the micromodel. Hydrate films are presumably thickest in the pore corners and thinnest in the pore center. The thickness of the hydrate films should cause melting to start in the center of pores and not closer to the pore walls. Single component hydrate studies suggest residual hydrate films in the center of the pores forms due to residing water droplets underneath the gas phase. In contrast to pure methane hydrate studies, local accumulation of CO_2 could cause residual hydrate films.

Single component hydrate film dissociation

Figure 4-16 demonstrates single component hydrate film dissociation in experiment 3. Crystalline hydrate, hydrate film, gas, water, and grains are shown in the sequence and denoted as H, Hf, G, W and R respectively. Image A shows the pore space filled with hydrate films, hydrate and grains at 18

bar prior to dissociation. Hydrate grown in water is nearly impossible to spot in image A, because of almost equal refractive index as water. These hydrates are identified when hydrate film has dissociated, and gas starts to flow. Image B shows the initial dissociation indicated by a yellow circle. Figure 4-2 described increased hydrate saturation caused by growth in water. The hydrate films enclosed by the red circle in image C formed like this. During dissociation, this hydrate melted and converged into the residual hydrate. Image D illustrates a boundary marked by red lines between liberated water and the hydrate grown in water (red circle image C). This boundary is more significant in image E, where hydrate film has completely dissociated and liberated gas flows freely in the pore channels. The interface between water and residual hydrate becomes more visible when gas has retracted, and the white arrows in the image indicate free water. Image F shows the complete dissociation of the residual hydrate.

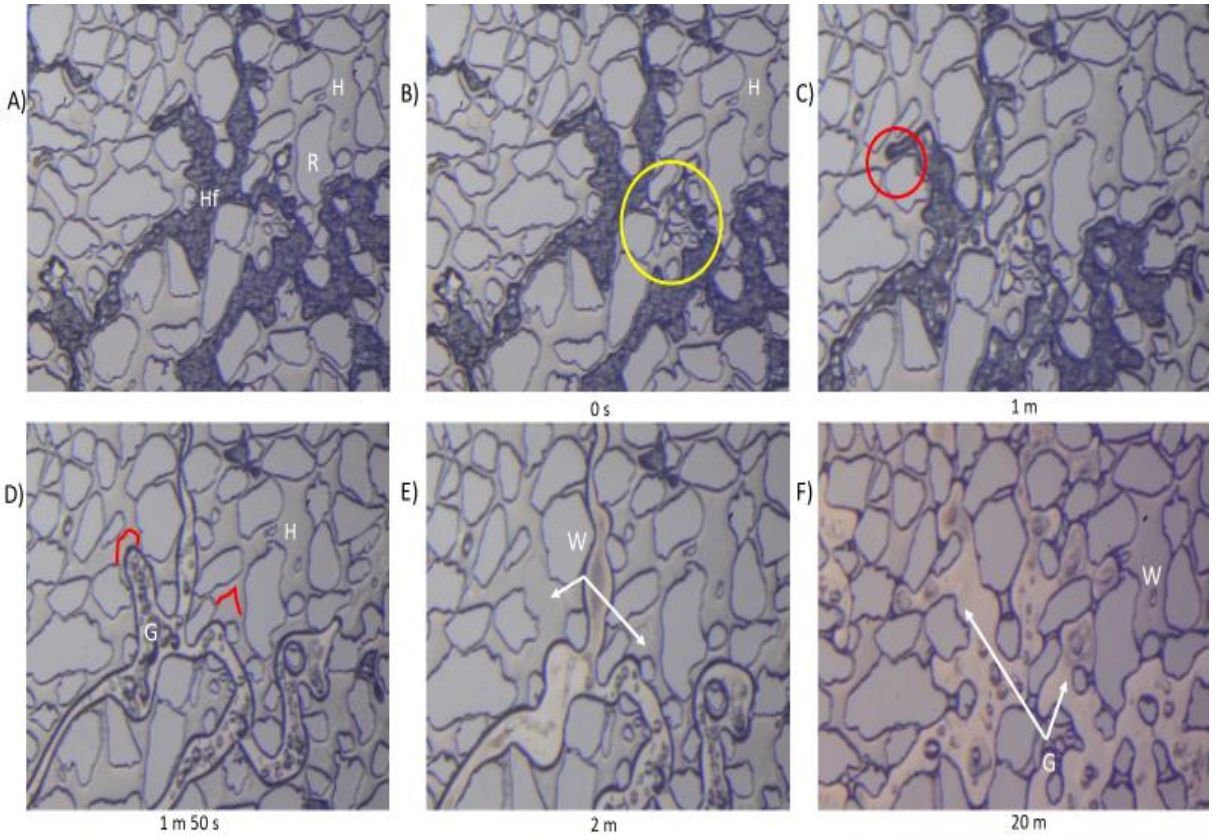

Figure 4-16 - Single component hydrate film dissociation with liquid CO_2 in experiment 3. A) Initial saturation before dissociation where hydrate, hydrate film and grains are present. B) Hydrate film starts to melt, indicated by yellow circle. C) Further hydrate film dissociation, red circle indicates hydrate grown in water after hydrate film enclosed available liquid CO_2. D) Hydrate film dissociates from center of pores towards pore walls. Red lines indicate the interface between hydrate in water and released water from hydrate film. E) Hydrate film has completely dissociated, and gas is mobilized, pore space consists of hydrate and water. F) Complete dissociation.

Crystalline mixed hydrate dissociation

Crystalline mixed hydrate dissociated very fast, in less than a second. Crystalline mixed hydrate dissociated much quicker than a single component hydrate film. Figure 4-17 illustrates the dissociation, where image A) shows the pore space is filled by crystalline mixed hydrate, hydrates grown in water, grains and liberated gas flowing on top of the crystalline hydrate. In image B, the crystalline mixed hydrate dissociates rapidly in less than a second. Image C illustrates gas liberation from adjacent hydrate or diffusion through wetting films from a nearby gas phase. Similar behaviour is seen in image D where a new gas bubble is liberated from a nearby hydrate structure. Both gas bubbles in image C and D connects to a free gas phase. Image E shows a small separation characteristic between two separate components. The difference between these two components is segmented in image F.

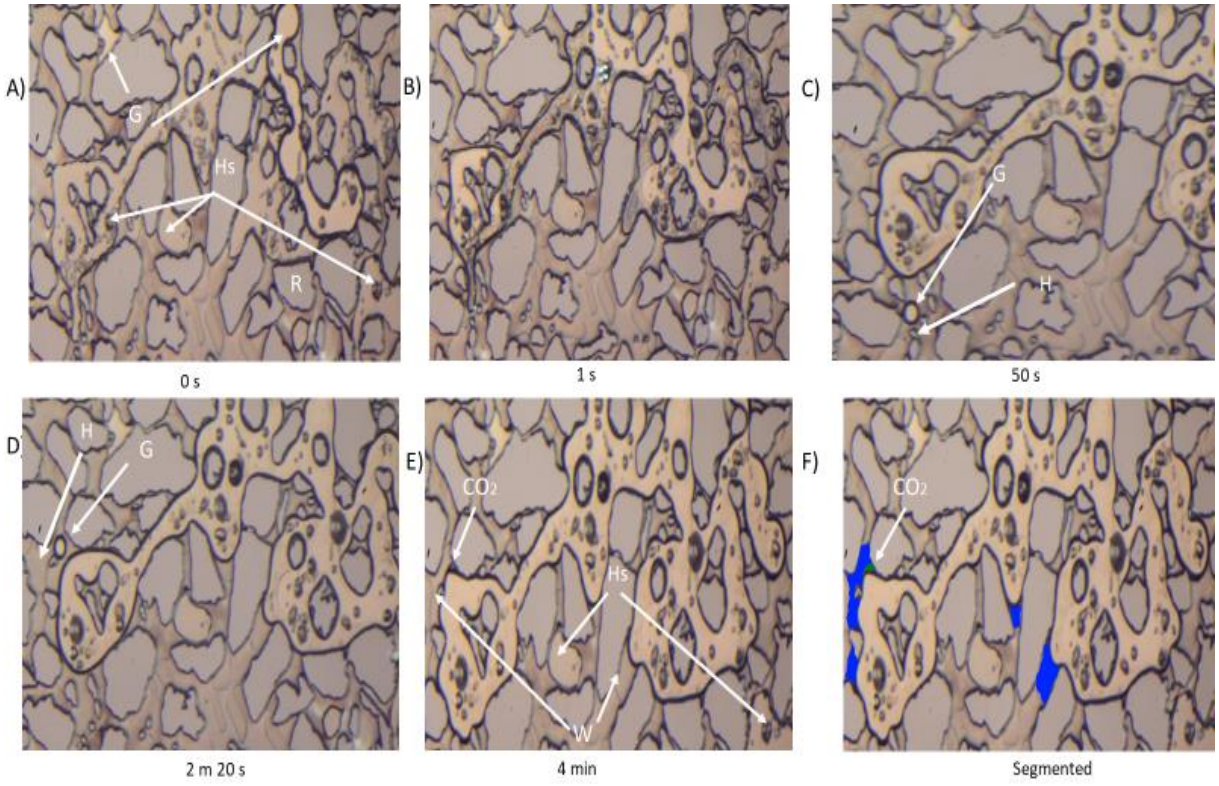

Figure 4-17 - Dissociation of crystalline hydrate in experiment 8. Crystalline mixed hydrate, hydrate, gas, water and grains are denoted as Hs, H, G, W and R respectively. A) Before dissociation at 19 bar, crystalline mixed hydrate, hydrate, gas (free gas on top of crystalline hydrate and in narrow pore throat) resides in pore space. B) Crystalline hydrate dissociates in less than a second. C) Dissociation of gas bubble either from surrounding hydrate or diffused from surrounding free gas phase through wetting films. D) Shows a dissociated bubble released from hydrate in water connecting to free gas. E) Shows pore space after four minutes where a separate component has formed underneath the gas phase indicated by white arrow presumably CO_2. F) Segmented image of image E as a better illustration of separate components where water and separate component is segmented blue and green respectively. Gas, hydrate and grains remained unsegmented.

The crystalline morphology is a mixed hydrate formed by a mixed composition of liquid CO_2 and CH_4. The gas composition in the hydrate at 19 bar will consist of 96.62 % and 3.38 % CO_2 and CH_4 respectively. This emphasizes the importance of a stepwise pressure reduction to quantify if a mixed hydrate formed. The Quizix pump has an uncertainty of ± 1.4 bar, which gives the composition fraction of CH_4 to be in the range of 0 - 24 %. Gas characteristics appear to be methane, due to its white and transparent surface, whereas gaseous CO_2 has a dark transparent surface illustrated in Figure 4-21. Image F shows separation characteristics of three components, where water is segmented in blue and what seems to be CO_2 in green. The observation of two separated components could indicate mixing of two gas components is limited when pressure and temperature conditions are within the GHSZ. The separated component underneath might indicate a hydrate film configuration underneath restricts two gas phases to mix.

Multicomponent hydrate dissociation

Hydrate dissociation was observed from crystalline and hydrate film morphology. A dissociation was identified when there was a visual observation of a released gas bubble in the FOV or a gas volume expanding over hydrate, as seen in Figure 4-19 and Figure 4-20. A counterargument to increased gas saturation as a dissociation point is that gas expands at lower pressures. Hydrate in contact with water should favour dissociation because water has a higher heat conductivity than gas. However, experimental work in micro models shows that hydrate tends to dissociate in contact with gas instead of water (Almenningen *et al.*, 2017). The low permeability caused by pore occupation of hydrate constraints mass transport and production of liberated CH_4 to diffusion through wetting films.

Zhou (Zhou *et al.*, 2016) used Raman analysis to investigate crystalline mixed hydrate dissociation. They suggested the crystal structure collapse as an entity and the gas molecules escape directly without diffusing into the ambient hydrate crystals. These results propose that small cavities with methane molecules will dissociate first, and the hydrate structure containing CO_2 molecules will further collapse.

For a mixed phases encapsulated by hydrate films, gas liberation might be controlled by diffusion through the hydrate film. Hydrate films will presumably be thinner at pressures below the equilibrium to CH_4 hydrate, giving molecules easier and accelerated diffusion compared to thicker hydrate film at formation pressure above 60 bar. Figure 4-18 illustrates a diffusion mechanism for molecules through hydrate films. The model shows a hydrate above equilibrium in the GHSZ to the left, and hydrate outside the GHSZ to the right, where hydrate film is thinnest in pore center and becomes thicker closer towards pore walls (Hauge *et al.*, 2016). Hydrate films are thickest in the pore corners and gives the gas a shorter diffusion path through the pore center where hydrate film is

thinnest. Also, released gas bubbles were observed to increase from pore walls in narrow pore throats. This suggests gas will diffuse through hydrate films in the pore center and escape towards water wetting films to an adjacent/associated gas phase. If free gas is not available, the released gas will accumulate and increase in volume as more gas is released throughout the dissociation process.

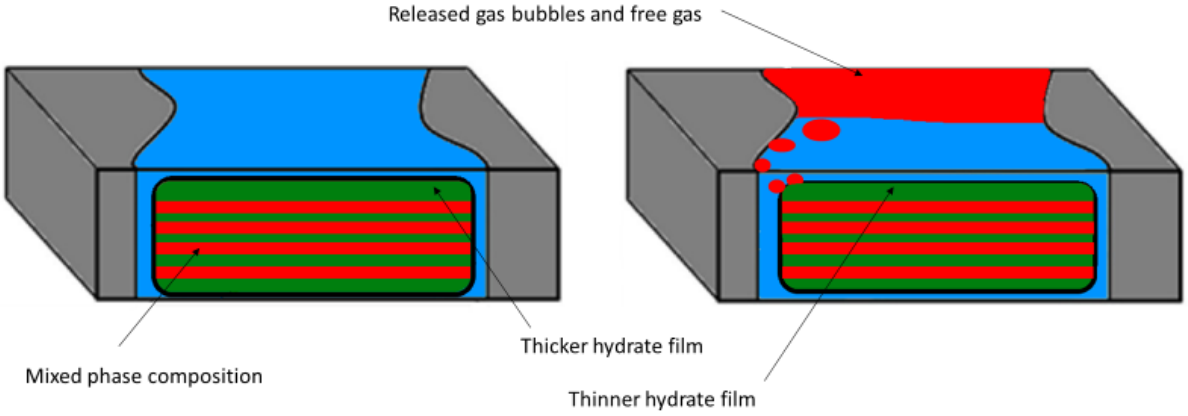

Figure 4-18 - Conceptual model illustrating dissociation of a mixed hydrate through hydrate film. The mixed phase composition in the figure to the left illustrates a mix of CO_2 (green) and CH_4 (red) at formation pressure. The figure to the right illustrates a dissociation mechanism for a mixed gas composition below P_{eq,CH_4}, with CO_2 (green) and CH_4 (red).

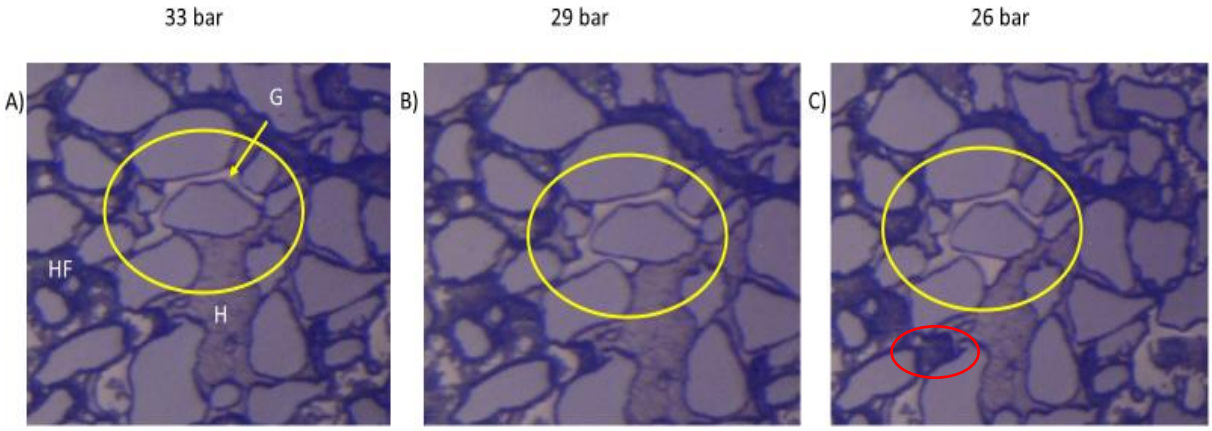

Figure 4-19 –Illustration of mixed hydrate dissociation in experiment 4, where the equilibrium pressure to methane hydrate was 32.34 bar. Crystalline hydrate, hydrate film and gas are denoted as H, HF and G respectively. A) Initial saturation at 33 bar where the pore space is filled with hydrate film (HF), crystalline hydrate and a gas phase inside the yellow circle. B) Pressure is reduced to 29 bar and the gas volume increase towards pores filled with crystalline hydrate. C) Pressure is reduced to 26 bar and the gas volume continues to expand towards pores filled with crystalline hydrate. Another observation is that hydrate film has encapsulated more of the gas in the bottom left perhaps because of released water transferred through the wetting film from crystalline hydrate dissociation.

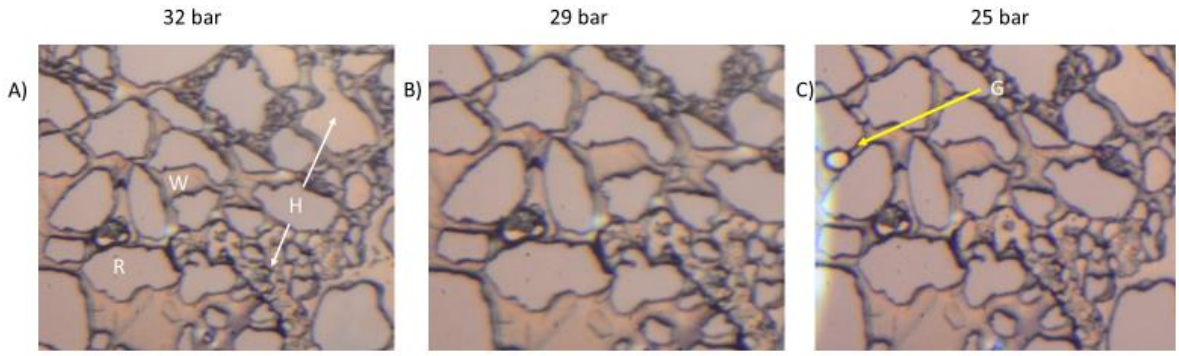

Figure 4-20 - Illustration of mixed hydrate dissociation mechanism by the release of gas in experiment 6 where the equilibrium pressure to methane was 31.01 bar. Crystalline hydrate, gas, water and grains are denoted as H, G, W and R respectively. A) Pore space is filled with crystalline hydrate (liquid CO_2), hydrate crystals formed in water, water pocket and grains at 32 bar. B) Pressure is reduced to 29 bar without any dissociation. C) A gas bubble is released in the pore throat at 25 bar.

Figure 4-19 and Figure 4-20 show two different dissociation mechanisms. In Figure 4-19, hydrate is dissociating, and gas is released to a trapped gas phase. The gas phase is increasing in volume towards the crystalline hydrate at each pressure step. The liberated gas can also diffuse from adjacent areas partially encapsulated by hydrate films (shown to the left in the images). As seen in Figure 4-19 (A-C), hydrate film is forming and encapsulating more gas when reducing pressure from 33 to 26 bar due to the supply of water through wetting films from crystalline hydrate dissociation. In Figure 4-20, hydrate dissociation leads to a liberated gas bubble. With no trapped gas present, the gas bubble expands in a pore throat and accumulates to a bubble.

Additional observations

Figure 4-21 shows an observation where two gas phases are inhibited from mixing. Pressure reduction below the liquid/gas boundary to CO_2 will form a system consisting of two components in the gaseous state. By theory, CO_2 and CH_4 in a gaseous state should mix and form one gas phase at the interface by molecular diffusion. The image sequence shows the pore space of two separate gas components after hydrates have dissociated and CO_2 and CH_4 are liberated. At the pressure and temperature conditions, the components should mix into one gaseous phase, but they were observed to remain separated if residual hydrate maintained in pore space. A hydrate film between the CO_2 and CH_4 could be the explanation of restricted mixing. The components were observed to flow as a unit and not as separate components could support the proposed hydrate film separation theory.

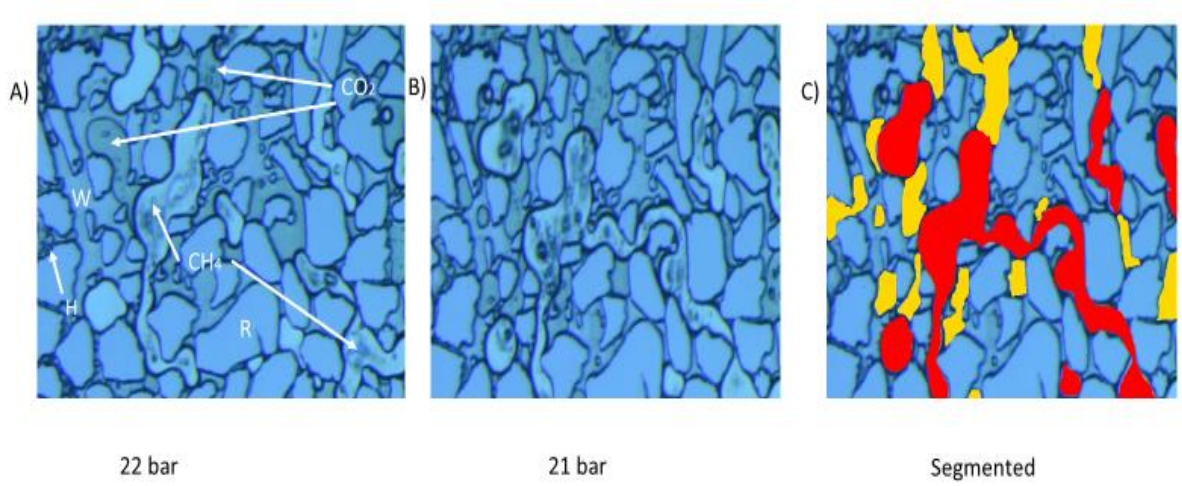

Figure 4-21 – Two separate gas phases in experiment 19. Gaseous CO_2 and CH_4, hydrate, water and grains are denoted as CO_2, CH_4, H, W and R respectively. Image shows pore space during dissociation where hydrate has liberated two gas components at 22 bar. Image B shows pore space after one pressure step and no mixing. C) Image B segmented, where yellow represents CO_2, red represents CH_4 and hydrate, water and grains remain unsegmented.

Effect of CO_2 liquid/gas boundary

CO_2 can exist in both liquid and gaseous state. The saturation/vapor pressure to CO_2 is as a function of pressure and temperature. A web computational tool based on the work of Span and Wagner(Span and Wagner, 1996), made by Zhao (CO2 calculator - A web computational tool, 2015) was utilized to calculate the liquid/gas pressure boundary to CO_2 at different temperatures shown in Figure 4-22. The two grey points illustrate observed CO_2 phase conversion and will be discussed in detail in section 4.3.2.

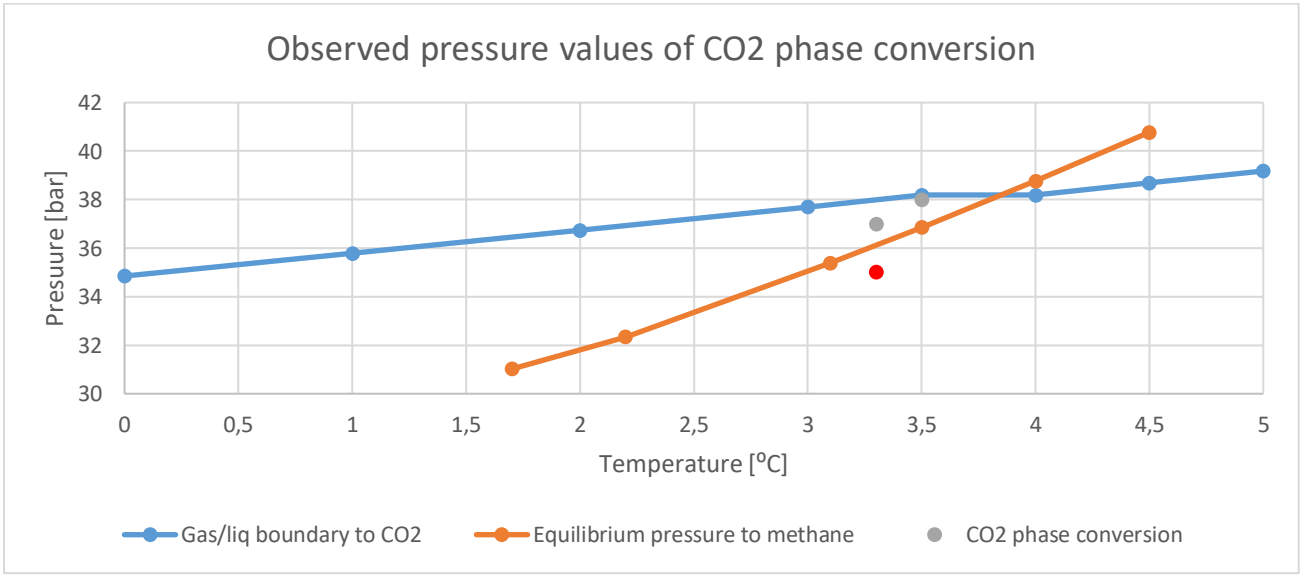

Figure 4-22 - Plot of liquid gas boundary to CO_2, equilibrium pressure to methane and observed points where CO_2phase conversion occurred. The blue line show liquid/gas boundary to CO_2 as a function of temperature calculated by CO2 calculator- A web computational tool (CO2 calculator - A web computational tool, 2015). The orange line shows the

equilibrium pressure to CH_4 as a function of temperature. The three single points show observed CO_2 phase conversion at different pressures and temperatures. The upper grey dot is experiment number 10 and the lower grey point is experiment number 2. The red dot represents single component experiment number 3.

Figure 4-23 demonstrates the impact of pressure reduction in experiment 3 (red dot in Figure 4-22) when hydrate films encapsulated liquid CO_2. The formation of this hydrate is explained in section 4.1.1. This hydrate configuration responded to pressure reduction below the liquid/gas boundary to CO_2 at 37,99 bar, by a propagating front through the hydrate films. This phase conversion changed the hydrate film colour from light grey to a darker hydrate film in less than 4 seconds. The wave propagation could be the conversion of liquid to gaseous CO_2. This sequence shows that hydrate films tend to have a darker film morphology when it encapsulates transparent colourless gases. Moreover, hydrate films encapsulating liquids (like liquid co2 which has a dark grey morphology), hydrate films tend to take the same colour as the liquid.

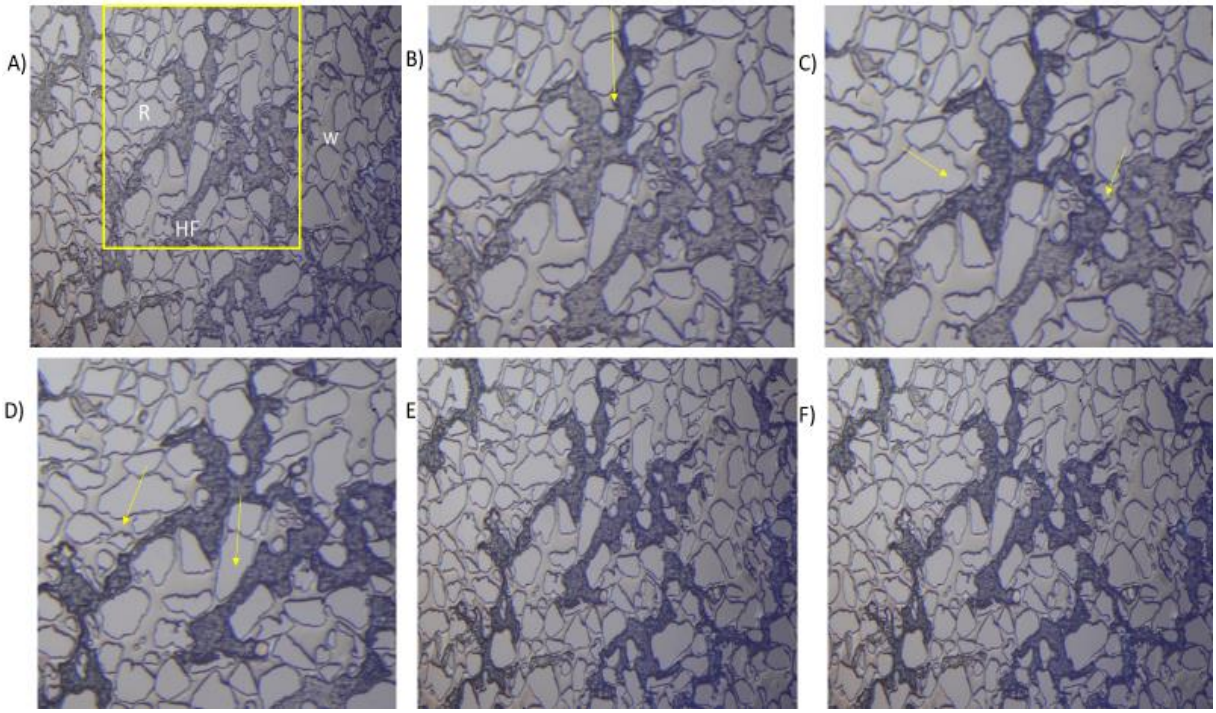

Figure 4-23 – Change of hydrate morphology by reducing pressure below the CO_2 liquid/gas boundary in experiment 3 at 3.3 ^{o}C. R, W, HF denotes grains, water and hydrate film respectively. While the yellow square indicates the cropped area of image (B, C, D). A) Initial saturation at 36 bar. B) Cropped image of the yellow square in image A where the propagating front is moving from top outside of image, yellow arrow indicates front propagation. C) Same area as image B where yellow arrows denote front propagation. D) Same area as image B and C where yellow arrows denote the direction of the propagating wave. E) Show the whole FOV when the conversion was complete. F) Shows the whole FOV just before the next pressure step.

4.3.2 Mixed hydrate reformation

Reformation of hydrates is one of the challenges in terms of extracting natural gas from unconventional and conventional reservoirs. Reformation of hydrates occurs due to altered pressure and temperature conditions. The potential risk of hydrate reformation can plug a flowline in up-, mid- and downstream industry or plug the pores in the reservoir. Hydrate reformation can be a sign of altered mixed hydrate composition, with a lower fraction of CH_4 and a higher mole fraction of CO_2. In this work, hydrate reformation was observed several times during stepwise pressure depletion. Carefully controlled pressure depletion after a CO_2 injection could lead to a higher production of methane and formation of mixed hydrates with a higher mole fraction of CO_2.
This section relates to one form of reformation after primary mixed hydrate formation or CO_2 injection. The phenomenon of hydrate reformation is categorized as; 1) hydrate reformation and dissociation at the same pressure step, 2) hydrate reformation stable over several pressure steps.

Reformation above CH_4 hydrate equilibrium pressure

There were observed two types of reformation above the equilibrium pressure to pure CH_4 hydrate. The first observation is related to a spontaneous conversion below liquid/gas boundary to CO_2 and above pure CH_4 hydrate equilibrium pressure. The second, is related to water invasion below the liquid/gas boundary to CO_2 and above pure CH_4 hydrate equilibrium pressure.

Reformation above the equilibrium pressure to pure CH_4 hydrate can be phase conversion of liquid CO_2 to gas, although the observation could not be seen directly in the FOV. Uchida reports that gas bubble formation inside the hydrate lattice can destabilize the cavity structure and release gas and water (Uchida *et al.,* 2000). A phase conversion will lead to an increased number of gas molecules moving freely inside the hydrate lattice. Gas movement generates vibration and releases heat inside the hydrate cavity, and this can induce hydrate dissociation. Figure 4-24 demonstrates hydrate reformation below the liquid/gas boundary to CO_2 and above the equilibrium pressure to pure CH_4 hydrate. The porous media was initially saturated with a mixed composition of CH_4 and liquid CO_2, making a crystalline hydrate (H), free gas layer above hydrate (G) and grains (R) in image(A). A layer of free gas displays a system where all free water is consumed to form hydrate and this configuration is called an excess gas system. The temperature was set to 3.3 ^{o}C giving the equilibrium pressure to CH_4 hydrate at 36.117 bar and the liquid/gas boundary to CO_2 at 37.99 bar. Gas increased in volume by occupying all pore space in image (B), when the pressure was reduced from 38 to 37 bar. After 33 minutes of staying at constant pressure at 37 bar, gas is displaced either by dissociated water outside the FOV or by hydrate dissociation in the FOV in image (C). Free water starts to capture the gas and form hydrate films in image (C) and (D), and further gas consumption leads to crystalline hydrate growth in image E and F.

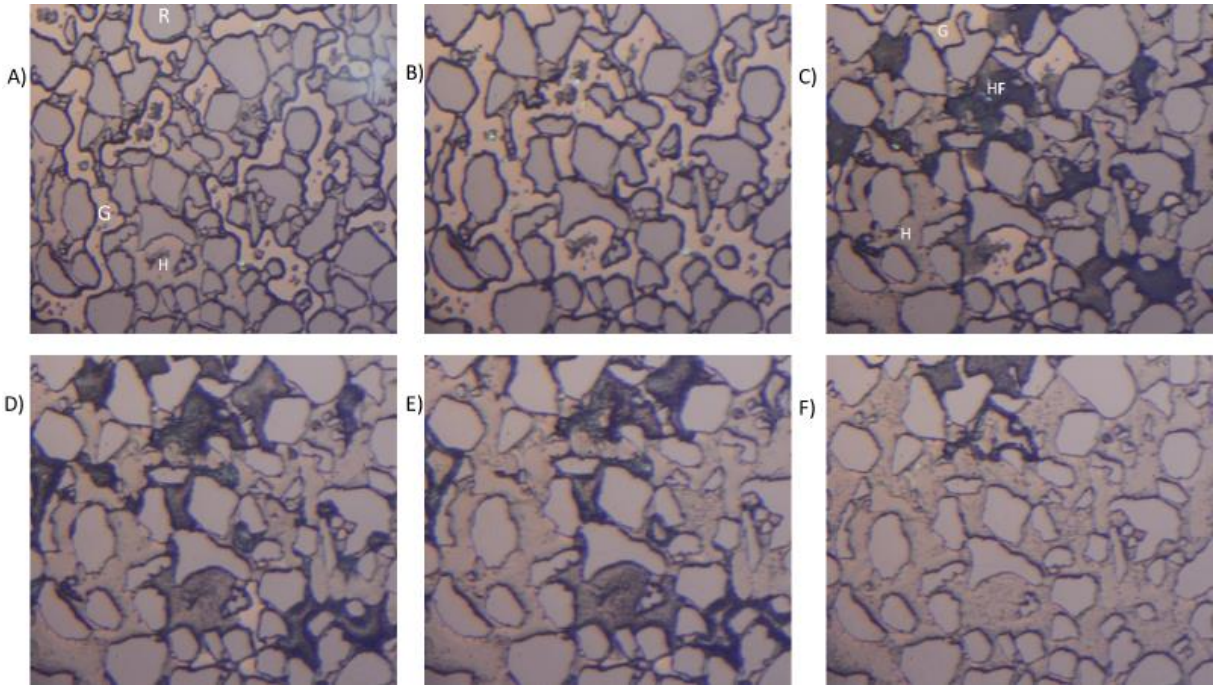

Figure 4-24 – Reformation between the liquid/gas boundary to CO_2 and methane hydrate equilibrium pressure in experiment 2. A) Initial saturation with solid hydrate with free gas layer on top. B) Gas volume expands. C) Water invades some of the pores leading to gas displacement and hydrate reformation. D) Hydrate growth from film to crystalline morphology. E) Hydrate film growing to crystalline hydrate. F) Crystalline hydrate

The observation illustrates a reformation that might be caused by a liquid CO_2 conversion to gas inside the hydrate lattice. The claim for this reasoning is after the formation of mixed hydrate, the system was left for 20 hours at formation pressure. Reportedly, 20 hours is enough time for free gas to be consumed into hydrate. Gas consumption did not occur during these 20 hours and left the system with a mobile free gas layer above the crystalline mixed hydrate.

Figure 4-25 demonstrates pressure reduction below the liquid/gas boundary to CO_2 in experiment 10. The pore space was initially filled with hydrate film, water and grains at 39 bar. The temperature was set to 3.5 ^{o}C, giving the liquid/gas boundary to CO_2 at 38.18 bar, and the equilibrium pressure to CH_4 hydrate at 36,852 bar (Colorado School Of Mines, 2015). In image A, shows the pore space is filled with hydrate films and small isolated water pockets. At this point, hydrate has not converted to crystalline hydrate due to lack of available water. In image B, the pressure is reduced to 38 bar, below the liquid/gas boundary to CO_2. After 18 minutes staying at 38 bar water flows through the pores in less than a second. Image (C) and (D) shows water propagates through the pore space before it is terminated in image (E). In image (F), smaller areas with hydrate films have transformed to crystalline hydrate due to water supply, indicated by the yellow circles. Also, crystalline hydrate grow in water and large areas with hydrate films develops a thicker hydrate film morphology.

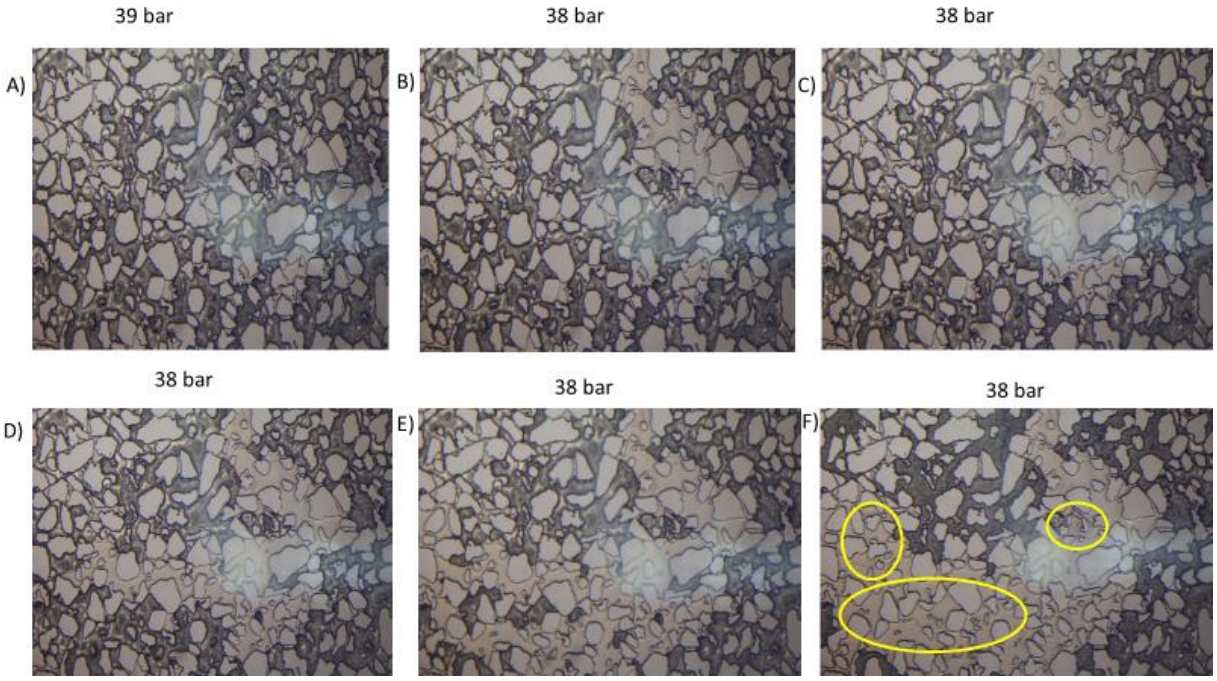

Figure 4-25 – Pressure reduction below the liquid/gas boundary to CO_2 in experiment 10. The time interval from image (B) to (F) is 3 seconds.

The observation in experiment 10 shows similar water invasion as described in section 4.2.1. In section 4.2, hydrate film transformed into crystalline hydrate because of additional water. The sequence in Figure 4-25 shows hydrate film thickening and not further growth into crystalline hydrate. Exchange experiments were conducted above 60 bar and Figure 4-25 describes a water invasion at 38 bar. A lack of driving force could explain the absence of hydrate film conversion to crystalline hydrate.

To summarize; a mixed composition of liquid CO_2 and CH_4 gas forms a pressure inside the hydrate lattice equal to the equilibrium pressure of the mixed hydrate. The equilibrium pressure to a mixed composition is below the equilibrium pressure to pure CH_4 hydrate. When liquid CO_2 molecules is encapsulated in the hydrate lattice it should by theory experience phase conversion to a gaseous state. Increased water saturation occurred in a stable hydrate system below the liquid/gas boundary to CO_2 and above the equilibrium pressure to CH_4 hydrate in experiment 2 and 10. The following proposal is based on sufficient pore pressure blocks the conversion of liquid CO_2 to gaseous CO_2. A hydrate system should be stable above CH_4 hydrate equilibrium pressure and below liquid/gas boundary to CO_2. Based on these observations, pressure reduction could initiate a double conversion effect. 1) gaseous CH_4 evaporates from liquid CO_2. 2) with following phase conversion of liquid CO_2 to gaseous CO_2. Pressure reduction below the liquid/gas boundary to CO_2 could be an initiation

factor for CO_2 to change its state. This conversion will generate volume expansion and vibration towards the hydrate lattice, causing hydrate cages to destabilize and dissociate, releasing water to flow through the pores.

There was no observation of released gas, and crystalline hydrate growth initiated in water after the flow of water ceased. This is an indication that the released gas dissolves in water and is a favourable mechanism for dissolution trapping of CO_2 in water for CCUS applications.

Dissociation – reformation above a hydrate layer

Below CH_4 hydrate equilibrium pressure, gas will dissociate by the mechanisms reported in section 4.3.1. Free gas will gradually increase in volume from a bubble to a continuous phase. Alternatively, liberated gas will increase the volume of an existing continuous gas phase. Figure 4-26 demonstrates the reformation of liberated free gas above a hydrate layer. Image A shows initial saturation after formation where the FOV consists of crystalline hydrate, hydrate film (yellow circle), grains (R) and water (W) at 24 bar. In image B, the pressure is reduced to 23 bar and a gas bubble is liberated. In image C and D, gas diffuses from the hydrate film area following the yellow line and liberated gas accumulates above the crystalline hydrate at 21 bar. In image E, the liberated gas solidifies and becomes immobile at 21 bar. In image F, the pressure is reduced by two pressure steps to 19 bar, and the liberated gas is still in a solidified state while hydrate film inside the yellow circle has dissociated.

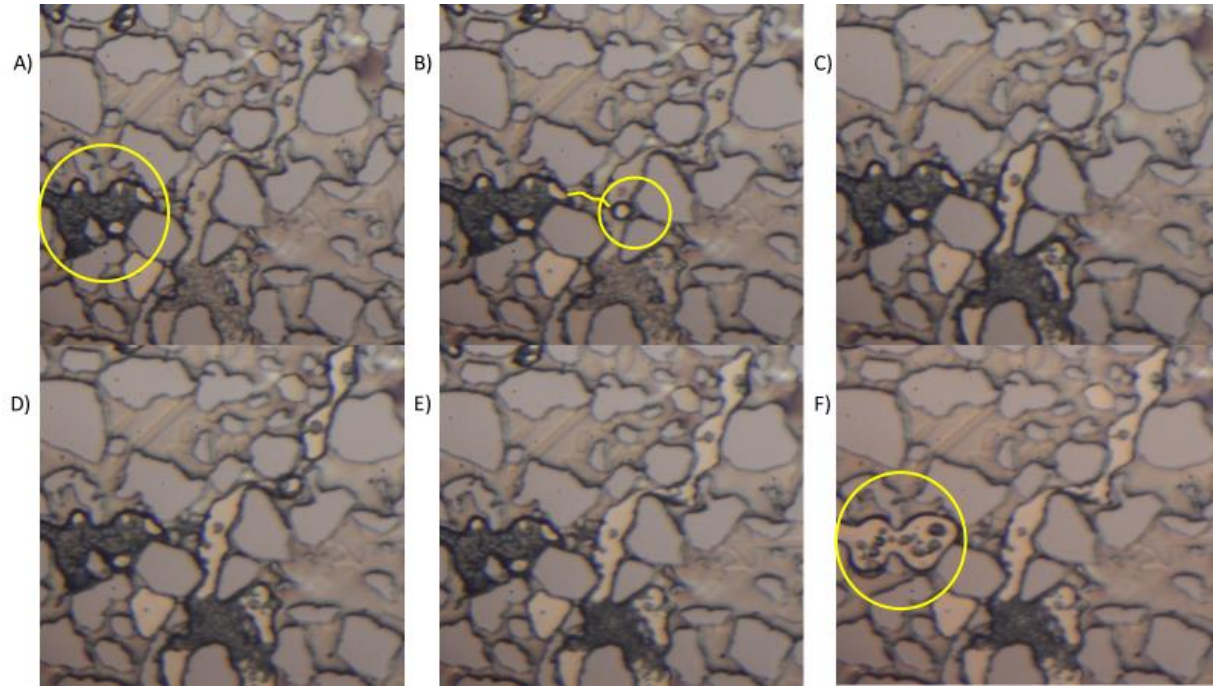

Figure 4-26 – Reformation sequence in mixed hydrate experiment 8. A) 2Initial saturation at 24 bar, the yellow circle shows gas encapsulated by hydrate film. B) Hydrate dissociation at 23 bar, first point of dissociation (yellow circle). Yellow line

indicates that gas is transported through the wetting film (possible to see by video, but not by images). C) Shows increased gas volume at 21 bar. D) Increase of gas volume at 21 bar. E) Hydrate encapsulates the gas volume at 21 bar. F) Reformed gas volume is still solid in solid phase while hydrate film in yellow circle dissociates at 19 bar.

The liberated gas flowed on top of hydrate with crystalline morphology and did not expand across the FOV. Once it appeared on top of hydrate, it stayed immobile. If this was caused by constant pressure or formation of hydrate film between the two phases is not clear. The gas volume continuously increased over the crystalline hydrate. Reformation can be caused by the endothermic nature of dissociation, creating a local cooling effect causing a driving force by shifting the equilibrium line to lower temperatures. Both gases, CO_2 and CH_4, are transparent and difficult to distinguish above a hydrate layer. CSMGem quantifies the hydrate gas composition at 23 bar and 3.5 ^{o}C to be 54 % CO_2 and 46 % CH_4 (image B). The hydrate stayed stable until pressure was reduced below pure CO_2 hydrate equilibrium at 18 bar. If the system is unaffected by cooling effects, it is reasonable to believe that CO_2 diffused from the hydrate film towards the crystalline hydrate.

Crystalline hydrate reformation of liberated gas in contact with crystalline hydrate

Figure 4-27 demonstrates the reformation process during stepwise dissociation in experiment 10. Crystalline hydrate (H), gas encapsulated by hydrate film (HF), gas (G), grains (R) and water (W) are present in the image sequence denoted as H, HF, G, R and W respectively. In image A, all the above mentioned except free gas is present in pore space at 28 bar. Image B shows the dissociation of crystalline hydrate at 27 bar. The hydrate gas composition dissociating at 27 bar and 3.5 ^{o}C is calculated by CSMGem to be 33 % CO_2 and 67 % CH_4. Image C shows further dissociation at 25 bar, the composition of the hydrate dissociating at 25 bar is 42.5 % CO_2 and 57.5 % CH_4. Image D shows the start of gas consumption in the reformation of hydrate at 25 bar. In image D, hydrate reformation consumes the free gas before total gas consumption has occurred in image E at 25 bar. Image F shows the whole FOV at 19 bar, where the yellow square denotes the cropped FOV in image A-E.

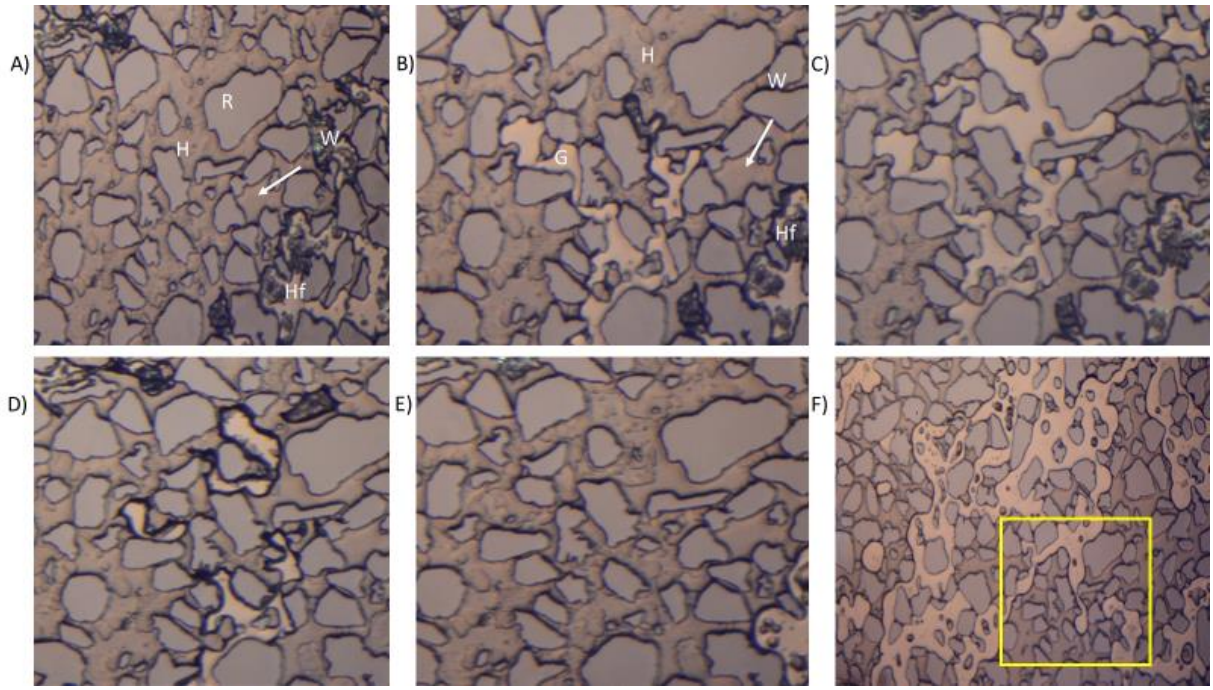

Figure 4-27 - Reformation of liberated gas in experiment 10. All images are magnified from the original field of view except (F). A) Initial saturation at 28 bar, bottom right shows hydrate film melting. B) Gas dissociation from crystallized hydrate at 27 bar. C) Start of reformation at 25 bar. D) Hydrate almost crystallized again at 25 bar. Water saturation is higher after the reformation. E) All gas is consumed after reformation at 25 bar. F) Dissociation at 19 bar. The yellow square marks FOV in image A to E.

The reformed crystalline hydrate was observed to dissociate over several pressure steps and dissociated in contact with liberated gas from adjacent areas in the FOV. Released gas bubbles were not observed implying the free gas phase increases in contact with hydrate, or the gas escaped through wetting films.

Dissociation – reformation – dissociation at the same pressure step

Previous discussions of reformation are linked to hydrate stability over several pressure steps. The process reformation-dissociation at the same pressure step was observed as well. This was not a common observation, but it was related to high water -, high gas- and low hydrate saturation with sufficient driving forces. The next figure illustrates the reformation-dissociation at 28 bar and 3 ^{o}C in experiment 7. The mixed hydrate dissociated overnight at 30 bar leaving the pore space filled with crystalline hydrate, hydrate film, water and isolated gas bubbles. Further pressure reduction led to the complete dissociation of hydrates. Image A shows the pore space just before hydrate reformation at 28 bar. CSMGem calculates the hydrate gas composition to be 22.7 % CO_2 and 77.3 % CH_4 at 28 bar. In image B, hydrate film encapsulates the free gas phase. The film development initiated from the water-gas interface and propagated through the gas phase and grew towards the pore center. In image C, hydrate films have evolved to crystalline hydrate, indicated by the yellow

lines, leaving two areas with gas enclosed by hydrate film. Image D shows hydrate dissociation indicated by the green rectangle in image C and D. Surrounding pore space has been filled by gas, probably caused by dissociation outside the FOV. The lower red circle indicates residual crystalline hydrate in image D. In image E, crystalline hydrate continues to dissociate in contact with free gas. In image F all reformed hydrates have dissociated at the same pressure step in less than 15 minutes.

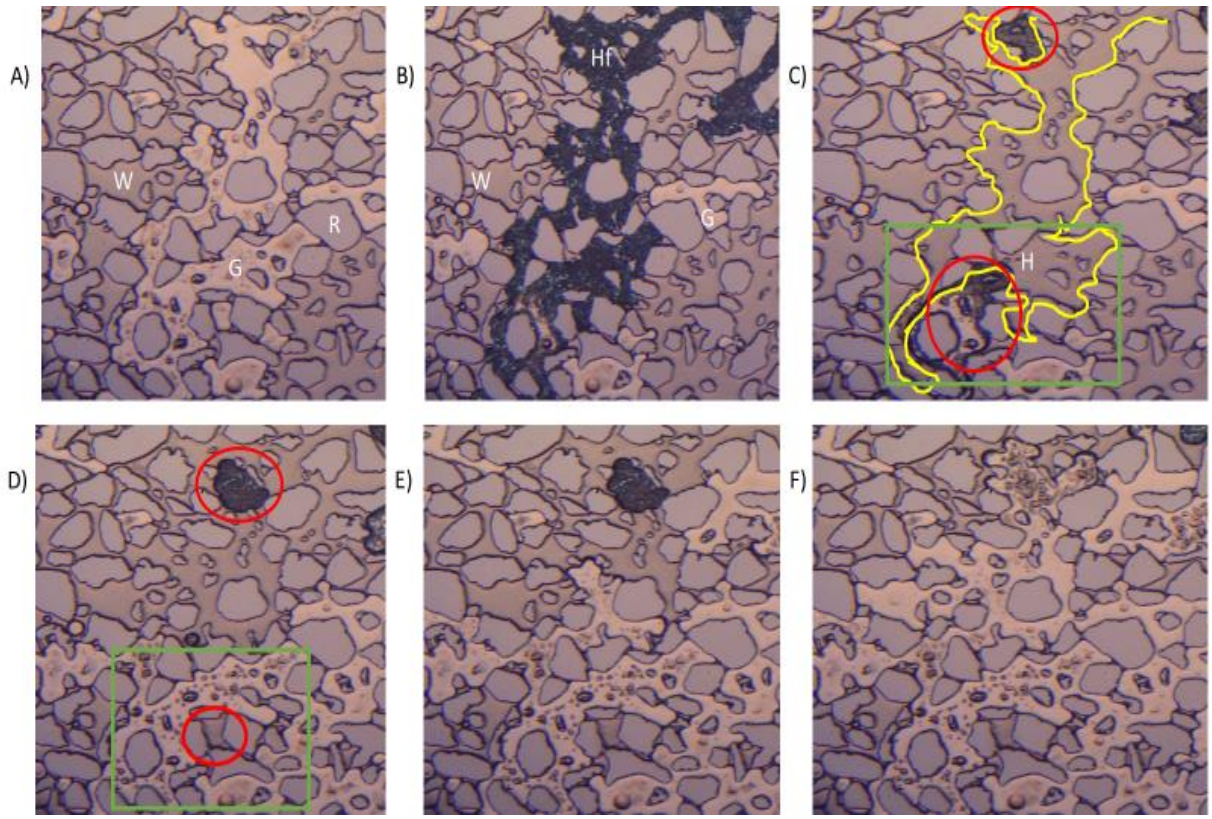

Figure 4-28 - Reformation and dissociation at the same pressure step in experiment 7. A) Initial saturation where gas, water and grains are denoted as G, W and R respectively. B) Gas is encapsulated by hydrate film. C) Hydrate film in pore space between yellow lines crystallizes leaving two areas with free gas enclosed by hydrate film inside the red circles. D) Crystalline hydrate and hydrate film start to dissociate. E) Dissociation propagates towards the top of image. F) All hydrate has dissociated.

This sequence illustrates the reformation of an unstable system that reformed and dissociated at the same pressure step. Thermocouple registered fluctuations in the range of ± 0.1 ^{o}C, which is within the limit of uncertainty. The endothermic nature of dissociation, together with the memory effect in the water, can cause a shift in the equilibrium line. There are no reports of how long a local cooling effect endures in the pore space. However, reformed mixed hydrates dissociated at the same pressure step when the gas composition of 22.7 % CO_2 and 77.3 % CH_4. The low mole fraction of CO_2 might indicate that reformed mixed hydrates need a mole fraction of CO_2 higher than 22.7 % to be stable at low driving forces. The lowest reformed hydrate gas composition that remained stable after further pressure reduction was 42.5 % CO_2 and 57.5 % CH_4.

4.3.3 Molar compositions

Most of the study in this work is qualitative results. This section reports a quantitative calculation of the composition in the mixed hydrates, calculated by CSMGem. During a stepwise dissociation process, the phase equilibria for different systems can be calculated using a thermodynamic model such as CSMGem, see section 3.4 for the detailed procedure. The dissociation points are the equilibrium for the mixed hydrate and show how the molar gas composition changes during a stepwise dissociation. The molar compositions are plotted together with an upper and lower temperature limit calculated by CSMGem. If the temperature was 3.5 ^{o}C, the molar compositions are plotted together with the theoretical mixed hydrate equilibrium at 4 ^{o}C and 3 ^{o}C. Same yields for experiments conducted at temperatures between 1-2 ^{o}C and 2-3 ^{o}C.

Molar compositions after mixed hydrate formation between 3^{o}C and 4 ^{o}C

Figure 4-29 illustrates the change in molar compositions in experiments conducted in a temperature regime between 3 ^{o}C and 4 ^{o}C. Experiment 2 and 11, have the first point of dissociation in the mole fraction regime above 70 % CO_2. Pore space after formation in experiment 2 consisted of liquid CO_2 hydrate with high amounts of free gas on top of hydrate. Reformation above pure CH_4 hydrate equilibrium created another hydrate composition or perhaps two different hydrate structures, referring to 4.3.2 and Figure 4-24. With two dissociation points, one and two bar above pure CO_2 hydrate equilibrium shows a mixed hydrate formation with a very low mole fraction of CH_4. This can indicate that the free gas phase observed above the hydrate layer is a significantly smaller volume than the hydrate volume. If the free gas formed a pure methane hydrate, it would dissociate at higher pressures.

Experiment 11 was a case of very high-water saturation (0.95) and small amounts of liquid CO_2 and CH_4 gas before formation. Equilibrium pressure to pure CO_2 hydrate was 18.114 bar and dissociation was observed at 20, 19 and 18 bar. High water saturation leads to the assumption that the system contains more CO_2 than CH_4 because of the components solubility in water. This type of hydrate configuration will dissociate at low pressures and consists of high mole fractions of CO_2.

Gas- and water saturation in experiment 7 and 10 was (0.34, 0.66) and (0.61, 0.38) respectively. Liquid CO_2 was not observed during formation in experiment 7. In experiment 10, the liquid CO_2 saturation value, 0.01, is an underestimation because liquid CO_2 was observed to dissolve in water prior to the inflow of gas and formation. Comparison of the two experiments shows that both systems have dissociation points at high pressures. Experiment 7 has complete dissociation at 26 bar, whereas experiment 10 has several dissociation points from 28 bar to 19 bar, showing the effect of dissolved liquid CO_2 in water.

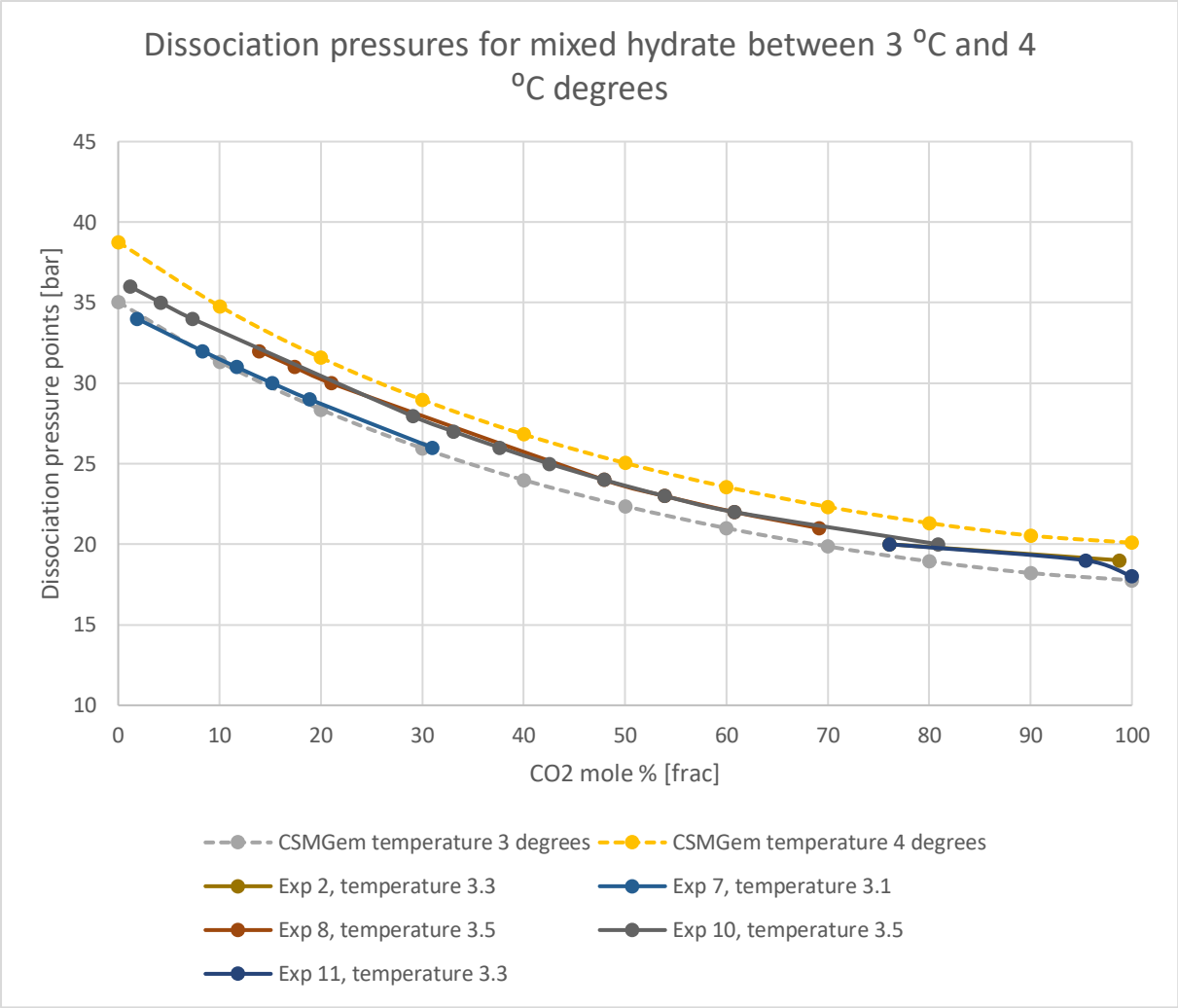

Figure 4-29 – Molar compositions for mixed hydrate experiments 2, 7, 8, 10 and 11 compared with theoretical equilibrium values in CSMGem at 3 °C and 4 °C.

Molar compositions after mixed hydrate formation between 2 °C and 3 °C

Experiments 4 and 5 were conducted at 2.2 °C. Both systems had high gas and low liquid CO_2 saturation. Experiment 5 had a single point dissociation at 26 bar even though there was no observation of liquid CO_2 before formation. In this experiment, hydrate films formed at 44 bar. 16 hours later, most of the hydrate films had melted in the center of pores and stayed intact towards pore walls. Reasons why this happened are still unclear, but could be similar mechanisms as described in Figure 4-8.

In experiment 4, water and gas were almost evenly distributed in the FOV with a small amount of liquid CO_2 at 50 bar. This system experienced hydrate film melting and increased gas saturation in the period between formation and the dissociation process. Nine dissociation points were observed where a significant dissociation at 24 bar left isolated residual hydrate crystals across the pores. These crystals dissociated and released gas bubbles by further pressure reduction where all hydrate

dissociated at 21 bar, 5 bar above pure CO_2 hydrate equilibrium pressure. This shows if liquid CO_2 cannot be seen in the FOV, it can be present in water or beneath the gas phase, contributing to a stable mixed hydrate down to 24 bar.

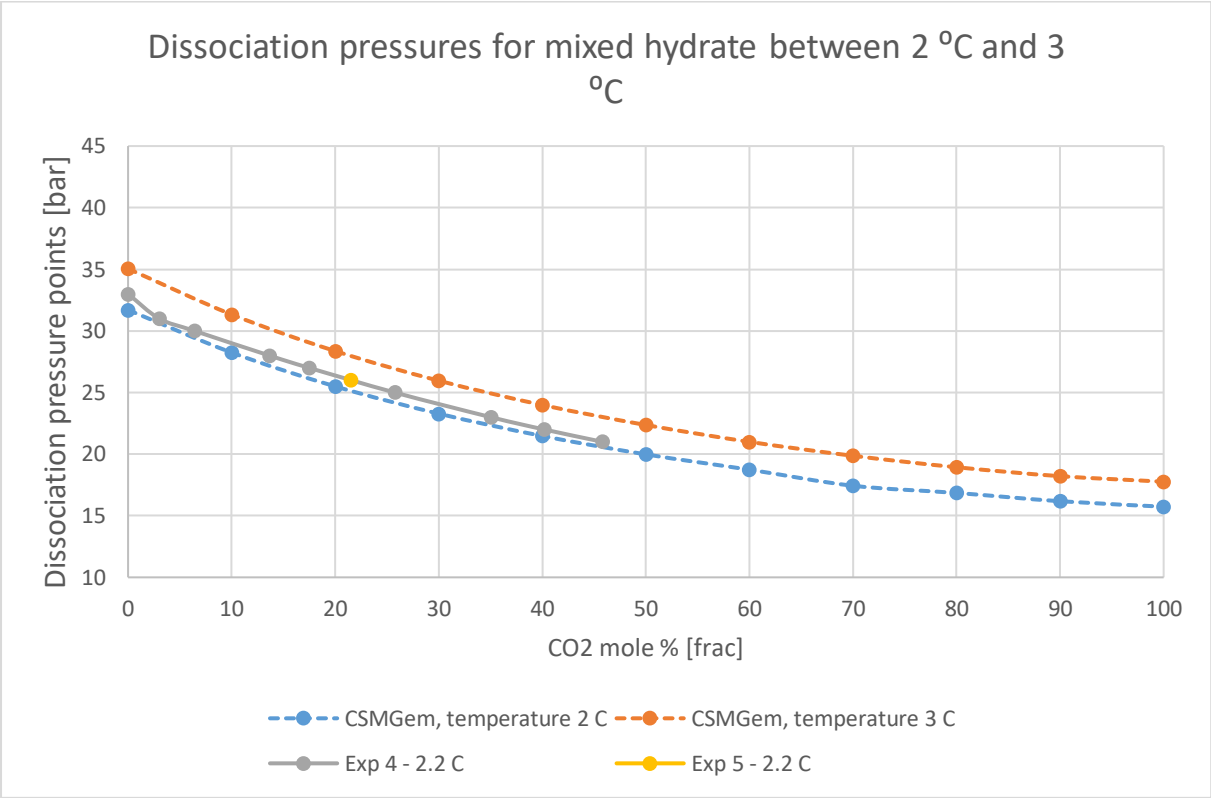

Figure 4-30 – Molar compositions for mixed hydrate experiments 4 and 5 compared with theoretical equilibrium values in CSMGem at 2 °C and 3 °C.

Molar compositions after mixed hydrate formation between 1 °C and 2 °C

Experiment 6 was conducted between 1 °C and 2 °C where the equilibrium pressure to pure CH_4- and CO_2 hydrate was 31.01 bar and 15.17 bar respectively. Saturation calculation before formation showed the system consisted of 3.88 % CH_4, 30.7 % liquid CO_2 and 65.5 % water. All hydrate dissociated one bar above pure CO_2 hydrate equilibrium at 16 bar with a hydrate gas composition of 78 % CO_2 and 22 % CH_4. The gas composition may indicate a significant amount of CH_4 dissolved in the liquid CO_2 before formation.

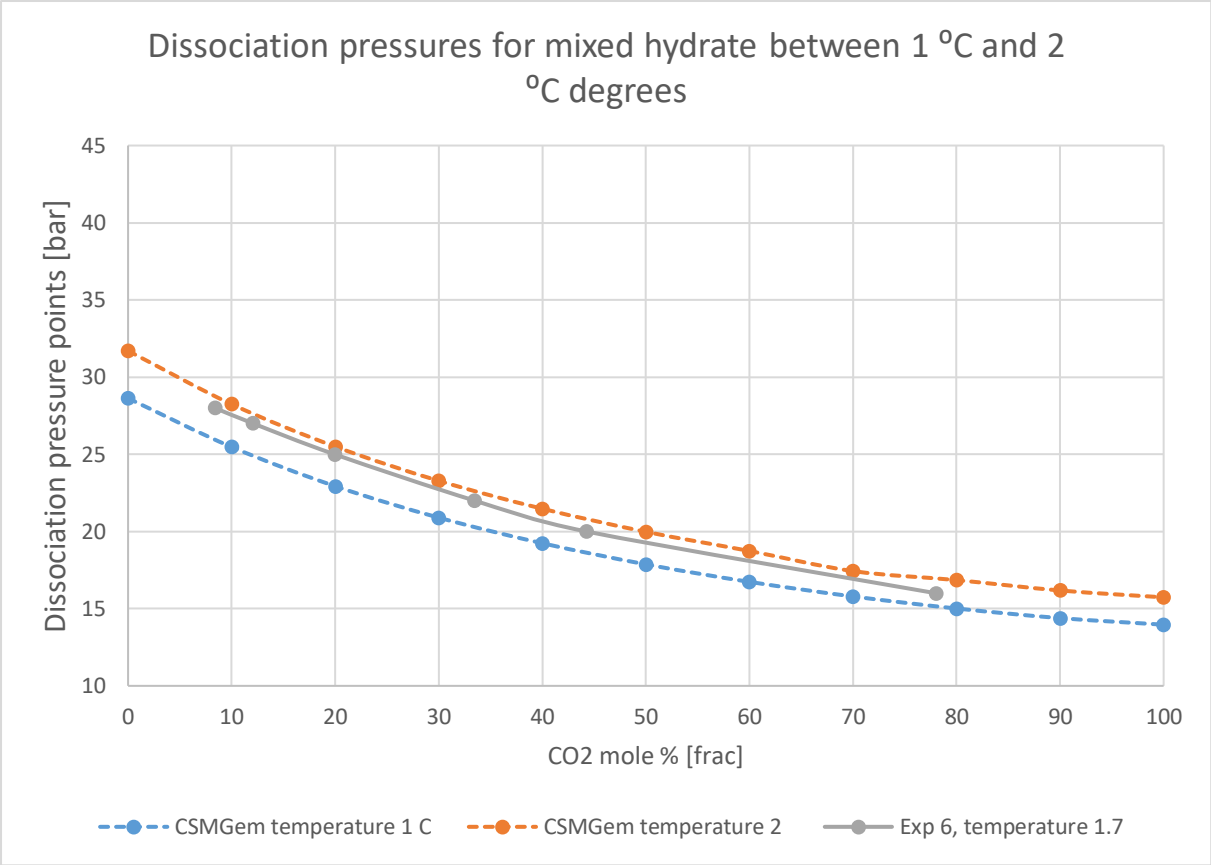

Figure 4-31 – Molar compositions for mixed hydrate experiment 6 plotted with theoretical equilibrium values in CSMGem at 1 °C and 2 °C.

Molar compositions after CO_2 injection between 3 °C and 4 °C

The next two figures show the compositional change for a mixed hydrate after CO_2 injection. There was not observed invasion of either water or liquid CO_2 in experiment 14 ($P_{eq,CH_4} = 36.117\ bar, P_{eq,CO_2} = 18.42$ bar (yellow points in Figure 4-32)). Hydrate films encapsulating CH_4 crystallized before dissociation suggesting water and CO_2 diffused into the FOV through wetting films. The most astonishing observation was hydrate dissociation above pure CH_4 hydrate equilibrium in experiment 14 and 15. The liberated gas in experiment 15 reformed rapidly into a stable hydrate structure, unlike in experiment 14. The liquid/gas boundary to CO_2 at 3.5 °C was calculated to 38.19 bar, assuming CO_2 phase conversion might have provoked dissociation above pure CH_4 hydrate equilibrium. Water invaded the pores in experiment 15 and 19 and increased the surface contact area for dissolved liquid CO_2 in water to contact methane hydrate. The increased surface contact area and observed dissociation points indicate a higher hydrate phase conversion compared to experiment 14.

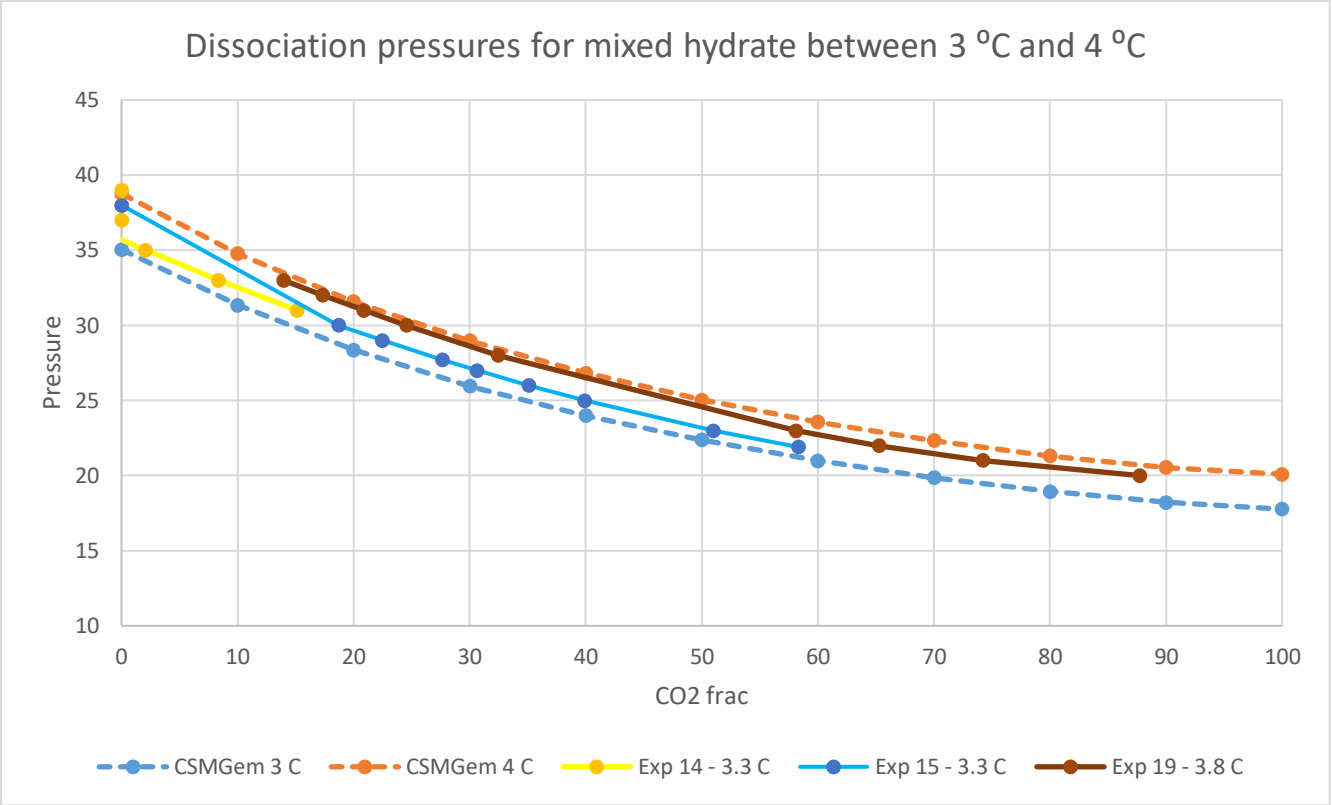

Figure 4-32 – Molar compositions after CO_2 injection for experiments conducted between 3 °C and 4 °C

Molar compositions after CO_2 injection between 4 °C and 5 °C

Experiment 16 had the highest water saturation before CO_2 injection, and the system did not experience water invasion during CO_2 injection. Higher water saturation increased the surface contact area for dissolved CO_2 to contact CH_4 hydrate, and resulted in a high phase conversion shown by the green line in Figure 4-33.

Experiment 17 experienced water invasion and following hydrate film growth in water and the invasion of liquid CO_2. The first point of dissociation at 29 bar makes the mixed hydrate gas composition to be 37 % CO_2 and 63 % CH_4. This was the highest mole fraction of CO_2 observed at the first point of dissociation and illustrates the impact of heat release from hydrate film growth and the presence of liquid CO_2. The dissociation points (blue line) shows the physical appearance of liquid CO_2 gives a higher $CO_2 - CH_4$ replacement compared to when liquid CO_2 is dissolved in water. The system was in a continuous formation-dissociation process (reformation) for several hours going from 22 to 18 bar. By theory, hydrate should have dissociated at pure CO_2 hydrate equilibrium at 21 bar, but the system experienced a form of self-preservation effect and completely dissociated at 18 bar. Makogon (Makogon and Ghassemi, 2010) explained self-preservation above the freezing point to be caused by an increase in capillary pressure due to alterations of the pore size and structure as a result of hydrate formation.

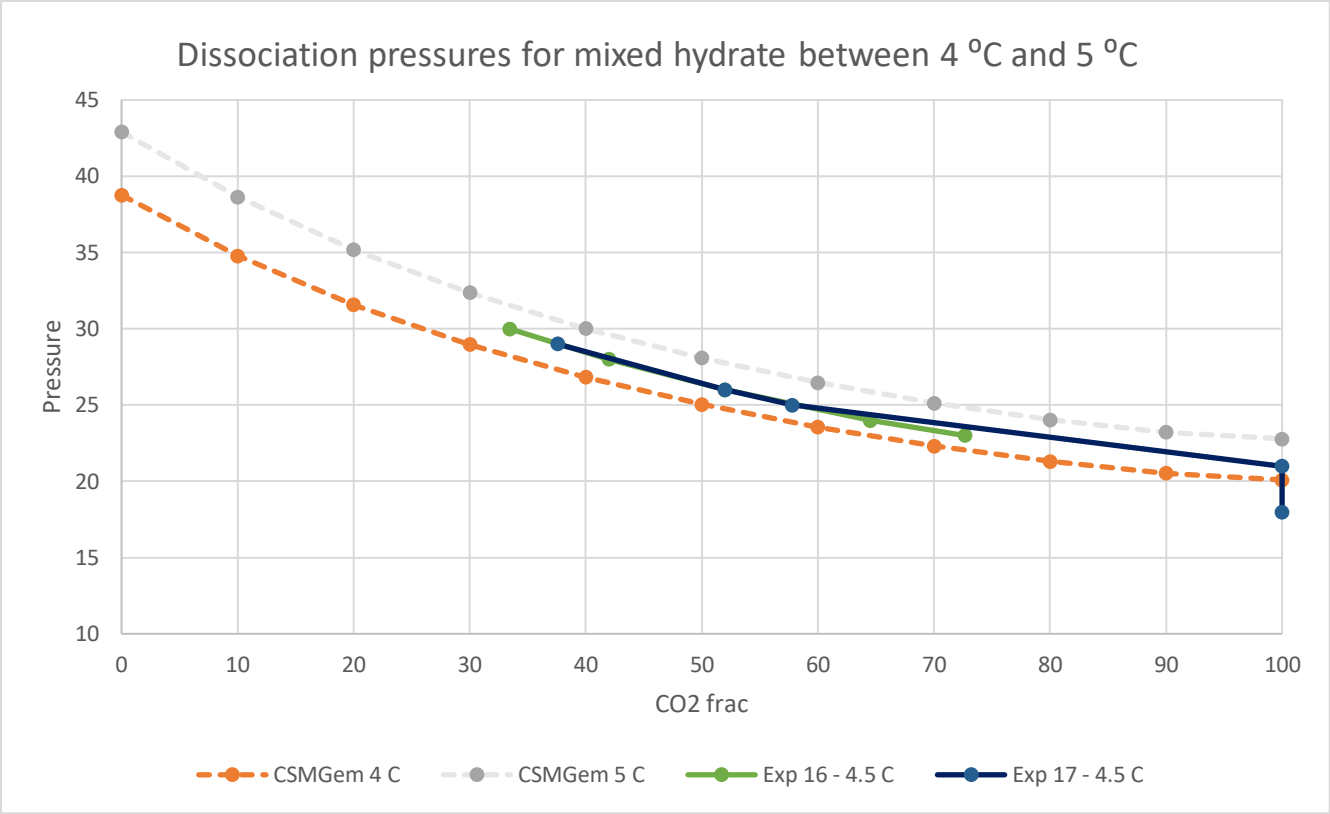

Figure 4-33 - Molar compositions after CO_2 for experiments injection conducted between 4 °C and 5 °C

To summarize; the experimental results from this study are in agreement to the compositional analysis reported by Belandria (Belandria *et al.*, 2011). The analysis shows a mixed hydrate dissociates at several pressures and gives a range of dissociation points independent of the saturation in the micromodel. A higher CH_4 gas saturation will, as anticipated, make multiple dissociation points closer to the equilibrium pressure to pure CH_4 hydrate. In contrast, high water saturation allows for more CO_2 to dissolve in water and a mixed hydrates will dissociate at pressures closer to the equilibrium pressure to pure CO_2 hydrate. Liquid CO_2 allows an amount of CH_4 to mix in the solution dependent on the formation pressure. A mix of liquid CO_2 and CH_4 gas forms mixed hydrates and gives multiple dissociation points in the mid-range between P_{eq,CH_4} and P_{eq,CO_2}.

5 Conclusions

Multicomponent hydrate systems were investigated on pore scale utilizing a silicon micromodel. This chapter presents key observations and is divided into three main groups: 1) Multicomponent hydrate formation, 2) liquid CO_2 injection into a micromodel with methane hydrate, and 3) mixed hydrate dissociation.

Mixed hydrate formation mechanisms

- Hydrate formation resulted in two hydrate configurations; hydrate films with encapsulated gas components and crystalline hydrate without enclosed gas components.
- In a system where CO_2 and CH_4 are present, hydrate growth initiated at the liquid CO_2 – water or CH_4 – water interface before growing towards the center of the pores.
- Systems with high gas saturation were rarely observed to grow into crystalline hydrate.
- Hydrate formation induced partitioning of dissolved components in water and increased hydrate saturation. The amount of dissolved CO_2 and CH_4 in water induced hydrate film or crystalline hydrate growth in the water phase.

Liquid CO_2 injection into a micromodel with methane hydrate

- Liquid CO_2 injection reduced hydrate (film) saturation significantly by displacing the gas encapsulated by hydrate films.
- Liquid CO_2 was transported to the field of view as liquid phase or by diffusion in water.
- Liquid CO_2 was enclosed by hydrate films quickly after injection.

Mixed hydrate dissociation

- A mixed hydrate released gas bubbles in portions leading to several dissociation points. Dissociation was observed from hydrate films and crystalline hydrate configurations. Further hydrate dissociation was favoured in contact with gas and not water.
- Systems with high water saturation dissociated at lower pressures indicating the presence of dissolved CO_2 in water. Whereas systems with high gas saturation dissociated at higher pressures closer to the equilibrium pressure to pure CH_4 hydrate.
- When liquid CO_2 was the only phase observed before formation, it was assumed to be a pure CO_2 hydrate. Results show that CH_4 can dissolve and mix with liquid CO_2 to form a mixed hydrate.
- Inside the gas hydrate P-T stability zone, two distinct liberated gas phases did not seem to mix.

- Hydrate reformation altered the hydrate gas composition to a higher mole fraction of CO_2 and lower mole fraction of CH_4.

6 Future work

Experimental work in micromodel can provide valuable information about single- and multicomponent gas hydrate system. The following suggestions for further projects are based on the author's interest:

- Multicomponent hydrate formation with saline water.
- Multicomponent hydrate formation using a microscope horizontally to investigate growth mechanism at the interface of the liquid- and gaseous component.
- Investigation of hydrate phase transitions in micro models with different wettability and mineral surfaces
- Liquid CO_2 injection into a micromodel saturated with crystalline methane hydrate
- Gaseous CO_2 injection into a micromodel saturated with methane enclosed by hydrate film
- Gaseous CO_2 injection into a micromodel saturated with crystalline methane hydrate

Nomenclature

$A_{pore\ area}$	Area of pore space	0.1 nm
A_{tot}	Total area of image	[J]
ΔG	Excess Gibbs free energy	[J]
$\Delta G^{surface}$	Surface excess free energy	$[J/mole]$
$\Delta G^{phase\ transition}$	Volume excess free energy	$[J/mole]$
Hf(1)	Hydrate film structure 1	-
Hf(2)	Hydrate film structure 2	-
Hf(3)	Hydrate film structure 3	-
$n_{methane\ gas}$	Refractive index of methane gas	-
n_{CO_2}	Refractive index of CO_2	-
$n_{hydrate}$	Refractive index of methane hydrate	-
$N_{bulk\ area}$	Number of pore area pixels	-
N_{tot}	Total number of pixels in image	-
N_{grains}	Number of grain pixels	-
P_{system}	System pressure	[bar]
P_{start}	Start pressure for injection	[bar]
P_{final}	Final pressure after injection	[bar]
P_{eq,CH_4}	Equilibrium pressure to pure CH_4 hydrate	[bar]
P_{eq,CO_2}	Equilibrium pressure to pure CO_2 hydrate	[bar]
r	Radius	m
S_w	Water saturation	-
S_g	CH_4 gas saturation	-
S_l	Liquid CO_2 saturation	-
T	Temperature	^oC
Å	Ångstrøm	0.1 nm
γ	Interfacial free energy	$[J/m^2]$
ρ_N^H	Molecular density	$[mole/m^3]$
$\emptyset_p$	Porosity	[fraction]

Abbreviations

CCUS	Carbon Capture Utilization and Storage
CSMGem	Colorado School of Mines Gibbs free energy minimization
D	Darcy
DRIE	Deep reactive ionic etching
EOR	Enhanced oil recovery
GHSZ	Gas hydrate stability zone
GHOZ	Gas hydrate occurrence zone
Mscf	Million standard cubic feet
NGH	Natural gas hydrates
PEEK	Polyetheretherketone
sI	Structure I hydrate
sII	Structure II hydrate
sH	Structure H hydrate

Bibliography

Almenningen, S., Flatlandsmo, J., Kovscek, A. R., *et al.* (2017) 'Determination of pore-scale hydrate phase equilibria in sediments using lab-on-a-chip technology', *Lab on a Chip*. Royal Society of Chemistry, 17(23), pp. 4070–4076. doi: 10.1039/c7lc00719a.

Almenningen, S., Flatlandsmo, J., Fernø, M. A., *et al.* (2017) 'Multiscale laboratory verification of depressurization for production of sedimentary methane hydrates', *SPE Journal*, 22(1), pp. 138–147. doi: 10.2118/180015-PA.

Almenningen, S., Iden, E., *et al.* (2018) 'Salinity Effects on Pore-Scale Methane Gas Hydrate Dissociation', *Journal of Geophysical Research: Solid Earth*, 123(7), pp. 5599–5608. doi: 10.1029/2017JB015345.

Almenningen, S., Gauteplass, J., *et al.* (2018) 'Visualization of hydrate formation during CO2 storage in water-saturated sandstone', *International Journal of Greenhouse Gas Control*. doi: 10.1016/j.ijggc.2018.11.008.

Anderson, G. K. (2003) 'Enthalpy of dissociation and hydration number of carbon dioxide hydrate from the Clapeyron equation', *Journal of Chemical Thermodynamics*. doi: 10.1016/S0021-9614(03)00093-4.

Aresta, M., Dibenedetto, A. and Quaranta, E. (2015) *Reaction mechanisms in carbon dioxide conversion*, *Reaction Mechanisms in Carbon Dioxide Conversion*. doi: 10.1007/978-3-662-46831-9.

Belandria, V. *et al.* (2011) 'Compositional analysis and hydrate dissociation conditions measurements for carbon dioxide + methane + water system', *Industrial and Engineering Chemistry Research*, 50(9), pp. 5783–5794. doi: 10.1021/ie101959t.

Benali, B. (2019) 'Quantitative Pore-Scale Analysis of CO 2 Foam for CCUS', Master thesis, University of Bergen.

Buchgraber, M. *et al.* (2012) 'Creation of a dual-porosity micromodel for pore-level visualization of multiphase flow', *Journal of Petroleum Science and Engineering*. doi: 10.1016/j.petrol.2012.03.012.

Bylov, M. and Rasmussen, P. (1997) 'Experimental determination of refractive index of gas hydrates', *Chemical Engineering Science*. doi: 10.1016/S0009-2509(97)00144-9.

Colorado School Of Mines (2015) *Center for Hydrate Research*. Available at: http://hydrates.mines.edu/CHR/Software.html (Accessed: 14 May 2020).

Englezos, P. (2019) 'Extraction of methane hydrate energy by carbon dioxide injection-key challenges

and a paradigm shift', *Chinese Journal of Chemical Engineering*. doi: 10.1016/j.cjche.2019.02.031.

Englezos, P., Dholabhai, P. D. and Kalogerakis, N. (1987) 'Kinetics of Formation of Methane Hydrates and Gas', 42(11), pp. 2647–2658. doi: doi.org/10.1016/0009-2509(87)87015-X.

Ersland, G. *et al.* (2010) 'Measuring gas hydrate formation and exchange with CO2 in Bentheim sandstone using MRI tomography', *Chemical Engineering Journal*, 158(1), pp. 25–31. doi: 10.1016/j.cej.2008.12.028.

Falenty, A. *et al.* (2016) 'Fluid composition and kinetics of the in situ replacement in CH 4 -CO 2 hydrate system', *Journal of Physical Chemistry C*, 120(48), pp. 27159–27172. doi: 10.1021/acs.jpcc.6b09460.

Flatlandsmo, J. (2015) 'Visualization and interpretation of methane hydrate growth and dissociation in synthetic porous media Master Thesis in Reservoir Physics', (December). Available at: http://bora.uib.no/bitstream/handle/1956/11667/142255490.pdf;sequence=1.

Graue, A. *et al.* (2006) 'Environmentally friendly CO2 storage in hydrate reservoirs benefits from associated spontaneous methane production', *Offshore Technology Conference 2006: New Depths. New Horizons*, 2, pp. 1050–1058.

Guo, J. *et al.* (2006) 'Solution properties of a fluorinated alkyl methacrylate polymer in carbon dioxide', *Macromolecules*, 39(9), pp. 3427–3434. doi: 10.1021/ma052409k.

Hancock, S. H. *et al.* (2005) 'Overview of thermal-stimulation production-test results for the JAPEX/JNOC/GSC et al. Mallik 5L-38 gas hydrate production research well', *Geological Survey of Canada Bulletin*, 585, pp. 1–15.

Hauge, L. P. *et al.* (2016) 'Pore-level hydrate formation mechanisms using realistic rock structures in high-pressure silicon micromodels', *International Journal of Greenhouse Gas Control*. doi: 10.1016/j.ijggc.2016.06.017.

Hermanrud, C. *et al.* (2009) 'Storage of CO 2 in saline aquifers-Lessons learned from 10 years of injection into the Utsira Formation in the Sleipner area', in *Energy Procedia*. doi: 10.1016/j.egypro.2009.01.260.

Hester, K. C. and Brewer, P. G. (2009) 'Clathrate Hydrates in Nature', *Annual Review of Marine Science*, 1(1), pp. 303–327. doi: 10.1146/annurev.marine.010908.163824.

Hornbrook, J. W., Castanier, L. M. and Pettit, P. A. (1991) 'Observation of foam/oil interactions in a new, high-resolution micromodel', *Proceedings - SPE Annual Technical Conference and Exhibition*,

Gamma, pp. 377–382. doi: 10.2523/22631-ms.

Husebø, J. (2008) '*Monitoring depressurization and CO2-CH4 exchange production scenarios in natural gas hydrates*. PhD thesis, University of Bergen.

Iden, E. (2017) Pore-Level Interpretation of Methane Hydrate Growth and Dissociation with Deionized and Saline Water', Master thesis, University of Bergen.

International Energy Agency (2019) *World Energy Outlook 2019*. Paris. Available at: https://www.iea.org/reports/world-energy-outlook-2019 (Accessed: 26 May 2020).

J. W. Jung, D. Nicolas Espinoza, J. C. S. (2010) 'Properties and phenomena relevant to CH4-CO2 replacement in hydrate-bearing sediments', Journal of Geophysical Research, vol. 115. doi:10.1029/2009JB000812.

Katsuki, D. *et al.* (2007) 'Methane hydrate crystal growth in a porous medium filled with methane-saturated liquid water', *Philosophical Magazine*, 87(7), pp. 1057–1069. doi: 10.1080/14786430601021652.

Katsuki, D. *et al.* (2008) 'Visual observation of dissociation of methane hydrate crystals in a glass micro model: Production and transfer of methane', *Journal of Applied Physics*, 104(8). doi: 10.1063/1.3000622.

Kvamme, B. *et al.* (2007) 'Storage of CO 2 in natural gas hydrate reservoirs and the effect of hydrate as an extra sealing in cold aquifers', *International Journal of Greenhouse Gas Control*, 1(2), pp. 236–246. doi: 10.1016/S1750-5836(06)00002-8.

Kvenvolden, K. A. (1988) 'Methane hydrate - A major reservoir of carbon in the shallow geosphere?', *Chemical Geology*, 71(1–3), pp. 41–51. doi: 10.1016/0009-2541(88)90104-0.

Lenormand, R., Touboul, E. and Zarcone, C. (1988) 'Numerical models and experiments on immiscible displacements in porous media', *Journal of Fluid Mechanics*, 189(November), pp. 165–187. doi: 10.1017/S0022112088000953.

Liang, S. *et al.* (2016) 'Molecular Mechanisms of Gas Diffusion in CO2 Hydrates', *Journal of Physical Chemistry C*, 120(30), pp. 16298–16304. doi: 10.1021/acs.jpcc.6b03111.

Lysyy, M. (2018) 'Pore-scale investigation of methane hydrate phase transitions and growth rates in synthetic porous media'. Master Thesis, University of Bergen.

Makogon, Y. F. (2010) 'Natural gas hydrates - A promising source of energy', *Journal of Natural Gas Science and Engineering*. doi: 10.1016/j.jngse.2009.12.004.

Makogon, Y. F. and Ghassemi, A. (2010) 'Effects of self-preservation of natural gas-hydrates', *44th US Rock Mechanics Symposium - 5th US/Canada Rock Mechanics Symposium*.

Morgan, J. (1953) '*Introduction to geometrical and physical optics*'. R. E. Krieger Pub. Co.

Moridis, G. J. *et al.* (2003) 'Strategies for gas production from hydrate accumulations under various geological and reservoir conditions', (January).

Moridis, G. J. *et al.* (2009) 'Toward production from gas hydrates: Current status, assessment of resources, and simulation-based evaluation of technology and potential', *SPE Reservoir Evaluation and Engineering*, 12(5), pp. 745–771. doi: 10.2118/114163-PA.

Nasir, Q., Sabil, K. M. and Lau, K. K. (2015) 'Measurement of isothermal (vapor+liquid) equilibria, (VLE) for binary (CH4+CO2) from T=(240.35 to 293.15) K and CO2 rich synthetic natural gas systems from T=(248.15 to 279.15) K', *Journal of Natural Gas Science and Engineering*. Elsevier B.V, 27, pp. 158–167. doi: 10.1016/j.jngse.2015.08.045.

Ohgaki, K. (1996) 'Methane exploitation by carbon dioxide from gas hydrates -phase equilibria for CO2-CH4 mixed hydrate system', Journal of Chemical Engineering Japan, 29(3), pp. 478-483.

Ohgaki, K., Takano, K. and Moritoki, M. (1994) 'Exploitation of CH4 Hydrates under the Nankai Trough in Combination with CO2 Storage', *Kagaku Kogaku Ronbunshu*, 20(1), pp. 121–123. doi: 10.1252/kakoronbunshu.20.121.

Ota, M., Abe, Y., *et al.* (2005) 'Methane recovery from methane hydrate using pressurized CO2', *Fluid Phase Equilibria*. doi: 10.1016/j.fluid.2004.10.002.

Ota, M., Morohashi, K., *et al.* (2005) 'Replacement of CH4 in the hydrate by use of liquid CO 2', *Energy Conversion and Management*. doi: 10.1016/j.enconman.2004.10.002.

Schoderbek, D. *et al.* (2012) 'North slope hydrate fieldtrial: CO2/CH4 exchange', *Society of Petroleum Engineers - Arctic Technology Conference 2012*, 1(December 2011), pp. 155–171. doi: 10.4043/23725-ms.

Schoderbek, D. *et al.* (2013) 'ConocoPhillips Gas Hydrate Production Test'. doi: 10.2172/1123878.

Seo, Y. T. and Lee, H. (2001) 'Multiple-phase hydrate equilibria of the ternary carbon dioxide, methane, and water mixtures', *Journal of Physical Chemistry B*, 105(41), pp. 10084–10090. doi: 10.1021/jp011095+.

Shindo, Y. *et al.* (1993) 'Kinetics of formation of CO2 hydrate', *Energy Conversion and Management*, 34(9–11), pp. 1073–1079. doi: 10.1016/0196-8904(93)90055-F.

Sloan, E. D. (1998) 'Gas hydrates: Review of physical/chemical properties', *Energy and Fuels*, 12(2), pp. 191–196. doi: 10.1021/ef970164+.

Sloan, E. D. (2003) 'Fundamental principles and applications of natural gas hydrates', *Nature*, 426(6964), pp. 353–359. doi: 10.1038/nature02135.

Span, R. and Wagner, W. (1996) 'A New Equation of State for Carbon Dioxide Covering the Fluid Region from the Triple-Point Temperature to 1100 K at Pressures up to 800 MPa', *Journal of Physical and Chemical Reference Data*, 25(6), pp. 1509–1596.

Stevens, J. C. *et al.* (2008) 'Experimental hydrate formation and gas production scenarios based on CO2 sequestration', *6th Gas Hydrates International Conference [ICGH] (Vancouver, British Columbia, 7/6-10/2008) Proceedings*, (May).

Tohidi, B. *et al.* (2001) 'Visual observation of gas-hydrate formation and dissociation in synthetic porous media by means of glass micromodels', *Geology*, 29(9), pp. 867–870. doi: 10.1130/0091-7613(2001)029<0867:VOOGHF>2.0.CO;2.

Uchida, T. *et al.* (2001) 'Replacing methane with CO2 in clathrate hydrate: Observations using Raman spectroscopy', in. Collingwood CSIRO Publishing, pp. 523–527.

Uchida, T., Ebinuma, T. and Narita, H. (2000) 'Observations of CO2-hydrate decomposition and reformation processes', *Journal of Crystal Growth*. doi: 10.1016/S0022-0248(00)00470-X.

Walsh, M. R. (2011) 'Microsecond Simulations of Spontaneous Methane Hydrate Nucleation and Growth', *Movie*, 1095(2009). doi: 10.1126/science.1174010.

Yuan, Q. *et al.* (2012) 'Recovery of methane from hydrate reservoir with gaseous carbon dioxide using a three-dimensional middle-size reactor', *Energy*. Elsevier Ltd, 40(1), pp. 47–58. doi: 10.1016/j.energy.2012.02.043.

Yuan, Q. *et al.* (2013) 'Methane recovery from natural gas hydrate in porous sediment using pressurized liquid CO2', *Energy Conversion and Management*. doi: 10.1016/j.enconman.2012.11.018.

Zhao, H. (2015) *CO2 calculator - A web computational tool*, *EMS Energy Institue at Penn State*. Available at: http://www.energy.psu.edu/tools/CO2-EOS/ (Accessed: 13 January 2020).

Zhao, J. *et al.* (2015) 'Experimental Study of Conditions for Methane Hydrate Productivity by the CO 2 Swap Method', *Energy and Fuels*, 29(11). doi: 10.1021/acs.energyfuels.5b00913.

Zhou, X. *et al.* (2008) 'Replacement of methane from quartz sand-bearing hydrate with carbon dioxide-in-water emulsion', *Energy and Fuels*, 22(3), pp. 1759–1764. doi: 10.1021/ef700705y.

Zhou, X. *et al.* (2016) 'In Situ Raman Analysis on the Dissociation Behavior of Mixed CH4-CO2 Hydrates', *Energy and Fuels*, 30(2), pp. 1279–1286. doi: 10.1021/acs.energyfuels.5b02119.